ISSN Print : 1656-4707
ISSN Online: 2467-5903

The Palawan Scientist

Volume 15 (2) December 2023

A Research Journal of the Western Philippines University
Aborlan, Palawan
www.wpu.edu.ph

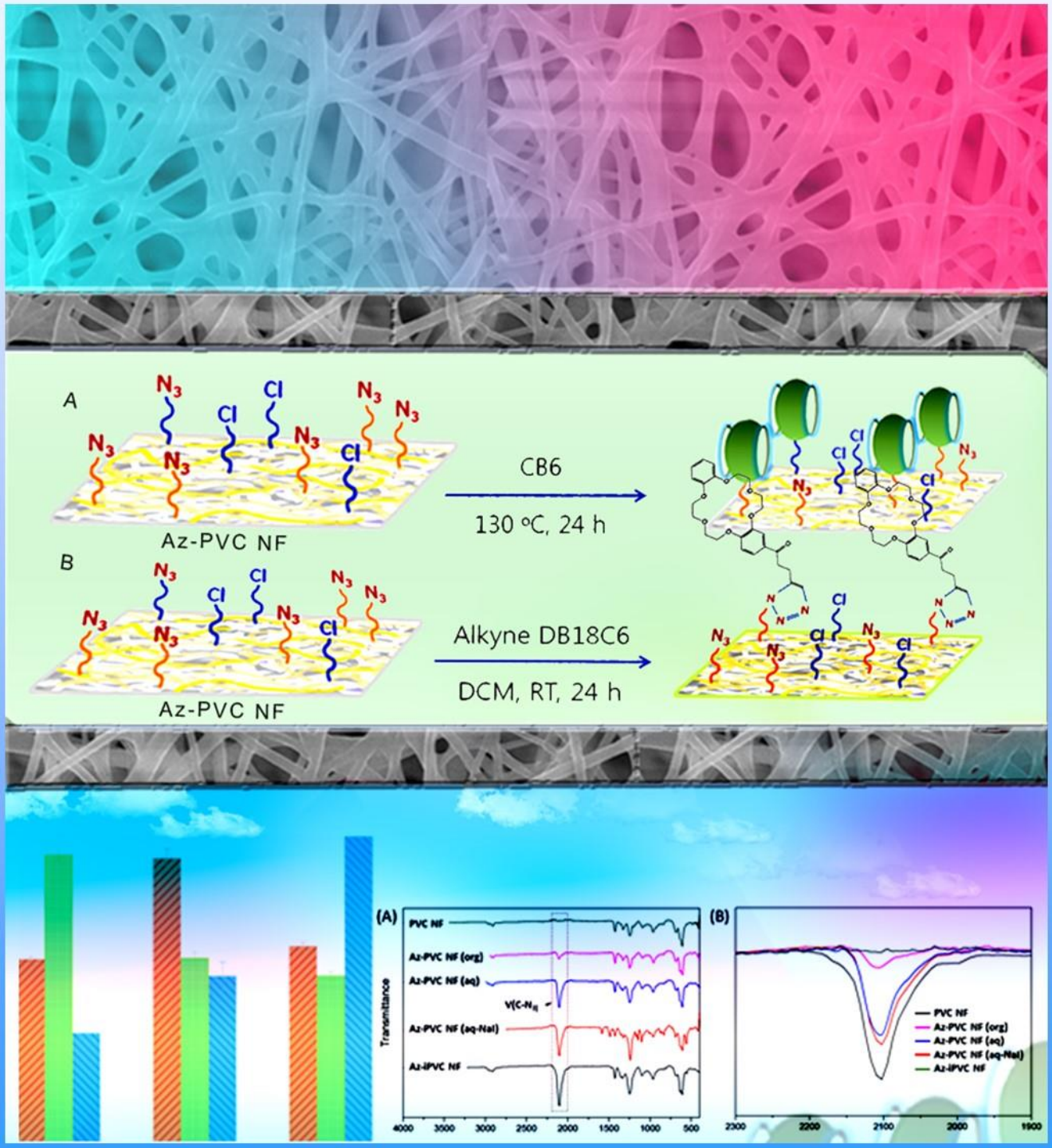

THE PALAWAN SCIENTIST is an externally peer-reviewed multi-disciplinary and open-access journal that **does NOT charge any processing/publication fees**. It releases one volume with two issues per year (June and December).

Moreover, published articles in this journal are indexed in the master journal list of Clarivate Analytics, ASEAN Citation Index, Andrew Gonzalez Philippine Citation Index, Philippine E-Journals, and both Google and Google Scholar. Articles are also stored on AquaDocs, and The Internet Archive.

OBJECTIVE AND SCOPE

As a multi-disciplinary journal, The Palawan Scientist aims to publish high-quality and original researches in agriculture, fisheries and aquatic sciences, environment, education, engineering, mathematics, sociology, and related disciplines.

DISCLAIMER

The Editorial Board of The Palawan Scientist does not provide warranties as to the completeness and veracity of the content. Moreover, the opinion and ideas expressed in this publication are by the authors and not necessarily of the publisher. The Western Philippines University cannot accept any legal responsibility or liability arising from plagiarism and other errors.

COPYRIGHT

COVER PHOTOS

Scanning electron microscopy (SEM) images and energy dispersive X-ray (EDX) spectra of pristine PVC NF (image A), Az-PVC NF (image B) and Az-iPVC NF (image C) membranes were obtained to visualize their surface morphology and estimate their surface elemental composition, respectively. SEM images show that electrospun PVC NF features thin, long fibers with nanosized diameters. Pristine PVC NF (Ø~ 413±195 nm) and Az-PVC NF (aq-NaI, Ø~ 426±201 nm) membranes are essentially morphologically similar which means that iodination and subsequent azidation of PVC NF membrane cause no change in the physical structure of the membrane. On the other hand, having been prepared using a different set of electrospinning conditions, Az-iPVC NF (Ø~ 187±53 nm) features thinner, densely meshed nanofibers. Results from surface elemental analyses via EDX further confirmed the presence of azide groups in Az-PVC NF and Az-iPVC NF, which contain approximately 6.8% and 9.8% nitrogen, respectively. **Images courtesy of EC Escobar.**

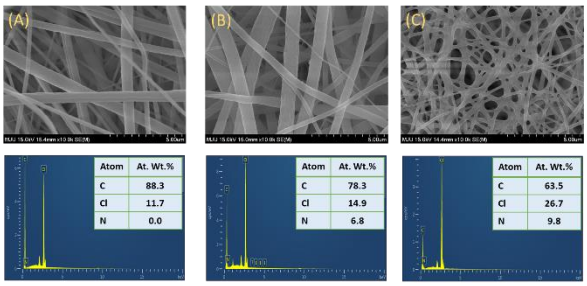

COVER DESIGN: Jovan A. Gimarangan

EDITORIAL

As a multidisciplinary journal, The Palawan Scientist has been evolving across different research areas in sciences for more than a decade. As proof of its wide dissemination and comprehensive efforts in publishing relevant and timely research outputs, published papers have expanded from agriculture and fisheries to engineering technical papers. The journal gears towards partnerships seeking to relentlessly uphold and publish outputs of many experts and young researchers alike.

In this year's partnership with the University of the Philippines Los Baños (UPLB), College of Engineering and Agro-industrial Technology (CEAT), the Palawan Scientist publishes its Special Issue containing selected research outputs presented during the 2nd International Conference of Engineering and Agro-industrial Technology (iCEAT). iCEAT is an annual event organized by CEAT UPLB which aims to provide avenue for exploration, discussion, recommendations and interconnectedness among leading experts, educators, policymakers, and industries on the latest trends, issues, and solutions for the field of engineering and agro-industrial technology.

This year, the iCEAT 2023 theme *"Materials and Processes for the New Normal: Sustainability, Innovation, and Opportunities"*. iCEAT envisions to work in collaboration with stakeholders for a universal call to act towards the attainment of the sustainable development goals (SDGs) towards no poverty, zero hunger, clean water and sanitation, affordable and clean energy, industry, innovation and infrastructure, sustainable cities and communities, responsible consumption and production, and climate action. Despite experiencing community disruptions during the onset of the COVID-19 pandemic, it has opened doors to technological and engineering advancements, all forward to societal future-proofing and sustainability. Innovations opened many opportunities for providing solutions to critical challenges.

The Palawan Scientist continues to encourage both experts and young researchers to experience being known through their research work published in this journal. This peer-reviewed journal serves as a platform for disseminating and sharing relevant research outputs in various fields that will contribute to developing further projects towards meeting the needs of communities especially the poor, needy and marginalized sector.

I would like to commend all authors, the iCEAT Organizing Committee members, and the Palawan Scientist Editorial Board members and staff for this year's successful collaboration. May this effective collaboration between UPLB and The Palawan Scientist continues to prosper in the years to come.

Hector R. Lim Jr., Ph.D.
Associate Editor-The Palawan Scientist
President, Agape Rural Program

CONTENTS

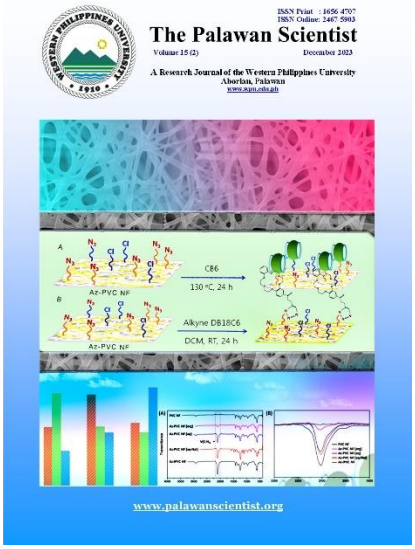

Current trends in modular wastewater treatment - a patent review

Jaren U. Tulipan and Jey-R S. Ventura*

Biomaterials and Environmental Engineering Laboratory, Department of Engineering Science, College of Engineering and Agro-Industrial Technology, University of the Philippines Los Baños, College, Laguna, Philippines

**Correspondence: jsventura@up.edu.ph*

Received: 30 May 2023 || Revised: 09 Sep. 2023 || Accepted: 27 Sep. 2023

ISSN: 1656-4707
E-ISSN: 2467-5903
Homepage: www.palawanscientist.org

How to cite:
Tulipan JU and Ventura JS. 2023. Current trends in modular wastewater treatment – a patent review. The Palawan Scientist, 15(2): 1-13.

ABSTRACT

Wastewater is a major source of water pollution, as it contains contaminants from human waste, chemicals, industrial runoff, and other sources that can be harmful to the environment and human health. Therefore, treatment is necessary to reduce its harmful effects. However, wastewater treatment (WWT) is often costly and difficult to implement in many areas. With conventional WWT designs lacking robustness and adaptability, modular designs can be a viable solution for this problem. In this review, a patent survey covering patents from 1996 to 2021 yielded 66 patents regarding modular WWT. The patent search showed increasing patents regarding modular WWT in recent years. Most of the patents were filed by companies in China. The International Patent Classification (IPC) was used to determine the current trends in modular WWT. Current patented designs suggest that there have been attempts to develop modularized electrochemical, separation, and sorption methods. Also, multistep patent designs showed fully integrated modular units from conventional WWT design and offer robustness and adaptability. This patent review showed that modular WWT technologies are capable and ready to be used in different settings.

Keywords: compact wastewater treatment, water pollution, wastewater treatment technologies

INTRODUCTION

Water pollution has become a global concern due to the exponential growth of the world's population and the rapid industrialization and urbanization (Sonune and Ghate 2004). This has led to a scarcity of clean water that makes it necessary to address this issue urgently. Wastewater generated by human activities further contributes to the problem, with an estimated 80% of wastewater worldwide discharged into the environment without adequate treatment (Dutta et al. 2021). This poses a significant challenge, especially for low-income countries where industrial wastewater contains high concentrations of metals, and domestic or municipal wastewater is laden with nutrients. In contrast, high-income countries can treat a larger proportion of their wastewater due to stricter regulations and the presence of wastewater treatment (WWT) facilities (Crini and Lichtfouse 2018; Dutta et al. 2021).

Wastewater treatment processes encompass a range of physical, biological, and chemical

techniques that have been extensively studied and applied over the years (Henze et al. 1997; Sonune and Ghate 2004; Anjaneyulu et al. 2005; Barakat 2011; Sharma et al. 2012). Current WWT processes typically involve four main stages: preliminary treatment, primary treatment, secondary treatment, and tertiary treatment. However, these conventional WWT plants suffer from notable drawbacks (Marchesseault et al. 2005; Reilly and Jelderks 2011a; Molinos-Senante et al. 2012; Jin et al. 2014). These challenges include the need for skilled operators, high operational costs, the requirement for overdesigning to accommodate future capacity increases and influent variations, the production of large amounts of waste sludge, and difficulties in adapting to varying influent volumes and contaminant concentrations.

Modular WWT systems offer a promising solution to these challenges by providing a robust, adaptable, and flexible approach to WWT, addressing many of the issues encountered in current designs (Spiller et al. 2015). These systems improve energy efficiency by optimizing the modules used for treating current influent wastewater, thereby reducing energy consumption. Additionally, their compact design minimizes land area requirements, making them suitable for small towns and industries with limited space. Modular treatment systems enable on-site WWT, extending the lifespan of existing facilities and ensuring effective treatment in specific areas. Moreover, modular designs allow for easy expansion by adding additional treatment modules to accommodate increased influent wastewater. Integrating modular WWT systems into current treatment plants can extend their operational life and ensure compliance with new effluent quality regulations.

However, it is crucial for modular systems to deliver comparable performance to conventional WWT plants. The primary objective of WWT is the removal of nutrients, with biodegradation being the preferred mechanism for breaking down these compounds (Dobson and Burgess 2007). The activated sludge process (ASP), a widely employed method, utilizes the aerobic degradation of organic compounds by supplying air to microbial communities in the reactor (Daverey et al. 2019). The ASP is considered a simple and cost-effective approach to WWT. However, current ASP systems are energy-intensive, resulting in high operational costs (Dobson and Burgess 2007; Daverey et al. 2019). To overcome this challenge, alternative secondary treatment technologies, such as membrane bioreactors, moving bed bioreactors, and sequencing batch reactors, have been explored.

This review aims to collect and evaluate patents filed between 1996 and 2021, focusing on the current design trends and technologies used in the development of modular WWT systems. By analyzing these patents, this review serves as a foundation for future advancements in modular WWT systems that will foster sustainability and address the pressing challenges associated with WWT.

PATENT SEARCH METHODOLOGY

Figure 1 shows the patent search methodology used for this study. A keyword search approach was used for the initial patent search using the Espacenet database of the European Patent Office. Generic keywords were used for the initial search which include “modular”, “compact”, “wastewater”, “treatment”, “plant”, “design”, “configuration”, “process”, and “method”. Only those patents relevant to modular WWT were considered, regardless of their International Patent Classification (IPC) classes. The selected patents were downloaded as a search query from the Espacenet database and compiled in an Excel spreadsheet. Two search queries were downloaded from the Espacenet database. The first search query was downloaded from the database on 02 August 2022 and contained 212 patents. The second search query, downloaded from the database on 08 August 2022 contained 54 patents. The patents were then reexamined to exclude searches that did not deal with treating wastewater and lacked modularity. From the previous search queries, only 66 patents were considered. The remaining relevant patents were then reanalyzed via the Google Patents database to find other data about the patent, i.e., patent application date, status, and countries where the patents were approved. The additional information extracted from each patent was done on 04 January 2023.

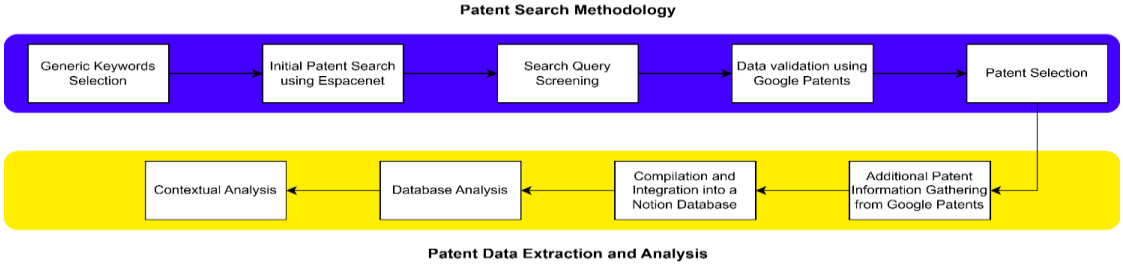

Figure 1. Patent search and data analysis methodology.

PATENT DATA EXTRACTION AND ANALYSIS

A total of 66 patents were found from the Espacenet and Google Patents databases that describe a design or a method of implementing a modular WWT technology. These patents were integrated into a Notion database (https://tinyurl.com/patentswwt). The exported information from each patent includes the patent number, patent name, application date, author/inventor, claims, figures, country of application, patent status, and IPC classes. The considered patents for the database are the applied patents only. However, during data gathering, the subcategories of the filed patents were recorded. The Notion database was used to analyze the patents and filter the patents according to different types of information exported. The filtered patents are used to determine the patent distribution with regard to the date of filing, country, and IPC classes. The claims of each patent were analyzed to give context to its design, validate its IPC classes, and further generalize the current design trends and application of WWT technology.

PATENT SITUATION FOR THE MODULAR WWT PLANT

As shown in Figure 2, the majority of the patents are from China, with 44 patents, followed by the USA with 14, Russia with three, and Australia, Canada, India, Germany, and South Korea with one patent each. Figure 3 shows the distribution of patents based on the year of application and the year of publication. It shows that the number of patent applications increased significantly from 2017 to 2021, with a peak of 10 patent applications in 2020 and 2021. During this period, 66% of the relevant patents for modular WWT were filed. Most of the patents from 1996 to 2016 were filed in the USA. Meanwhile, 38 out of the 45 patents filed from 2017 to 2021 were filed in China.

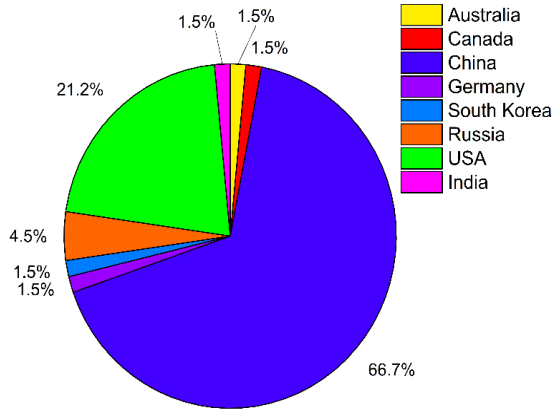

Figure 2. Distribution of patents based on the countries where they were filed.

It was seen that patents filed from 1996 to 2016 experienced slower publication, with an average of 902 days between the date of application and the date of publication. However, this has not been the case recently. Patents from 2017 to 2021 are generally granted faster, with an average of 340 days between the date of application and the date of publication.

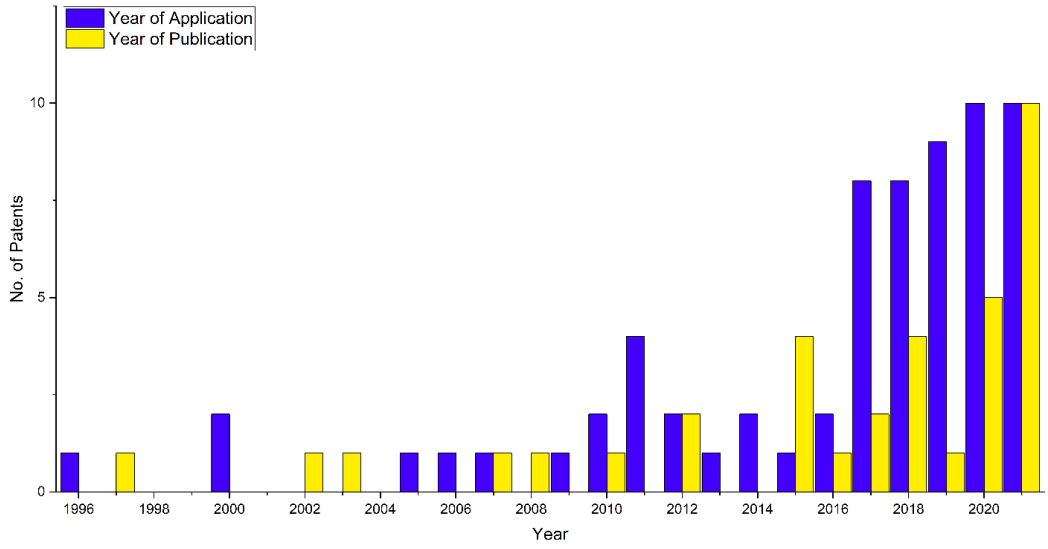

Figure 3. Distribution of patents based on the year of application and year of publication.

Figure 4 shows the distribution of patents based on the number of claims. Thirty-five out of the 66 patents considered in this study have between 6 and 10 claims. This shows that there has been a huge advancement in modular WWT technology. The presence of two patents with more than 41 claims suggests the uniqueness and complexity of their modular system. Furthermore, it is important to consider the implications of claim distribution in the context of intellectual property management and litigation. Patents with a large number of claims are more robust in defending against infringement as they cover a wider scope of potential violations. Conversely, patents with fewer claims could also be more concise and easier to manage.

Figure 5 shows the distribution of patents based on their application status. Currently, there are 34 active patents with modular WWT designs, of which 23 are from China. There is one withdrawn patent (CN108178461A) and two abandoned patents (US2005274669A1 and US20070289922A1). There are 10 expired patents, of which seven are classified as expired due to fee-related issues. As of this writing, there are 19 pending patent applications. Seventeen of them are from China, and two are from the USA.

Figure 6 shows the distribution of patents based on the nature of their current assignee. Most of the relevant patents have companies as their current assignees. Meanwhile, eight patents have universities as their current assignees, and eight patents have no assignee. The presence of multiple companies as patent holders can indicate several key points related to commercialization, technological advancements, and competitiveness within specific industries. Firstly, when numerous companies hold patents, it typically signifies a strong inclination toward commercializing inventions (Mazzoleni and Nelson 1998). Companies, driven by profit motives and the need to stay competitive in the market, tend to direct their innovations towards practical applications that can generate revenue. Also, companies often possess more substantial resources compared to universities, including robust research budgets, specialized facilities, and a skilled workforce (Lockett and Wright 2005). Consequently, a higher prevalence of company-held patents can indicate a faster pace of technological advancement in particular industries (Garavito and Rueda 2021). A greater number of companies holding patents can also foster a competitive ecosystem (Encaoua et al. 2006; Arora et al. 2008). Companies may engage in competition to innovate, which, in turn, promotes continuous enhancements in their products and services. This competitive environment can be advantageous for consumers by offering them a wider array of choices and potentially driving down prices**.**

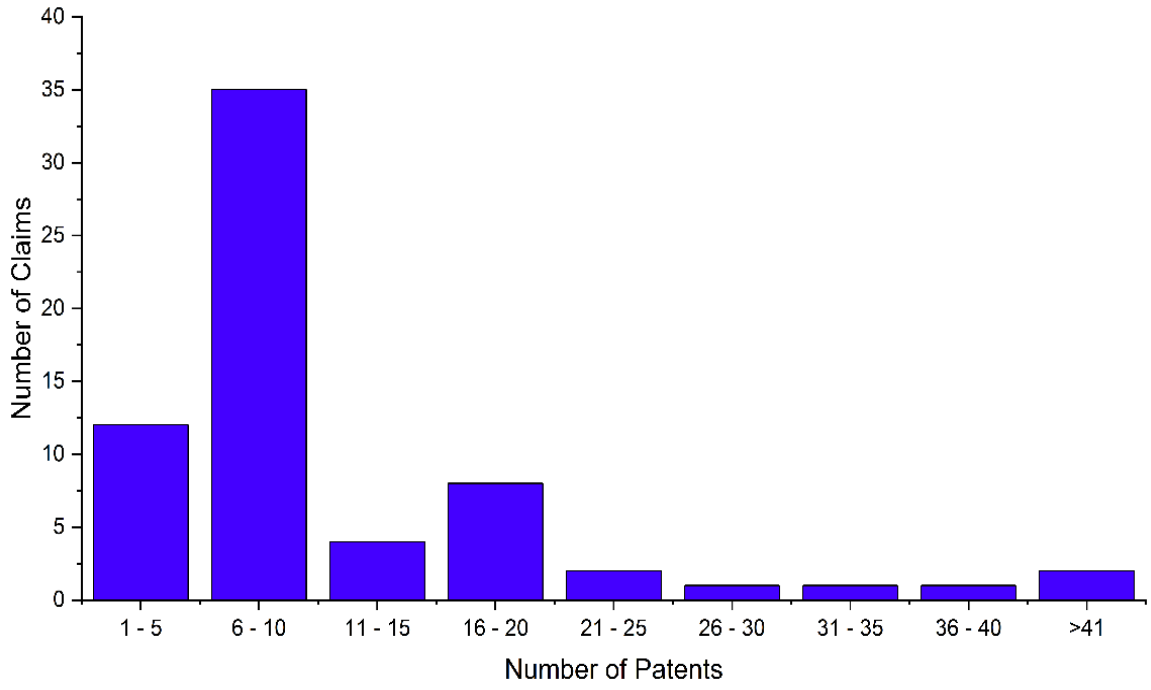

Figure 4. Distribution of patents based on the number of claims.

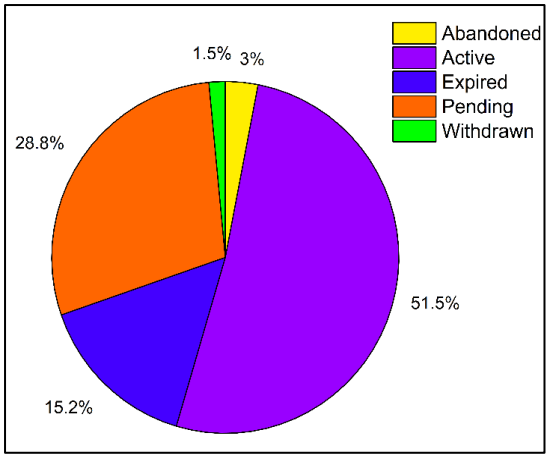

Figure 5. Distribution of patents based on application status.

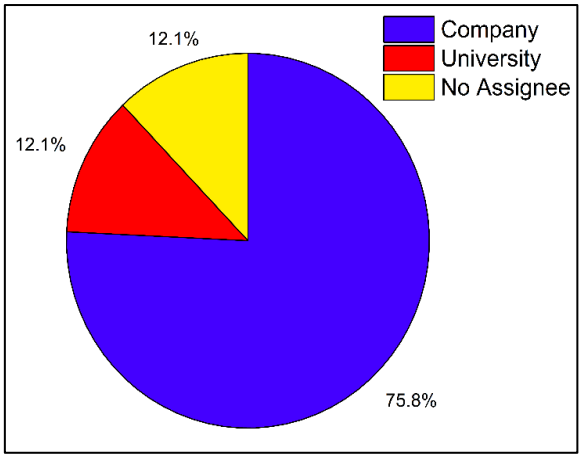

Figure 6. Distribution of patents based on current assignee.

CURRENT DESIGN TRENDS FOR MODULARITY OF WWT PLANT BASED ON THE IPC OF THE PATENTS

For this patent review, the classification considered for the patents is the IPC. This classification features a systematic and uniform means of classifying patents in terms of the area of technology of the patents. It uses a system of letters and numbers to form IPC symbols with class level, subclass level, group level, and subgroup level integrated into a single IPC symbol. Using this classification, it is easier to evaluate the current design trends for modular WWT based on filed patents.

Table 1 summarizes the IPC of the patents considered for this study. In the table, there are seven subclasses under which the 66 relevant patents were classified. This shows that there are numerous attempts at modularization of different technologies for WWT. The subclasses were focused on the separation process (B01D, B65D), treatment of water, wastewater, and sewage (C02F), containers and fixed constructions (E03B, E03F), and process control systems (G05B, G05D). Since the relevant patents pertain to modular WWT systems, groups under the C02F subclass were examined. Figure 7 shows the distribution of patents based on the IPC.

Besides the C02F subclass, the highest number of patents classified under a subclass is five. This subclass is B01D, which covers the separation of solids via physical processes such as filtration and sedimentation. Another subgroup involving separation methods is C02F9/02 where US2005274669A1 is classified. Also, the E03F5/14 subgroup covers the separation of solid or liquid substances from sewage.

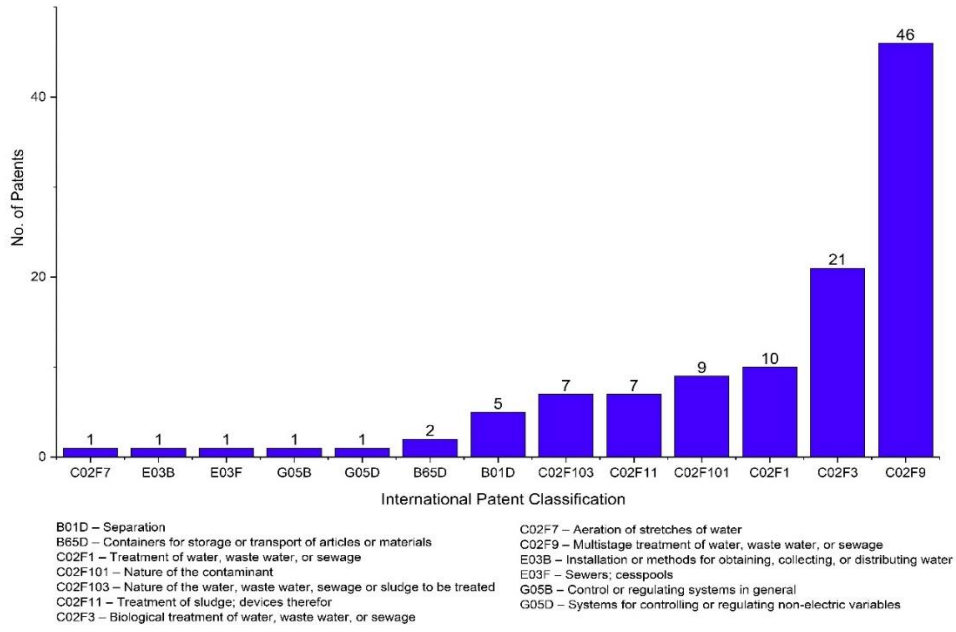

Figure 7. Distribution of patents based on IPC.

This implies that modular primary treatments are already designed and feasible for application. Further implications are the C02F9/08, C02F9/10, and C02F9/12 subgroups, where a total of five patents are classified under these classifications. These subgroups cover multistep WWT involving physical treatment. However, since physical treatment is a rather simpler treatment method than biological and chemical, the small number of patents classified under relevant classifications involving a physical treatment method shows that the modularity of physical treatments has not yet been fully explored.

The B65D and E03B subclasses imply a compact modular WWT design that is flexible to accommodate any wastewater-influent variations. B65D covers the storage and transport of materials. The IPC subgroups under this subclass under which two patents are classified are B65D21/024, B65D21/028, B65D88/010, B65D88/74, B65D90/02, and B65D90/10. The B65D21 group implies a flexible WWT design where modules are made of nestable, stackable, or joinable containers. Only WO2008006175A1 utilized such a design. The E03B subclass further aids the flexibility of WWT design because it considers the arrangement of treatment modules and methods of installation of the modules.

Another approach to having a flexible WWT system is the design disclosed in US2012055883A1. The patent disclosed a system of treatment modules that can go offline or online depending on the treatment needs of the influent wastewater. The patent is classified under the G05B subclass, which covers control systems regulating component variables. Meanwhile, US9079125B2 disclosed a design that has a flow level sensor that adjusts the influent volume dynamically so the treatment system can properly accommodate the influent wastewater. This patent is under the G05D subclass, which covers control systems for non-electrical variables.

From the relevant patents examined, there are already three approaches patented for a flexible and adaptable WWT system. The first is to have a design where modules are stackable and joinable. This signifies a modular system that can increase or decrease its treatment capacity by adding or removing treatment modules. The second approach is to have a control system that can dynamically control which treatment modules should be activated or deactivated to accommodate the varying wastewater influent on the system. The third approach, which is common to non-modular design, is to regulate the volume flow of influent wastewater to prevent overloading the system.

The C02F subclass deals with the treatment of water, wastewater, and sewage. Under this subclass, seven groups were identified by the IPCs of the relevant patents considered for this review. The C02F101 subclass covers the identity of contaminants in water, wastewater, and sewage. The patents showed that the patented modular WWT systems can treat different contaminants, such as heavy metals, inorganic compounds, nitrogen compounds, and organic compounds. This improves the applicability of a modular WWT system to any industry, small business, or municipality.

Common WWTs identified through the C02F1 group are sorption (C02F1/28), UV-light irradiation (C02F1/32), reverse osmosis (C02F1/44), electrochemical methods (C02F1/46), and oxidation with ozone (C02F1/78). Among the 66 patents considered in this review, only 10 are classified under the C02F1 group, as shown in Figure 5. This means that although different treatment methods are explored for modular systems, these designs are not mature and can be further developed. However, this shows that the modularity of WWT methods is feasible, and that further development of modular designs could lead to a higher number of patents being classified under this group. This also shows that different methods can be used as a treatment module for WWT. This means that a modular WWT design has a variety of options to treat a target characteristic of the influent wastewater.

The relevant patents also showed that their modular WWT system is capable of biological treatment. There are 21 patents classified under the C02F3 group and 27 patents under the C02F9/14 subgroup. The biological treatment used in modular designs can be categorized into four – aerobic processes, activated sludge processes, anaerobic digestion, and membrane bioreactors.

There are four patents using the biological treatment of wastewater through aerobic processes, which are classified under C02F3/02 and C02F3/06. The aerobic process disclosed by US9890067 utilized a column design of submerged filters to treat wastewater. Meanwhile, there are eight patents using aerobic and anaerobic processes in their multistep treatment design, as classified under C02F9/14. Designs include modular tanks, ponds, and treatment modules.

Meanwhile, there are 11 patents using the activated sludge process under the C02F3 group. Most of the designs use the conventional activated sludge process. Four patents under C02F9/14 used activated sludge in various integrations in multistep systems. There are also nine patents using anaerobic digestion for biological treatment. The patents generally use anaerobic digestion to have a complete nitrification and denitrification process.

Under the C02F3 group, CN108117150A and CN208055010U utilized membrane bioreactor modules. Furthermore, seven patents under C02F9/14 used membrane technology for their biological treatment in their multistep treatment systems.

The classification of the patents under C02F3 and C02F9/14 shows that even advanced biological treatments can have a modular design, which gives a glimpse of the high treatment efficiency of modular

WWT systems. This shows that biological treatment is now well integrated into modular systems.

Patented modular WWT systems also have sludge treatment modules. There are seven patents that are classified under the C02F11 group. The treatment methods for sludge disclosed by these patents include biological treatment, anaerobic treatment, dewatering and thickening, oxidation, and adding chemical agents. The small number of patents integrating sludge treatment modules into their treatment systems suggests that sludge treatment is not the primary concern of such modular systems. However, the seven patents showed that sludge treatment modules are feasible to integrate into modular systems, making a more complete system.

Among the groups under the C02F subclass, the C02F9 group has the highest number of identified patents. This group covers the multistep treatment of wastewater. The identified subgroups that the patents are classified under involve separation steps (C02F9/02), chemical treatment steps (C02F9/04), electrochemical treatment steps (C02F9/06), physical treatment steps (C02F9/08, C02F9/10, C02F9/12), and biological treatment steps (C02F9/14). As shown in Figure 8, the number of patents being classified under C02F9 is increasing from 2015 to 2021. The high number of patents and the annual increase in the number of patents classified under this group offer two insights. The first is that, due to more complex wastewater influents that need to be treated, a move toward designing a multistep modular treatment system is crucial to preventing untreated wastewater effluent. The second is that, due to the development of different treatment modules through the years, there are now enough designs and methods to integrate different treatment modules into a single modular treatment system. Designing a multistep modular WWT system also offers robustness in terms of treatment efficiency. Multistep treatment offers a higher possibility of removing any unexpected contaminants the influent wastewater may contain.

The current patented modular WWT systems showed the following insights on the treatment system design.

1. Primary treatment methods and secondary biological treatment methods are well integrated into modular systems. This integration ensures that the initial stages of WWT efficiently remove solid materials and pollutants.

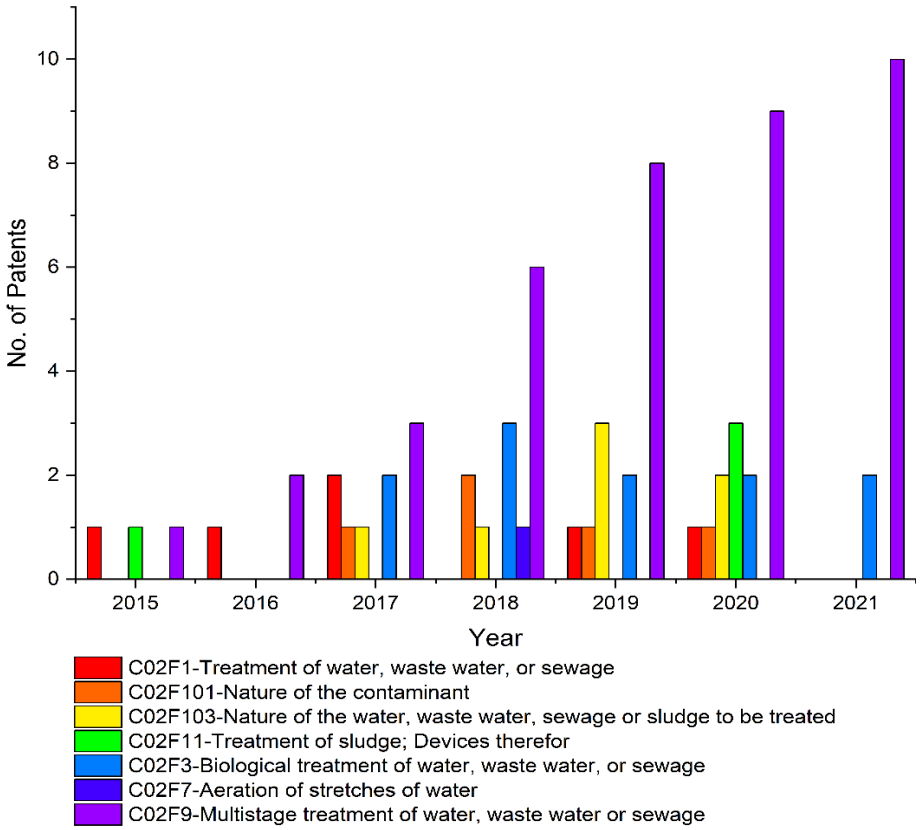

Figure 8. Distribution of patents from 2015-2021 based on the C02F subclass.

Table 1. Current design trends based on International Patent Classification (IPC).

IPC	IPC Title	IPC Description	Sample Patents (Source)	Modular Design Features of the Patents	Source
B01D	Separation of solids	Physical processes such as filtration, sedimentation, crystallization, precipitation, absorption, and adsorption	US9079125B2 (Reilly and Jelderks 2011b) ,	Treatment basins	(WIPO, 2023a)
			US9890067 (Monsrreal and Rogelio 2012)	removable screens	
			KR102069161B1 (Hyun and Choi 2019)	settling baffles	
			CN109381898A (Wang 2017)	filtration via loose material	
B65D	Containers for storage and transport	Covers nestable, stackable, or joinable containers	WO2008006175A1 (Wallis 2007)	Rearrangeable tanks with flexible applicability	(WIPO, 2023b)
			KR102069161B1 (Hyun and Choi 2019)	Tank design for wastewater treatment made of reinforced fiber glass	
C02F1	Treatment methods for water and wastewater	Covers various methods such as flotation, sorption, irradiation, dialysis, and reverse osmosis	US20160115062 (Krieger 2015)	Flotation system	(WIPO, 2023c)
			CN102050539A (Zhu et al. 2010)	Treatment using activated charcoal	
			US8318008B1 (Anderson 2009)	Ultraviolet sterilizer	
			US9890067 (Monsrreal and Rogelio 2012)	Nanofiltration reverse osmosis unit	
			CN111302478A (Zhang et al. 2020)	Electrolysis and electrochemical separation	
			CN106966467A (Yang and Li 2017)	Modular electrochemical WWT	
			CN105776442A (Yu et al. 2016)	Ozone disinfection	
C02F101	Nature of contaminants in water and wastewater	Covers organic and heavy metal compounds	CN108083579A (Yu et al. 2017), CN113880305A (Luo 2021), CN108911301A (Ren et al. 2018)	Removal of organic compounds	(WIPO, 2023c)
			CN113415959 (Liu et al. 2021), CN113880305A (Luo 2021),	Removal of heavy metals	

IPC	IPC Title	IPC Description	Sample Patents (Source)	Modular Design Features of the Patents	Source
			CN215365331U (Hui et al. 2021) CN111573999A (Tong et al. 2010), CN111646648A (Yan et al. 2020), CN110127963A (Xu et al. 2019)	Removal of inorganic, organic, and nitrogen compounds	
C02F103	Nature and origin of wastewater	Covers wastewater from different sources such as mining activities, oilfields, and food industries	CN113415959 (Liu et al. 2021) CN111792764A (Zhang et al. 2020) CN212504336U (Zhang et al. 2020) CN108083579A (Yu et al. 2017)	Treatment of sludge and wastewater Use of trough and subtroughs for connections Treatment of acid mine wastewater Treatment of wastewater from animal husbandry	(WIPO, 2023c)
C02F11	Devices for treating sludge	Covers various treatment methods such as biological, anaerobic, and addition of chemical agents	US6379545B1 (Perslow et al. 2000) US2015014245A1 (Rogelio and Monsrreal 2012) CN111646648A (Yan et al. 2020) RU2741566C1 (Sargin and Vinichenko 2020)	Integrated sludge digester Anaerobic treatment Screw filters for mechanical dewatering Use of chemical agents	(WIPO, 2023c)
C02F3	Biological treatment of water and wastewater	Covers various treatment methods such as aerobic and anaerobic processes using activated sludge	WO2008006175A1 (Wallis 2007) US5688400A (Baxter 1996) US9079125B2 (Reilly and Jelderks 2011b) CN208055010U (Tang and Xu 2018)	Biological filtration Aeration chamber Activated sludge process MBR technology	(WIPO, 2023c)
C02F7	Aeration of stretches of water	Covers aeration of water for WWT	CN108178461A (Hui 2018)	Modular high-efficient film device used to treat and aerate wastewater	(WIPO, 2023c)
C02F9	Multistep treatment of water,	Covers various methods such as chemical, electrochemical,	US20160115062 (Krieger 2015))	Mobile WWT facility with flotation, filtration, chemical, sludge	(WIPO, 2023c)

IPC	IPC Title	IPC Description	Sample Patents (Source)	Modular Design Features of the Patents	Source
	wastewater, and sewage	physical, thermal, and biological processes	US2021246058A1 (McFadden 2021)	treatment modules, and desalination system Two-step treatment of landfill condensate using an aerobic reactor and an anaerobic reactor	
			US2005274669A1 (Marchessault et al., 2005)	Modular transportable WWT system with bioreactor, anoxic tank, membrane filter, and UV disinfection unit	
E03B	Installations used for obtaining, collecting, or distributing water	Covers methods related to water collection	WO2008006175A1 (Wallis 2007)	Water treatment tank design, collection facility	(WIPO, 2023d)
E03F	Fixed constructions of sewers and cesspools	Covers devices for separating liquid or solid substances from sewage	RU2727420C1 (Ermachenko and Bukhantsov 2019)	Modular block unit for primary treatment of wastewater, equipped with device for collecting oils, fats and grease, semi-permissible baffle for retention of floating substances	(WIPO, 2023d)
G05B	Control systems or control elements used in regulating specific variables	Covers control systems for regulating specific variables	US2012055883A1 (Reilly and Jelderks 2011a)	Program control system for monitoring WWT system	(WIPO, 2023e)
G05D	Control systems for regulating non-electrical variables	Covers control systems for regulating non-electrical variables	US9079125B2 (Reilly and Jelderks 2011b)	WWT design equipped with a sensor for detecting wastewater input flow	(WIPO, 2023e)

2. There are already treatment modules that can be integrated into current WWT facilities to upgrade the treatment capabilities and accommodate a higher influent volume. This integration enables the upgrade of treatment capabilities, allowing these facilities to accommodate higher influent volumes without the need for extensive overhauls or expansions.

3. Current trends in modular wastewater systems emphasize multistep treatment processes. This approach results in robust systems capable of producing effluents with wastewater characteristics that meet or even exceed regulatory standards. It ensures a higher level of treatment effectiveness.

4. Patented systems focus on flexibility and adaptability. By adding or regulating treatment

modules, these systems can easily adapt to changing conditions, influent variations, and capacity demands. This adaptability minimizes the need for overdesign, reducing operational costs.

5. Integration of process control systems into current modular WWT design is crucial to achieving an easy-to-operate WWT system. This integration streamlines system operation, making it more user-friendly. Skilled operators become less of a necessity, thus, lowering operational costs.

The current trend observed in this patent review does reflect the existing WWT challenges and problems to some extent. Modular WWT systems, as seen from the IPC of the patents, offer a promising solution to these challenges. The systems offer energy and space efficiency, on-site treatment, scalability, and regulatory compliance. These systems are gaining attention in patents and industry discussions due to several advantages they bring, which align with the ongoing issues in WWT.

CONCLUSION

In recent years, there has been a rise in patent applications for modular WWT systems. This is attributed to the need for many communities and industries to comply with stricter effluent standards. Developed countries such as China and the USA are leading the patent applications for modular WWT systems. Most of the patents have companies as their current assignees. The current patent situation for modular WWT systems shows that there is rapid development in the system approach and design.

The relevant patents are analyzed based on their IPCs. The classifications showed that many different treatment methods have been modularized, such as electrochemical methods, separation methods, and sorption. The modular designs of these systems focus on removing contaminants such as nitrogen compounds, organic compounds, inorganic compounds, and heavy metals. Current designs have fully integrated biological treatments such as aerobic processes, activated sludge processes, and anaerobic digestion. Some of them incorporated sludge treatment via dewatering, chemical agents, biological treatment, and oxidation.

The current trend of modular design offers diverse ways to have an adaptable and flexible design. The current design trend also involves multistep treatment of wastewater, which offers robustness to the system. The integration of control systems as well as the further development of treatment modules will be factors in how the modular WWT system is going to be used in the future.

FUNDING

This research was funded by the Department of Science and Technology (DOST) - Philippine Council for Industry, Energy and Emerging Technology Research and Development (PCIEERD).

ETHICAL CONSIDERATIONS

The conduct of this review did not use/invove any animal or human as subject of the study.

DECLARATION OF COMPETING INTEREST

The authors declare that there are no competing interests for any authors.

ACKNOWLEDGMENTS

This study is part of the DOST PCIEERD funded project entitled “ENVITECS: NanoSiliCage (NSC): Nanocaged silicate composite for treatment of wastewater from Valenzuela City plastic industries” in collaboration with Material Science and Engineering Program – UP Diliman and Department of Engineering Science – UP Los Baños.

REFERENCES

Anjaneyulu Y, Sreedhara Chary N and Samuel Suman Raj D. 2005. Decolourization of Industrial Effluents – Available Methods and Emerging Technologies – A Review. Reviews in Environmental Science and Bio/Technology, 4(4): 245–273. https://doi.org/10.1007/S11157-005-1246-Z

Anderson SM. 2009. Modular individual wastewater nutrient removal system. (Patent No. US8318008B1). https://patentimages.storage.googleapis.com/72/fc/a4/10d6410b5febd2/US8318008.pdf. Accessed on 04 January 2023.

Arora A, Ceccagnoli M and Cohen WM. 2008. R&D and the patent premium. International Journal of Industrial Organization, 26(5): 1153–1179. https://doi.org/10.1016/j.ijindorg.2007.11.004

Barakat MA. 2011. New trends in removing heavy metals from industrial wastewater. Arabian Journal of Chemistry, 4(4): 361–377. https://doi.org/10.1016/J.ARABJC.2010.07.019

Baxter TD. 1996. Wastewater treatment plant. (Patent No. US5688400A). https://patentimages.storage.googleapis.com/98/fb/c7/9c7ca9f37083b0/US5688400.pdf. Accessed on 04 January 2023.

Crini G and Lichtfouse E. 2018. Advantages and disadvantages of techniques used for wastewater treatment. Environmental Chemistry Letters, 17(1): 145–155. https://doi.org/10.1007/S10311-018-0785-9

Daverey A, Pandey D, Verma P, Verma S, Shah V, Dutta K and Arunachalam K. 2019. Recent advances in energy efficient biological treatment of municipal wastewater. Bioresource Technology Reports volume 7. Elsevier, Amsterdam, Netherlands. https://doi.org/10.1016/J.BITEB.2019.100252"

https://doi.org/10.1016/J.BITEB.2019.100252. Accessed on 22 May 2023.
Dobson RS and Burgess JE. 2007. Biological treatment of precious metal refinery wastewater: A review. Minerals Engineering, 20(6): 519–532. https://doi.org/10.1016/J.MINENG.2006.10.011
Dutta D, Arya S and Kumar S. 2021. Industrial wastewater treatment: Current trends, bottlenecks, and best practices. Chemosphere, 285: 131245. https://doi.org/10.1016/J.CHEMOSPHERE.2021.131245
Encaoua D, Guellec D and Martínez C. 2006. Patent systems for encouraging innovation: Lessons from economic analysis. Research Policy, 35(9): 1423–1440. https://doi.org/10.1016/j.respol.2006.07.004
Ermachenko PA and Bukhantsov YV. 2019. Block-modular unit for primary treatment of wastewater. (Patent No. RU2727420C1). https://patentimages.storage.googleapis.com/fc/a4/c9/e729c10d12f6a3/RU2727420C1.pdf. Accessed on 04 January 2023.
Garavito HY and Rueda GJF. 2021. Innovation and patents as a business success factor. Journal of Economics, Finance and Administrative Science, 26(51): 143–159. https://doi.org/10.1108/JEFAS-09-2019-0218
Henze M, Harremoes P, Arvin E and la Cour Jansen J. 1997. Wastewater Treatment: Biological and Chemical Processes 2nd edition. Springer, Heidelberg, Germany. 383pp.
Hui T. 2018. Module type efficient membrane treatment device for wastewater treatment. (Patent No. CN108178461A). https://patentimages.storage.googleapis.com/d8/8c/9e/458578ededbd81/CN108178461A.pdf. Accessed on 04 January 2023.
Hui W, Zhang J, Ma J, Xu Q and Ren L. 2021. Modular efficient treatment device for heavy metal wastewater. (Patent No. CN215365331U). https://patentimages.storage.googleapis.com/0c/07/49/893c5956245d9d/CN215365331U.pdf. Accessed on 04 January 2023.
Hyun GK and Choi WS. 2019. Modular water treatment tank and method of preparing the same, and wastewater treatment facility including the same. (Patent No. KR102069161B1). https://patentimages.storage.googleapis.com/a2/f7/49/ca0352d0168657/KR102069161B1.pdf. Accessed on 04 January 2023.
Jin L, Zhang G and Tian H. 2014. Current state of sewage treatment in China. Water Research, 66: 85–98. https://doi.org/10.1016/J.WATRES.2014.08.014
Krieger JP. 2015. Mobile wastewater treatment system. (Patent No. US20160115062). https://patentimages.storage.googleapis.com/a3/9c/b4/b530ebf7531e2d/US20160115062A1.pdf. Accessed on 04 January 2023.
Ladron de Guevara C and Freeman L. 2006. Modular wastewater treatment system. (Patent No. US20070289922A1). https://patentimages.storage.googleapis.com/24/45/2c/3b56f6911f266e/US20070289922A1.pdf. Accessed on 04 January 2023.
Liu J, Fang Y, Yuan H and Wang C. 2021. Modular acid mine wastewater treatment equipment. (Patent No. CN113415959A). https://patentimages.storage.googleapis.com/c3/21/12/8cb1fbcb78be31/CN113415959A.pdf. Accessed on 04 January 2023.
Lockett A and Wright M. 2005. Resources, capabilities, risk capital and the creation of university spin-out companies. Research Policy, 34(7): 1043–1057. https://doi.org/10.1016/j.respol.2005.05.006
Luo F. 2021. Modular integrated flowback wastewater treatment system and method. (Patent No. CN113880305A). https://patentimages.storage.googleapis.com/92/2c/15/4c5fd8ff0d7ae9/CN113880305A.pdf. Accessed on 04 January 2023.
Marchesseault G, Beal TR, Edgar R, Ervey J, Keturakis A and Robblee C. 2005. Wastewater treatment system. (Patent No. US2005274669A1). https://patentimages.storage.googleapis.com/99/f3/08/bcbcf2fc2632ee/US20050274669A1.pdf. Accessed on 04 January 2023.
Mazzoleni R and Nelson RR. 1998. The benefits and costs of strong patent protection: A contribution to the current debate. Research Policy, 27(3): 273–284. https://doi.org/10.1016/S0048-7333(98)00048-1
McFadden AF. 2021. Anaerobic and aerobic treatment system and process for landfill wastewater. (Patent No. US2021246058A1). https://patentimages.storage.googleapis.com/2f/04/a7/230d6e8a185143/US20210246058A1.pdf. Accessed on 04 January 2023.
Molinos-Senante M, Garrido-Baserba M, Reif R, Hernández-Sancho F and Poch M. 2012. Assessment of wastewater treatment plant design for small communities: Environmental and economic aspects. Science of The Total Environment, 427–428: 11–18. https://doi.org/10.1016/J.SCITOTENV.2012.04.023
Monsrreal P and Rogelio J. 2012. Modular wastewater treatment plant. (Patent No. US9890067). https://patentimages.storage.googleapis.com/f7/2a/ad/78406a91c0bd54/US9890067.pdf. Accessed on 04 January 2023.
Perslow JA, Krebs ME and Matthews JA. 2000. Modular wastewater treatment system. (Patent No. US6379545B1). https://patentimages.storage.googleapis.com/5e/43/bb/82832aad53aec1/US6379545.pdf. Accessed on 04 January 2023.
Reilly JP and Jelderks VA. 2011a. Modular wastewater treatment system management. (Patent No. US2012055883A1). https://patentimages.storage.googleapis.com/68/9a/6b/b2b601ebbd1604/US20120055883A1.pdf. Accessed on 04 January 2023.
Reilly JP and Jelderks VA. 2011b. Modular wastewater treatment system management. (Patent No. US9079125B2). https://patentimages.storage.googleapis.com/9b/a1/e6/f53338eb6f27f3/US9079125.pdf. Accessed on 04 January 2023.
Ren X, Luo C, Yuan S, Wang J, Wu K, Luan X, Tang J, Zhang H and Tong Y. 2018. Modular organic wastewater treatment system. (Patent No. CN108911301A). https://patentimages.storage.googleapis.com/60/2d/45/cf612280944e3d/CN108911301A.pdf. Accessed on 04 January 2023.
Rogelio J and Monsrreal P. 2012. Modular wastewater treatment plant. (Patent No. US2015014245A1). https://patentimages.storage.googleapis.com/44/9f/a5/d1b2a85f855aeb/US20150014245A1.pdf. Accessed on 04 January 2023.
Sargin EY and Vinichenko AS. 2020. Biological treatment plant of domestic waste water in a block-modular design. (Patent No. RU2741566C1). https://patentimages.storage.googleapis.com/c5/76/5d/4889feedbcf6a2/RU2741566C1.pdf. Accessed on 04 January 2023.
Sharma SK, Sanghi R and Mudhoo A. 2012. Green practices to save our precious water resource. In: Sharma, SK and Sanghi, R. Advances in Water Treatment and Pollution Prevention. Springer, Heidelberg, Germany. pp. 1-36.
Sonune A and Ghate R. 2004. Developments in wastewater treatment methods. Desalination, 167(1–3): 55–63. https://doi.org/10.1016/J.DESAL.2004.06.113
Spiller M, Vreeburg JHG, Leusbrock I and Zeeman G. 2015. Flexible design in water and wastewater engineering - Definitions, literature and decision guide. Journal of Environmental Management, 149: 271–281. https://doi.org/10.1016/j.jenvman.2014.09.031

Tang B and Xu R. 2018. Novel modular integrated wastewater treatment device. (Patent No. CN208055010U). https://patentimages.storage.googleapis.com/26/f3/44/6818a4fe33c6a1/CN208055010U.pdf. Accessed on 04 January 2023.

Tang B and Xu R. 2018. Novel modular sewage treatment integrated device. (Patent No. CN108117150A). https://patentimages.storage.googleapis.com/ff/29/dd/d708536329038b/CN108117150A.pdf. Accessed on 04 January 2023.

Tong W, Ye W and Hong Y. 2020. Anaerobic ammonia oxidation treatment system in modular KtLM sewage treatment process. (Patent No. CN111573999A). https://patentimages.storage.googleapis.com/d0/85/49/786a3bf22d65dc/CN111573999A.pdf. Accessed on 04 January 2023.

Wallis SJ. 2007. Modular wastewater treatment tanks with releasable connections. (Patent No. WO2008006175A1). https://patentimages.storage.googleapis.com/50/f7/94/a2f7efc3894174/WO2008006175A1.pdf. Accessed on 04 January 2023.

Wang H. 2017. A kind of modular unit and its method of waste water treatment. (Patent No. CN109381898A). https://patentimages.storage.googleapis.com/b1/7a/14/fdb91e906eff60/CN109381898A.pdf. Accessed on 04 January 2023.

World Intellectual Property Organization (WIPO). 2023a. Section B — performing operations; transporting, B01 physical or chemical processes or apparatus in general. https://www.wipo.int/ipc/itos4ipc/ITSupport_and_download_area/20230101/pdf/scheme/full_ipc/en/b01.pdf. Accessed on 02 February 2023.

World Intellectual Property Organization (WIPO). 2023b. Section B — performing operations; transporting, B65 conveying; packing; storing; handling thin or filamentary material. https://www.wipo.int/ipc/itos4ipc/ITSupport_and_download_area/20230101/pdf/scheme/full_ipc/en/b65.pdf. Accessed on 02 February 2023.

World Intellectual Property Organization (WIPO). 2023c. Section C — chemistry; metallurgy, C02 treatment of water, waste water, sewage, or sludge. https://www.wipo.int/ipc/itos4ipc/ITSupport_and_download_area/20230101/pdf/scheme/full_ipc/en/c02.pdf. Accessed on 02 February 2023.

World Intellectual Property Organization (WIPO). 2023d. Section E — fixed constructions, E03 water supply; sewerage. https://www.wipo.int/ipc/itos4ipc/ITSupport_and_download_area/20230101/pdf/scheme/full_ipc/en/e03.pdf. Accessed on 02 February 2023.

World Intellectual Property Organization (WIPO). 2023e. Section G — physics, G05 controlling; regulating. https://www.wipo.int/ipc/itos4ipc/ITSupport_and_download_area/20230101/pdf/scheme/full_ipc/en/g05.pdf.Accessed on 02 February 2023.

Xu J, Zhou Z, Zhao J, Pan B, Song Y and Fu C. 2019. Modularized detachable comprehensive wastewater treatment device. (Patent No. CN110127963A). https://patentimages.storage.googleapis.com/34/51/18/82833387fe79c0/CN110127963A.pdf. Accessed on 04 January 2023.

Yan H, Liu D, Cao W, Chen Y, Xu D and Guo X. 2020. Modular railway train excrement collector excrement wastewater long-term treatment method. (Patent No. CN111646648A). https://patentimages.storage.googleapis.com/27/5a/cd/16ac37d01546be/CN111646648A.pdf. Accessed on 04 January 2023.

Yang B and Li J. 2017. Modular multi-element electrochemical wastewater treatment device and wastewater treatment method thereof. (Patent No. CN106966467A). https://patentimages.storage.googleapis.com/f3/70/80/c6ab0ab6c285cd/CN106966467A.pdf. Accessed on 04 January 2023.

Yu K, Hu L, Feng H, Chen S and Yang L. 2016. Modularized electrochemical wastewater treatment system. (Patent No. CN105776442A). https://patentimages.storage.googleapis.com/84/0d/d1/038ade1b7b4477/CN105776442A.pdf. Accessed on 04 January 2023.

Yu P, Li X and Sun J. 2017. Modular integrated system and technology for treating non-fermented bean product production wastewater. (Patent No. CN108083579A). https://patentimages.storage.googleapis.com/35/e1/ac/584b40902709c2/CN108083579A.pdf. Accessed on 04 January 2023.

Zhang C, Wu T and Sun Q. 2020. Modular closed ozone advanced oxidation aquaculture wastewater treatment system. (Patent No. CN212504336U). https://patentimages.storage.googleapis.com/41/54/e9/93329e335f16fa/CN212504336U.pdf. Accessed on 04 January 2023.

Zhang M, Jiang F and Li G. 2020. Coal mine underground full-membrane-method modular mine wastewater treatment method and device. (Patent No. CN111792764A). https://patentimages.storage.googleapis.com/c9/8e/61/3b118a4a183a9a/CN111792764A.pdf. Accessed on 04 January 2023.

Zhang X, Ouyang C, Cao X, Wei K, Huang X. 2020. Sludge and wastewater treatment device and sludge or wastewater treatment method. (Patent No. CN111302478A). https://patentimages.storage.googleapis.com/90/8b/76/b27590d2e72a90/CN111302478A.pdf. Accessed on 04 January 2023.

Zhu A, Zheng S, Jun C and Teng H. 2010. Movable industrial wastewater advanced treatment experimentation device. (Patent No. CN102050539A). https://patentimages.storage.googleapis.com/45/cd/be/79404c867430ec/CN102050539A.pdf. Accessed on 04 January 2023.

ROLE OF AUTHORS: *JUT - data collection, data gathering, data analysis, manuscript writing and editing; JSV – conceptualization, supervision, manuscript writing and editing.*

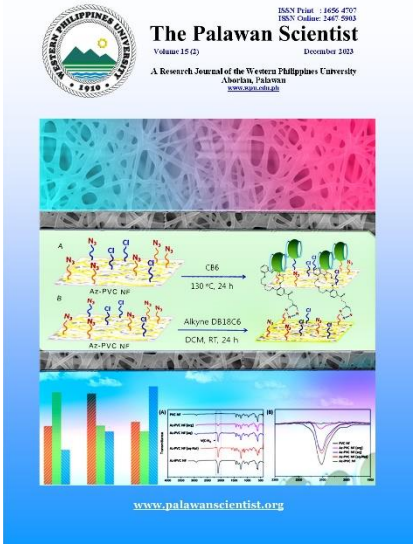

Facile preparation of azido functionalized polyvinyl chloride (PVC) nanofiber (NF) membrane for various applications

Erwin C. Escobar[1*], Grace M. Nisola[2] and Wook-Jin Chung[2]

[1]Department of Engineering Science, College of Engineering and Agro-Industrial Technology, University of the Philippines Los Baños, College Laguna, Philippines
[2]Environmental Waste Recycle Institute (EWRI), Department of Energy Science and Technology (DEST), Myongji University, Myongji-ro 116, Cheoin-gu, Yongin-si, Gyeonggi-do, South Korea 17058
**Correspondence: ecescobar1@up.edu.ph*

Received: 31 May 2023 || Revised: 22 Aug. 2023 || Accepted: 12 Sep. 2023

ISSN: 1656-4707
E-ISSN: 2467-5903
Homepage: www.palawanscientist.org

How to cite:
Escobar EC, Nisola GM and Chung WJ. 2023. Facile preparation of azido functionalized polyvinyl chloride (PVC) nanofiber (NF) membrane for various applications. The Palawan Scientist, 15(2): 14-20.

ABSTRACT

Polyvinyl chloride (PVC) nanofiber (NF) membrane functionalized with azido groups (Az-PVC NF) was prepared using various techniques with the aim of enhancing azide substitution of chlorine in the PVC backbone. Azidation strategies that were investigated include: (1) catalyst-assisted azidation in organic solvent, (2) phase transfer catalyzed azidation in aqueous media, (3) phase transfer catalyzed azidation in aqueous media using pre-iodinated membrane, and (4) phase transfer catalyzed azidation in aqueous media of electrospun pre-iodinated PVC granules prepared via Finkelstein reaction. Results showed that azidation was greatly enhanced when PVC NF membrane or PVC powder underwent pre-iodination prior to azidation. As far as it is known, this is the first time that preparation techniques for azidized PVC NF membrane in aqueous media that involve halogen exchange have been studied. Hence, the optimized conditions for the preparation of azidized PVC NF membranes and the resulting membrane properties are hereby reported. Furthermore, the utility of Az-PVC NF in the development of water treatment technologies was demonstrated with successful grafting of cucurbiturils via nitrene insertion.

Keywords: azide, covalent attachment, halogen exchange

INTRODUCTION

Polyvinyl chloride (PVC) is among the most widely produced and among the cheapest plastic materials (Pham et al. 2021). It has been used in a great variety of industrial, construction, and household products, and its applications continue to grow as new material processing technologies emerge. For example, with the development of electrospinning techniques for the production of nanofibers (NF) and nanofiber mats, PVC is now being used as membrane in air and water filtration systems, as protective layer in textiles, as anti-corrosion material, and many others (Ouerghui et al. 2016; Pham et al. 2021). These nanofiber-based applications of PVC take advantage of new or improved properties such as increased porosity and increased surface area resulting from the fabrication process.

Meanwhile, the use of PVC NF membrane in the development of air or water treatment technologies may be expanded by allowing attachment of molecules with desired functionalities. A convenient way to carry out this functionalization is to introduce azido groups on the PVC chain by substitution of chlorine. Thereafter, other molecules can be covalently tethered to PVC NF via nitrene or click chemistry. As such, azidized PVC NF (Az-PVC NF) membrane can be customized to possess features useful for functions other than filtration. In other words, azidation opens

PVC NF membrane to a multitude of modifications and applications.

Successful azidation of PVC NF membrane, however, is difficult to accomplish through conventional methods such as the use of organic solvents because these cause the fiber to deteriorate or they entail an exceedingly long time for substantial replacement of chlorine to take place. Process economics and occupational safety considerations require that azidation must be as pervasive and as swift as possible. Thus, strategies for the effective and efficient preparation of Az-PVC NF membrane need to be developed.

In this study, an assortment of techniques for the preparation of Az-PVC NF membrane were employed with the aim of achieving as much replacement of chlorine by azido groups as possible. It was found that remarkable improvements in azidation can be achieved using aqueous systems in the presence of a phase transfer catalyst, and that further improvements occur when prior replacement of chlorine by iodine is performed. This is the first report on the efficient and effective preparation of azidized PVC NF membrane in aqueous systems employing halogenation pretreatment. To demonstrate the utility of Az-PVC NF membrane in the development of water treatment technologies, it was grafted via nitrene insertion with cucurbit[6]uril or CB6—a pumpkin-shaped molecule capable of host-guest interactions with organic molecules and selective sequestration of large metal ions such as Cs^+ on two of its carbonyl rims.

METHODS

Materials

Polyvinyl chloride (PVC, average Mw~ 62000, average Mn~ 35 000) and cuburbit[6]uril hydrate were purchased from Sigma-Aldrich. Sodium azide (NaN_3, 99%, extra pure) and tetrabutylammonium bromide (TBAB, 99+%) were purchased from ACROS Organics, South Korea. Sodium iodide (NaI, 99+%) was manufactured by Showa Chemical Co. Ltd. (Japan). Solvents used include dimethylformamide (DMF, anhydrous, Fisher Scientific U.K. Ltd.), acetone (99.8%, DaeJung Chemicals and Metals, Korea), ethanol (99.9%, Samchun Chemicals, South Korea) and tetrahydrofuran (THF, 99.9%, Samchun Chemicals, South Korea). Deionized water (18.2 $m\Omega \cdot cm^{-1}$ at 25°C) was processed through a Millipore Milli-Q system. Reagents and solvents were used as received.

Preparation of PVC NF Membrane from pristine PVC Granules

An electrospinning solution was prepared by dissolving PVC granules (15 wt. %) in a 1:2 volume ratio of THF to DMF. Polyvinyl chloride nanofiber membrane was produced by electrospinning this solution at 22 kV at an ejection rate of 4 ml h^{-1} through a 21G needle and a rotating drum collector speed of 230 rpm at a distance of 100 mm.

Preparation of Iodinated PVC Granules

Iodinated PVC granules were prepared via Finkelstein reaction using sodium iodide as source of halogen nucleophile. Polyvinyl chloride granules (30 g) and NaI (71 g) were mixed in 215 ml acetone for 23 h. The iodinated granules were collected by filtration and dried overnight in an air-circulating oven at 65°C. Iodinated granules were vigorously washed multiple times with deionized water and then dried in a vacuum oven at 80°C for 12 h.

Preparation of PVC NF Membrane from Iodinated PVC Granules

Electrospinning solution was prepared by dissolving iodinated PVC granules (15 wt. %) in a 1:1.5 volume ratio of THF to DMF. Iodinated PVC NF membrane was produced by electrospinning this solution at 22 kV at an ejection rate of 2 ml h^{-1} through a 21G needle and a rotating drum collector speed of 230 rpm at a distance of 110 mm.

Preparation of Az-PVC NF Membranes

Four preparation techniques were employed to produce Az-PVC NF membrane. The first three involved use of PVC NF membrane prepared from pristine PVC granules (Figure 1) while the fourth involved PVC NF membrane prepared from iodinated PVC granules (Figure 2).

The first membrane underwent azidation by soaking for 24 h in saturated NaN_3 in DMF with 2% NH_4Cl as catalyst to produce Az-PVC NF (org) (Figure 1A). The second was soaked for 4 h in 6.15 mol L^{-1} NaN_3 and 0.037 mol L^{-1} TBAB in H_2O to produce Az-PVC NF (aq) (Figure 1B). The third was subjected to halogen exchange by soaking for 5 h in 6.15 mol L^{-1} NaI and 0.15 mol L^{-1} TBAB in H_2O, followed by soaking for 4 h in 6.15 mol L^{-1} NaN_3 and 0.037 mol L^{-1} TBAB in H_2O to produce Az-PVC NF (aq-NaI) (Figure 1C). The fourth membrane which was prepared from iodinated PVC granules was soaked for 4 h in 6.15 mol L^{-1} NaN_3 and 0.037 mol L^{-1} TBAB in H_2O to produce Az-iPVC NF (Figure 2). After azidation, the membranes were washed with copious amounts of deionized water followed by 70% ethanol, and then dried in a vacuum oven at 80°C for 12 h.

Preparation of CB6-loaded PVC NF Membrane

Azidized PVC NF membrane was soaked in an aqueous CB6 solution in HCl at 100°C. After reaction, the membrane was washed vigorously with deionized water followed by 70% ethanol, and then dried in a vacuum oven at 80°C for 12 h.

Instrumentation

Functional groups in membrane materials were identified using a Fourier transform infrared (FTIR) -attenuated total reflectance (ATR) (Varian Scimitar 2000, USA) spectrometer. Morphology and approximate surface elemental compositions were determined using a scanning electron microscope equipped with energy dispersive X-ray spectrometer (SEM-EDX, Hitachi S-3500 N, Japan) while fiber diameters (Ø) were measured from SEM images using ImageJ (Schneider et al. 2012). Mechanical properties were determined using a Universal Testing Machine (UTM LFPlus, Lloyd Instruments, UK) equipped with a 1 kN load cell. Azide loadings were quantified by elemental analysis using an Elemental Analyzer (Elementar Analysensysteme GmbH, Germany). Water droplets for contact angle (Θ) measurements were visualized with a video microscope (SCALAR VL-11S, Japan).

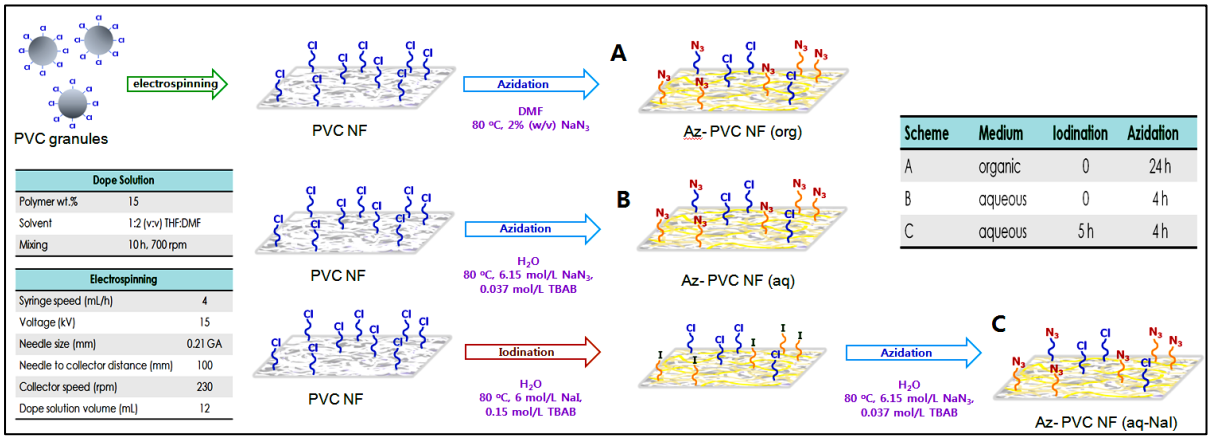

Figure 1. Preparation of membranes (A) Az-PVC NF (org), (B) Az-PVC NF (aq), and (C) Az-PVC NF (aq-NaI) using electrospun pristine PVC granules.

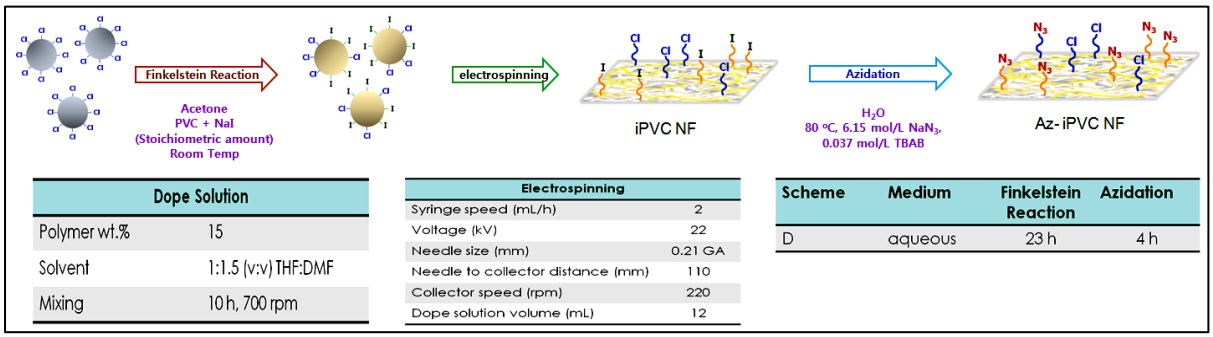

Figure 2. Preparation of Az-iPVC NF using electrospun iodinated PVC granules.

RESULTS

Characterization of azidized PVC NF Membranes

The FTIR spectra of pristine and azidized PVC NF membranes are provided in Figure 3A. The emergence of the azide peak at 2100 cm^{-1} suggests the presence of azido ($-N_3$) groups in the membrane which can be attributed to successful substitution of chlorine (Ouerghui et al. 2016). Results revealed a remarkable increase in the intensity of the azide peak in azidized PVC NF membranes prepared using aqueous azidation media. The superposition of the azide peaks (Figure 3B) provides a more vivid comparison of the peak intensities, with Az-iPVC NF exhibiting the strongest. The azide peak intensity follows the trend Az-iPVC NF > Az-PVC NF (aq-NaI) > Az-PVC NF (aq) > Az-PVC NF (org).

The actual azide load of each membrane was quantified via elemental analysis and results are summarized in Table 1. Results showed that the nitrogen content and consequently the azide load follow the trend Az-iPVC NF > Az-PVC NF (aq-NaI) > Az-PVC NF (aq) > Az-PVC NF (org) which is the same trend observed in the FTIR azide peak intensities. Az-iPVC NF membrane which registered the highest nitrogen content has an azide load of approximately 2.36 mmol g^{-1}.

Scanning electron microscopy images of pristine and azidized membranes show that electrospun PVC features thin, long fibers with nanosized diameters (Figure 4). Polyvinyl chloride nanofiber (PVC NF, Ø~ 413±195 nm) and Az-PVC NF (aq-NaI, Ø~ 426±201 nm) membranes are essentially morphologically similar which means that iodination and subsequent azidation of PVC NF membrane cause no change in the physical structure of the membrane (Figures 4A and 4B). On the other hand, having been prepared using a different set of electrospinning conditions, Az-iPVC NF (Ø~ 187±53 nm) features thinner, densely meshed nanofibers (Figure 4C). Results from surface elemental analyses via EDX further confirmed the presence of azide groups in Az-PVC NF and Az-iPVC NF, which contain approximately 6.8% and 9.8% nitrogen, respectively (Figures 4B and 4C).

.

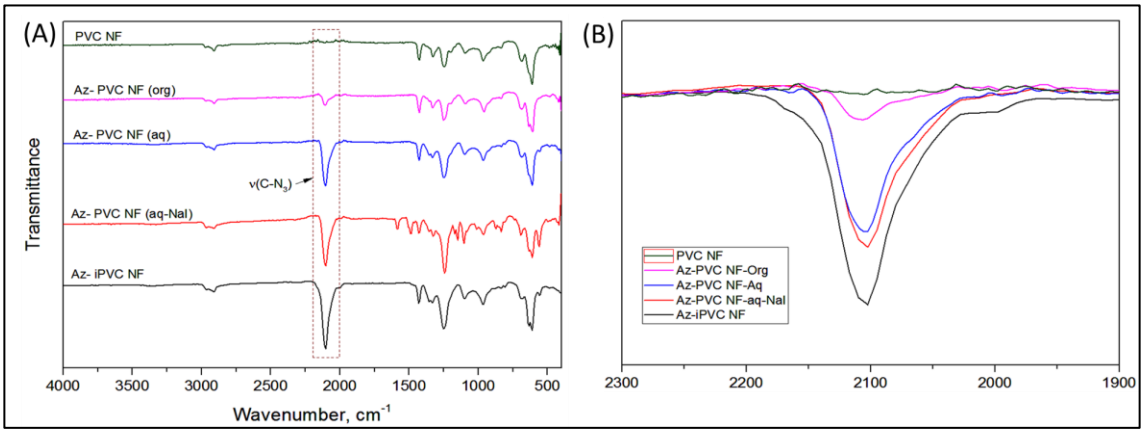

Figure 3. Fourier transform infrared spectra of (A) pristine PVC NF membrane and azidized PVC NF membranes prepared using different techniques, and (B) a superposition of their azide peaks.

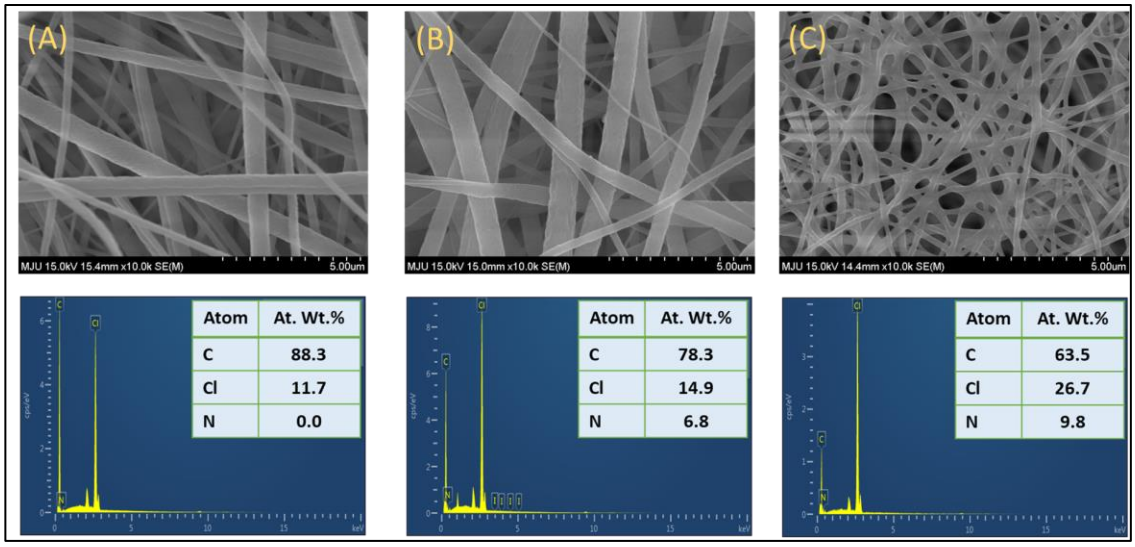

Figure 4. Scanning electron microscopy image and EDX spectra of (A) PVC NF, (B) Az-PVC NF (aq-NaI) and (C) Az-iPVC NF.

Table 1. Elemental composition and azide loading of PVC NF membranes.

Membrane	% C	% H	% N	Azide Load (mmol g^{-1})
PVC NF	38.64	4.992	0.35	0.08
Az-PVC NF (org)	38.64	4.974	2.80	0.67
Az-PVC NF (aq)	38.66	4.968	6.92	1.65
Az-PVC NF (aq-NaI)	39.23	4.905	8.51	2.03
Az-iPVC NF	39.00	4.868	9.91	2.36

The mechanical properties of the membranes were found to be at variance with one another. Young's moduli are around 20-35 MPa, stiffnesses are at 3900-6000 N m^{-1} and stresses at maximum load are at 1.34-2.68 N mm^{-2} (Figure 5). Despite the variability, the mechanical properties of all membranes prepared in this study are comparable with published data for which Young's moduli in the range 3.75-308 MPa and stresses at maximum load of 0.67-9.1 N mm^{-2} have been reported (Pham et al. 2021).

Covalent Immobilization of CB6 in Az-PVC NF

Thermally induced generation of nitrenes led to successful immobilization of CB6, as confirmed by the subsequent weakening of the azide peak (2100 cm^{-1}) and the emergence of the carbonyl stretch (1740 cm^{-1}) in the FTIR spectra of CB6-loaded PVC NF membrane (Figure 6A). The SEM image of CB6-loaded PVC NF (Ø~ 418±173 nm) membrane is shown in Figure 6B while the corresponding surface elemental scan which confirms the existence of oxygen, and hence surface-immobilized CB6, is shown in Figure 6C. Significant changes in surface properties were observed from static water droplet contact angle measurements whereby the previously hydrophobic surfaces of pristine (Θ = 137.5°) and azidized (Θ = 139.7°) PVC NF membrane became more hydrophilic after CB6 immobilization (Figure 6D), causing the water droplet to be flatter (Θ = 90.4°). This improved hydrophilicity is likely due to increased attractive electronic interactions (e.g. hydrogen bonding) between water molecules at the droplet interface and the carbonyl groups of immobilized CB6 on the PVC surface which effectively disrupts the droplet surface tension. As with most surfaces, the static water droplet contact angle approaches 90° or less as a consequence of hydrophilicity (Law 2014).

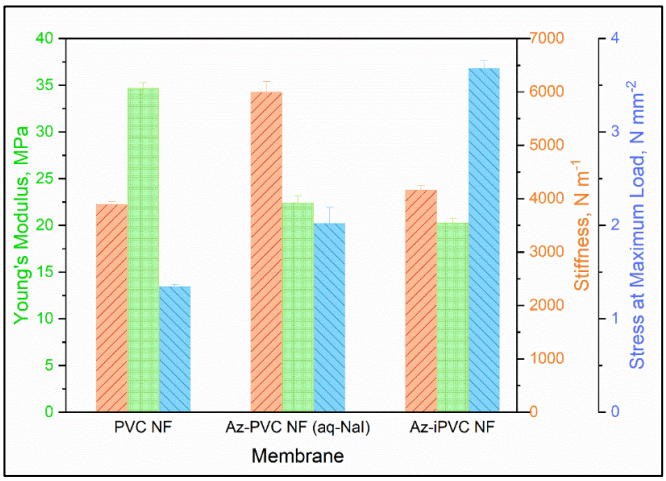

Figure 5. Mechanical properties of PVC NF, Az-PVC NF (aq-NaI) and Az-iPVC NF.

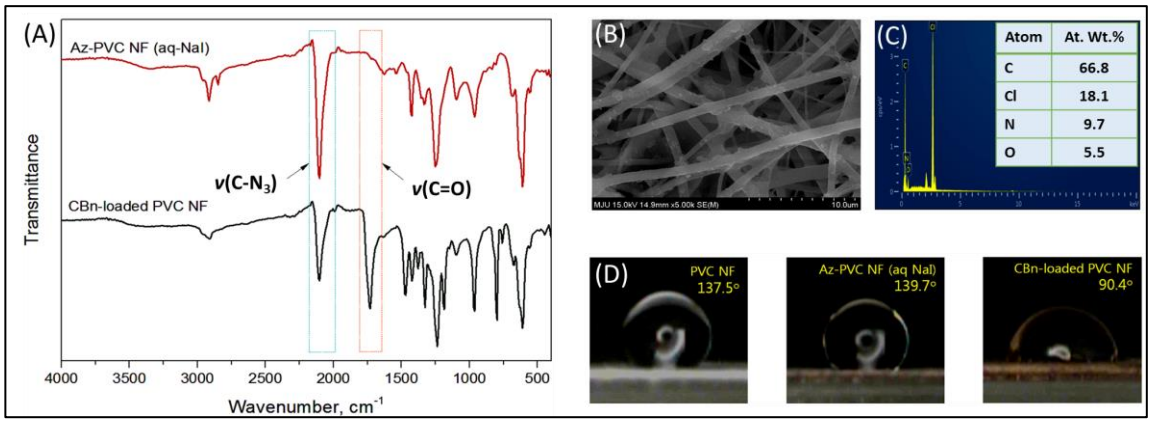

Figure 6. (A) Fourier transform infrared spectra of pristine and CB6-functionalized Az-PVC NF; (B) SEM image and (C) EDX spectrum of CB6-functionalized Az-PVC NF; and (D) water contact angles of PVC NF, Az-PVC NF and CB6-functionalized Az-PVC NF.

DISCUSSION

Azidation in Aqueous Systems and the Importance of Pre-iodination

Azidation of PVC is usually carried out in a polar aprotic solvent (e.g. DMF) since this favors S_N2 reactions by keeping the nucleophile prone to reactive collisions. This approach, however, cannot be applied to electrospun PVC NF membrane because the membrane deteriorates in DMF. Moreover, poor solubility of NaN_3 in DMF limits the amount of azide nucleophiles available. An azidation solvent system that keeps the PVC NF membrane intact and dissolves the azide salt easily had to be resorted to, and this was accomplished by performing the reaction in aqueous media in the presence of TBAB as phase transfer catalyst (Lakshmi and Jayakrishnan 2002). In this method, the soluble organic cation $N^+(Bu)^{4-}$ transports N_3^- from the aqueous phase to the organic solid phase of the PVC NF membrane where the nucleophilic substitution occurs. These explain the remarkable improvement in azide load of Az-PVC NF (aq) relative to Az-PVC NF (org).

Because a high loading of azide groups is desired, chlorine groups in the PVC NF membrane were pre-displaced with iodine, again by phase transfer catalysis using TBAB. Although a weaker base, iodine is a stronger nucleophile than chlorine if the reaction occurs in a polar protic solvent like water, which allows the replacement of chlorine to proceed spontaneously. Meanwhile, iodine is better than the azide ion at displacing chloride groups in the PVC backbone via nucleophilic substitution, which means that under the same conditions, more chlorine groups are replaced in PVC if it were reacted with iodine anions than when reacted with azide anions. In short, iodine ions are more effective than azide ions at sweeping off chlorine atoms from the PVC chain. Once attached to PVC, iodine atoms are not as firmly bonded as the chlorine groups that they displaced due to the larger atomic size of iodine. This causes iodine to have a greater tendency than chlorine to leave the alkyl backbone of PVC. As such, iodine atoms are more vulnerable to displacement by smaller nucleophiles like azide ions. This makes azidation of PVC more pervasive if preceded by iodination because iodination serves to facilitate the displacement of chlorine atoms and is easily substituted by azide ions thereafter. This explains the higher azide load of Az-PVC NF (Aq-NaI) than Az-PVC NF (Aq).

To further exploit the efficacious azidation of pre-iodinated PVC NF, a more vigorous iodination reaction through halogen exchange in acetone was performed. The procedure, however, cannot be applied to PVC NF membrane because the membrane dissolves completely in acetone. Fortunately, PVC granules are not so easily dissolved by acetone, and the halogen exchange reaction—also called Finkelstein reaction—may be performed successfully. Iodinated PVC NF membrane prepared from such granules registered the highest azide loading among all the different azidation strategies employed.

Applications of Az-PVC NF Membrane

Azido groups on PVC NF membrane can participate in nitrene insertion or click reactions resulting in covalently bonded molecules (Figure 7). Covalent immobilization of molecules on solid supports, especially the custom-made expensive functional molecules such as cucurbiturils and crown ethers, allows the possibility of multiple reuse which helps offset costs (Escobar et al. 2021; Escobar et al. 2022).

The conversion of azido groups to nitrenes that insert non-selectively into C-H bonds is particularly useful in covalently immobilizing molecules devoid of functional attachments or are difficult to chemically modify such as the cucurbit[*n*]urils or CB*n*'s where *n* represents the number of glycoluril units comprising the molecule. CB*n*'s are a family of macrocylic molecules that possesses highly symmetric structures with two identical negatively charged portal carbonyl groups and a hydrophobic cavity (Assaf and Nau 2015). Supramolecular assemblies built from CB6 with 4,4',4''-benzene-1,3,5-triyl tribenzoic acid as directing agent had been shown to exhibit high selectivity for Cs^+—an abundant component of radioactive wastes—against common alkali ions in basic medium (Chen et al. 2014), while CB8 in free form had been reported to have a high adsorption capacity for Pb^{2+} (Sun et al. 2016). Meanwhile, CB6 by itself has been found to form CB6-Cs^+ complexes, registering stability constants that are several orders of magnitude higher than those formed with either 18-crown-6 ether or cryptand 222, an outcome attributed mainly to the strong negative charge of the carbonyl rim and a close cavity-ion size match (Buschmann et al. 1992). Because of their ability to interact selectively with solutes, the covalent immobilization of CB*n*'s onto solid supports such as PVC NF is a huge step into their utilization for practical solute sequestration technologies. On the other hand, azido groups can participate in click reactions which permit fast and highly selective attachment of molecules that possess alkyne functionalities. Click reactions have been used extensively in the development of water decontamination technologies involving various specialized alkyne-bearing molecules on different azido-functionalized supports (Liang and Astruc 2011; Nisola et al. 2020; Ouerghui et al. 2016). With the azido-functionalized PVC NF membranes developed in this study, applications that take advantage of nitrene or click reactions might be extended over to membranes, thereby allowing the development of membrane materials with highly specialized functionalities.

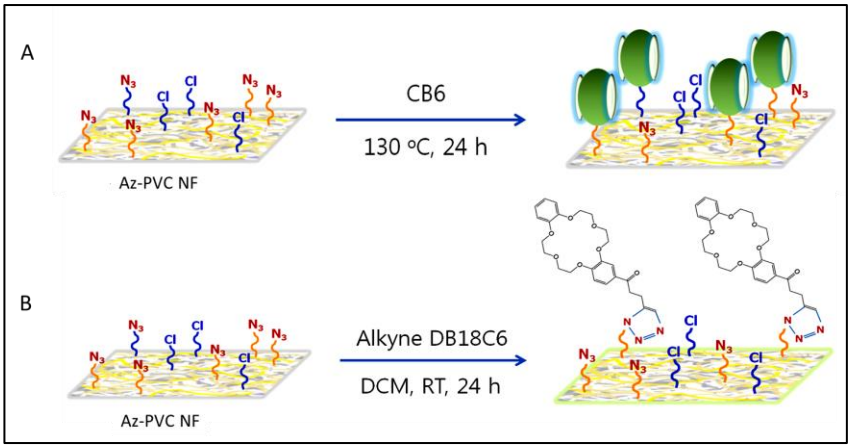

Figure 7. Examples of molecule attachment schemes in Az-PVC NF: (A) nitrene insertion in alkyl chains of cucurbiturils, or (B) click reaction with alkyne-functionalized crown ethers.

FUNDING

This research was supported by the National Research Foundation of Korea (NRF) funded by the Ministry of Science and ICT (2020R1A2C1003560, 2021R1A2C2093746).

ETHICAL CONSIDERATIONS

This research did not require human or animal subjects.

DECLARATION OF COMPETING INTEREST

The authors declare that they have no known competing financial interests or personal relationships that could have influenced the work reported in this paper.

ACKNOWLEDGMENTS

The authors thank the reviewers for their help in improving the manuscript.

REFERENCES

Assaf KL and Nau WM. 2015. Cucurbituril: from synthesis to high-affinity binding and catalysis. Chemical Society Reviews, 44(2): 394-498. https://doi.org/10.1039/C4CS00273C

Buschmann HJ, Cleve E and Schollmeyer E. 1992. Cucurbituril as a ligand for the complexation of cations in aqueous solutions. Inorganica Chimica Acta, 193(1): 93-97. https://doi.org/10.1016/S0020-1693(00)83800-1

Chen K, Kang YS, Zhao Y, Yang JM, Lu Y and Sun WY. 2014. Cucurbit[6]uril-based supramolecular assemblies: possible application in radioactive cesium cation capture. Journal of the American Chemical Society, 136: 16744-16747. https://doi.org/10.1021/ja5098836

Escobar EC, Sio JEL, Bendoy AP, Torrejos REC, Fissaha HT, Kim H, Chung WJ and Nisola GM. 2021. Removal of Cs^+ in water by dibenzo-18-crown-6 ether tethered on mesoporous SBA-15 as a reusable and efficient adsorbent. Journal of Water Process Engineering, 39: 101716. https://doi.org/10.1016/j.jwpe.2020.101716

Escobar EC, Sio JEL, Torrejos REC, Kim H, Chung WJ and Nisola GM. 2022. Organic ligands for the development of adsorbents for Cs^+ sequestration: A review. Journal of Industrial and Engineering Chemistry, 107:1-19. https://doi.org/10.1016/j.jiec.2021.11.039

Lakshmi S and Jayakrishnan A. 2002. Iodination of plasticized poly(vinyl chloride) in aqueous media via phase transfer catalysis. Journal of Applied Polymer Science, 84(3): 493-499. https://doi.org/10.1002/app.10176

Law K-Y. 2014. Definitions for Hydrophilicity, Hydrophobicity, and Superhydrophobicity: Getting the Basics Right. The Journal of Physical Chemistry Letters, 5(4): 686-688. https://doi.org/10.1021/jz402762h

Liang L and Astruc D. 2011. The copper(I)-catalyzed alkyne-azide cycloaddition (CuAAC) "click" reaction and its applications. An overview. Coordination Chemistry Reviews, 225(23-24): 2933-2945. https://doi.org/10.1016/j.ccr.2011.06.028

Nisola GM, Parohinog KJ, Cho MK, Burnea FKB, Lee JY, Seo JG, Lee SP and Chung WJ. 2020. Covalently decorated crown ethers on magnetic graphene oxides as bi-functional adsorbents with tailorable ion recognition properties for selective metal ion capture in water. Chemical Engineering Journal, 389: 123421. https://doi.org/10.1016/j.cej.2019.123421

Ouerghui A, Elamari H, Dardouri M, Ncib S, Meganem F and Girard C. 2016. Chemical modifications of poly(vinyl chloride) to poly(vinyl azide) and "clicked" triazole bearing groups for application in metal cation extraction. Reactive and Functional Polymers, 100: 191-197. https://doi.org/10.1016/j.reactfunctpolym.2016.01.016

Pham LQ, Uspenskaya MV, Olekhnovich RO and Bernal RAO. 2021. A review on electrospun functionalized polyvinyl chloride (PVC) nanofibers: Fabrication, properties, and application. Fibers, 9(2): 12. https://doi.org/10.3390/fib9020012

Schneider C, Rasband W and Eliceiri K. 2012. NIH Image to ImageJ: 25 years of image analysis. Nature Methods, 9: 671–675. https://doi.org/10.1038/nmeth.2089

Sun X, Li B, Wan D and Wang N. 2016. Using a novel adsorbent macrocyclic compound cucurbit[8]uril for Pb^{2+} removal from aqueous solution. Journal of Environmental Sciences, 50: 3-12. https://doi.org/10.1016/j.jes.2016.04.029

ROLE OF AUTHORS: *ECE- methodology, investigation, writing of original draft; GMN- conceptualization, project administration, investigation; WJC- resources, supervision, project administration.*

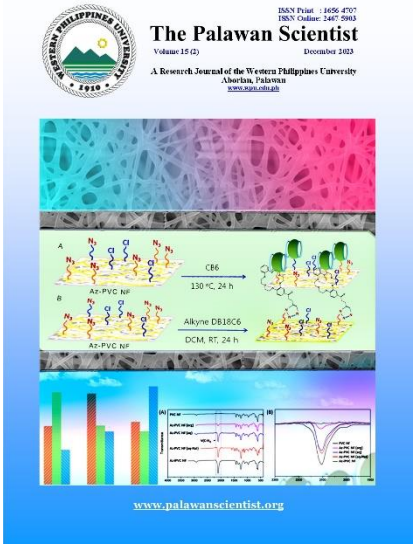

Design of a compact wastewater treatment and isolation of microbial consortia for nutrient reduction of plastic recycling wastewater

Jaren U. Tulipan and Jey-R S. Ventura*

Biomaterials and Environmental Engineering Laboratory, Department of Engineering Science, College of Engineering and Agro-Industrial Technology, University of the Philippines Los Baños, College, Laguna, Philippines
**Correspondence: jsventura@up.edu.ph*

Received: 31 May 2023 || Revised: 03 Oct. 2023 || Accepted: 19 Oct. 2023

ISSN: 1656-4707
E-ISSN: 2467-5903
Homepage: www.palawanscientist.org

How to cite:
Tulipan JU and Ventura JS. 2023. Design of a compact wastewater treatment and isolation of microbial consortia for nutrient reduction of plastic recycling wastewater. The Palawan Scientist, 15 (2): 21-30.

ABSTRACT

The wastewater generated during the plastic recycling is an aspect that is often overlooked in the process. This wastewater contains pollutants that can affect the environment and human health. To address this problem, a study was conducted to design and evaluate the performance of an anoxic-oxic (AO) system and an anoxic-oxic-oxic (AO_2) system in treating plastic recycling wastewater. Additionally, the study collected wastewater from a plastic recycling company and activated sludge from a sewage treatment plant to test the viability of biological treatment for treating plastic recycling wastewater. The results showed that both systems were effective at reducing chemical oxygen demand (COD), with the AO system having a higher percent COD removal (98.13%) than the AO_2 system (85.33%). Also, there were 18 unique colonies isolated from the wastewater and activated sludge. Overall, the study concludes that biological treatment can be used to treat plastic recycling wastewater, and the design of upscaled system is crucial to fully solve the wastewater problem.

Keywords: laboratory scale reactor, recycling industry wastewater, wastewater treatment design

INTRODUCTION

Plastic waste has become a major environmental issue in recent years, with much attention focused on the impact of plastic pollution on the environment and human health. One of the most effective ways to reduce the environmental impact of plastic waste is to recycle it. Plastic recycling is the process of transforming discarded plastic materials into new products that can be used again (Hopewell et al. 2009). However, one aspect of the problem that is often overlooked is the wastewater generated during the plastic recycling process (Gunarathna et al. 2010). The washing stage plays a pivotal role in removing residues such as wood, pulp fibers, food, and adhesives, which otherwise would have detrimental effects on the final regenerated product. Therefore, these washing stages produce vast amounts of wastewater. The current washing technology used by plastic recyclers has significantly reduced water consumption to 2-3 m^3 of water per ton of plastic material (Altieri et al. 2021). This wastewater can contain a variety of hazardous chemicals and contaminants, and if not properly treated, it can have serious negative impacts on the environment and human health (Setiawan et al. 2021).

The composition of wastewater varies depending on the source. Altieri et al. (2021) investigated plastic solid waste washing wastewater and found that it contains high amounts of chemical oxygen demand (COD), biochemical oxygen demand (BOD), and total nitrogen (TN). The high concentration of these pollutants may be attributed to the source of the plastic solid waste, which was mainly from the agro-industrial sector. Setiawan et al. (2021) characterized polyester synthetic fiber industry wastewater and found that it contains high amounts of COD, BOD, and total suspended solids (TSS). Santos et al. (2005) characterized effluents from the washing steps of polyethylene terephthalate (PET) and polyolefins cleaning process, while Santhmayor et al. (2020) characterized wastewater from waste plastic recycling machines. Both studies indicated high amounts of COD and TSS in the wastewater. The high COD values may be attributed to the surfactant used in the washing step of the plastics (Santos et al. 2005). Meanwhile, Kolbl (2016) characterized plastic processing plant wastewater and found a high amount of total phosphorous (TP). The above findings show that plastic recycling wastewater can have high amounts of COD, BOD, TP, TN, and TSS. High levels of these pollutants may cause nitrate contamination, eutrophication, and ammonia toxicity (Curtin et al. 2011). Additionally, high levels of TSS may cause problems for aquatic life as TSS may include solids from the plastic recycling wastewater that can harm the environment (Santhmayor et al. 2020). These results show proof that plastic recycling wastewater can be harmful. Therefore, proper treatment of plastic recycling wastewater is essential to prevent these negative impacts.

Plastic recycling wastewater poses harmful effects on the environment, and there is still a lack of available and cost-effective technology for the plastic recycling industry to implement. In the case of Valenzuela City, Philippines, the researchers found that most plastic recycling facilities do not have the necessary equipment or infrastructure to properly treat wastewater. Most of the facilities reuse their wastewater without treatment to cut operating costs. This is not only hazardous but also decreases the quality of recycled plastic (Altieri et al. 2021). Efforts to mitigate the effects of this in the wastewater were made by applying flocculation methods. However, the lack of knowledge on wastewater composition and appropriate treatment system makes it difficult to assess.

To address this problem, this study aimed to design and evaluate the performance of an anoxic-oxic (AO) system and an anoxic-oxic-oxic (AO_2) system in treating plastic recycling wastewater. These systems were investigated for their potential to enhance biological nutrient removal from plastic recycling wastewater. Also, developing these systems ensures a low-cost technology that can be adapted by the plastic recycling industry. The specific objectives were the following: (1) to characterize the wastewater generated by a local plastic recycling facility in Valenzuela City, Philippines; (2) to isolate and assess the potential of microbial consortia found in activated sludge for the purpose of treating plastic recycling wastewater; and (3) to determine the removal efficiencies and COD reduction performance of the AO and AO_2 systems. Through these objectives, the study sought to contribute valuable insights into the treatment of plastic recycling wastewater.

METHODS

Wastewater Collection and Characterization

Twenty liters of wastewater from a plastic recycling company in Valenzuela City, Philippines were collected and stored. The wastewater was subjected to analysis using standard methods for the examination of water and wastewater to determine the following parameters: COD, BOD, nitrates, phosphates, TSS, pH, and dissolved oxygen.

Sludge Collection and Acclimatization

Similarly, 20-L of activated sludge were collected from a sewage treatment plant in Biñan, Laguna, Philippines, and divided into two setups for acclimatization in synthetic wastewater. One setup was anoxic, while the other was aerobic using an aquarium pump for aeration. The synthetic wastewater used is composed of 5 g L^{-1} glucose, 1 g L^{-1} NH_4Cl, 1 g L^{-1} Na_2CO_3, 1 g L^{-1} $NaHCO_3$, 0.2 g L^{-1} K_2HPO_4, and 1 mL L^{-1} of trace metal solution (Alzate-Gavira et al. 2003). To maintain the culture setups, synthetic wastewater was regularly replaced.

Isolation of Bacteria from the Activated sludge

Microbial preservation and isolation. To have a starting culture for the wastewater treatment facility, the microbial consortia from the activated sludge were isolated and stored. Ten mL samples were taken from the treated wastewater, the mixed liquor from the anoxic setup, and the settled activated sludge solution. The samples were stored in 2-mL centrifuge tubes. Then, serial dilution of each sample was done up to 10^{-5} dilutions. Plate count agar (PCA) was prepared to serve as the growth medium for the microorganisms in the activated sludge because it is usually used for bacterial enumeration in water and wastewater (Aryal 2022; Ogodo et al. 2022). It is composed of 5 g L^{-1} casein hydrolysate, 2.5 g L^{-1} yeast extract, 1 g L^{-1} glucose, and 15 g L^{-1} agar.

After which, the pour plate method was then used. Four plates of treated wastewater, an anoxic setup of mixed liquor, and an activated sludge solution were made. Then, two plates of each were placed in a

desiccator to create an anaerobic condition. The other two plates of each were placed in storage to facilitate aerobic conditions. Under these conditions, the microorganisms were allowed to grow for two days.

Luria Bertani (LB) broth was prepared to serve as the medium for the growth cultivation of bacteria found in the plates. It is composed of 100 g L^{-1} casein hydrolysate, 50 g L^{-1} yeast extract, and 60 g L^{-1} glucose. The bacteria colonies found in each plate were placed on test tubes filled with 15 mL of LB broth. Two test tubes of colonies found from treated wastewater, anoxic setup mixed liquor, and activated sludge solution were placed in a desiccator to facilitate anaerobic conditions. The other two test tubes were placed in storage to facilitate aerobic conditions. The bacteria were allowed to grow for three days. After which, glycerol stocks were made from each test tube. The isolates were then stored at 4°C with 1 mL of LB broth and 1 mL of glycerol.

Regrowing and characterization of the stock inoculum. Plate count agar with nystatin (10,000 units ml^{-1}) was prepared and served as a medium for growth for the microbial consortia plates. Nystatin was added to ensure that only bacteria would grow on the PCA plates. A total of 24 plates of PCA were prepared. Four plates were prepared for both anaerobic and aerobic setups for treated wastewater, anoxic setup mixed liquor, and activated sludge solution. The plates were incubated in an anaerobic (using a desiccator) and aerobic condition for approximately 4 days to allow the bacteria to grow.

Colonies were identified based on their observed characteristics on the plates. Gram staining was done to further characterize the unique bacteria colonies by their cell membrane structures. The gram-stained bacteria were observed under a microscope.

AO and AO_2 Reactor Design and Fabrication

AO system. A laboratory-scale AO system was designed to determine the COD reduction of the system using the activated sludge. Design considerations were as follows. The volume of the oxic chamber and the anoxic chamber was determined in the ratio of 1:2. The height of the reactor was set to 120 mm, which is roughly the same height as a 250-mL beaker. The width of the reactor was set to 68 mm to fit a magnetic stirrer inside the reactor. To achieve a 1:2 volume ratio for the oxic and anoxic chambers, the length of each chamber was set to 68 mm and 136 mm, respectively. Alternating hanging and standing baffles were placed inside the reactor to compartmentalize the reactors and regulate the flow of liquid from the anoxic chamber to the oxic chamber. The baffles are 3 mm thick and have vertical clearances of 20 mm. The reactor was fabricated by 3D printing using Creality CR-10 Max. The 3D printing parameters were based on the study of Nasr Esfahani et al. (2021) using polylactic acid (PLA) filament for the printing process. The wall thickness of the reactor was set to 4 mm, and the base thickness was set to 10 mm. The infill pattern was set to tri-hexagon with an infill density of 75% (Nasr Esfahani et al. 2021). An outlet was placed at the same height as the standing baffle. The 3D model of the fabricated AO reactor is shown in Figure 1.

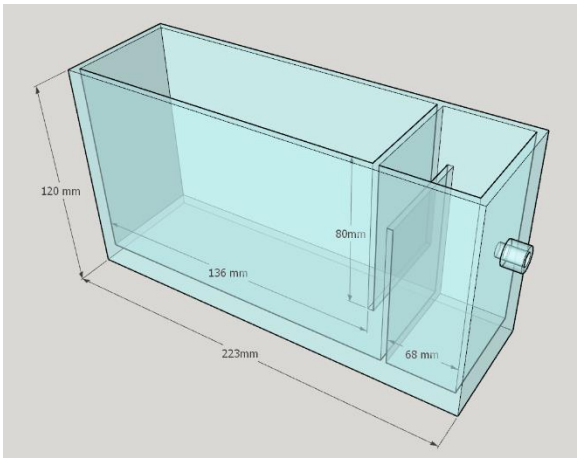

Figure 1. 3D model of the fabricated anoxic-oxic reactor.

The AO system configuration is depicted in Figure 2. The hydraulic retention time (HRT) for the anoxic chamber was set to 16 hr and the HRT for the oxic chamber was set to 8 hr. Meanwhile, the pH and the temperature in both the anoxic and oxic chambers were set at pH 7 and 25°C. Meanwhile, the influent flowrate and the effluent flowrate were both set at 1 m^3 d^{-1}.

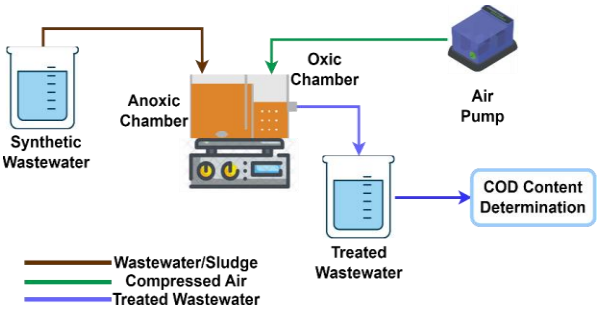

Figure 2. Anoxic-oxic system configuration.

AO_2 system. From the results of the AO laboratory scale reactor, it was determined to improve the system configuration by adding another oxic chamber to the design. With this, an AO_2 laboratory scale reactor with cascading baffles was designed. The height of the reactor was set to 70 mm. The wall thickness of the reactor was set to 4 mm, while the base thickness was set to 5 mm. The reactor consists of three chambers – one anoxic chamber and two oxic chambers. The chambers were equal in area, with

length and width measuring 62.5 mm and 60 mm, respectively. Alternating hanging and standing baffles were designed to compartmentalize the chambers and regulate the wastewater flow. The standing baffles were designed to have a 5 mm decrease in height to facilitate cascading flow from one chamber to the next. The standing baffle heights were 60 mm and 55 mm with a vertical clearance of 20 mm. A single outlet was placed at the same height as the last standing baffle and has an inner diameter of 10 mm.

A 3D printed laboratory scale reactor was used in the setup. The infill design was chosen to be tri-hexagon to have better 2D stress management. The infill density was set to be 60%, which was found to be sturdy enough to prevent any leakages based on previous test prints. The 3D model of the fabricated AO_2 reactor is shown in Figure 3. The AO_2 system configuration is shown in Figure 4. The hydraulic retention time (HRT) for the anoxic and two oxic chambers was set to 8 hr. The pH and the temperature in all the chambers were set at pH 7 and 25°C, respectively. Meanwhile, the influent flowrate and the effluent flowrate were both set at 1 m^3 d^{-1}.

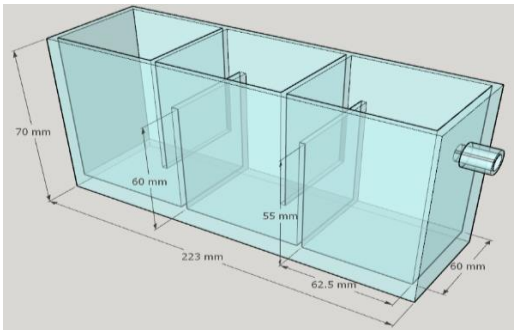

Figure 3. 3D model of the fabricated anoxic-oxic-oxic reactor.

Chemical Oxygen Demand Reduction Performance

A10-L container containing synthetic wastewater served as the influent into the system. The wastewater was continuously fed to the reactors at a rate of 1 L day^{-1}. The collected activated sludge was placed in the different chambers of the reactor. An air stone was placed in the oxic chamber that was connected to an air pump, which served as the air supply for the oxic chamber, while a magnetic stirrer was placed inside the anoxic chamber.

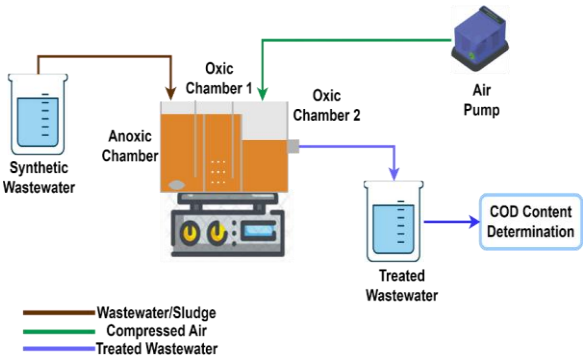

Figure 4. Anoxic-oxic-oxic system configuration.

Meanwhile, the COD of the influent and effluent were measured using the dinitrosalicylic acid (DNS) method, which is based on the National Renewable Energy Laboratory's method for measuring cellulase activity (Adney and Baker 2008). The DNS method was used to determine the COD reduction performance of the reactors by assuming that the glucose content measured by the DNS method is equal to the COD content of the samples. The theoretical COD can be calculated based on the combustion reaction of glucose and oxygen to produce carbon dioxide and water, as seen in Equation 1. Then the theoretical COD can be calculated using Equation 2. Using Equation 2, it can be calculated that for 1000 ppm of glucose, the COD is approximately 1067 ppm. Equation 3 shows the standard curve equation used to determine the COD of the samples for this experiment. The COD reduction rate and percent COD reduction were calculated using Equations 4 and 5.

$$C_6H_{12}O_6 + 6O_2 \rightarrow 6CO_2 + 6H_2O \qquad (Equation\ 1)$$

$$Theoretical\ COD = mol\ oxidizable\ material\ x\ \frac{mol\ O_2}{mol\ oxidizable\ material}\ x\ MM\ O_2 \qquad (Equation\ 2)$$

$$Absorbance\ (nm) = 0.1396 + 0.5827 * COD\ (g\ L^{-1}) \qquad (Equation\ 3)$$

$$COD\ reduction\ rate = \frac{Initial\ COD\ concentration - Final\ COD\ Concentration}{Final\ time - initial\ time} \qquad (Equation\ 4)$$

$$\%\ COD\ reduction = \frac{Initial\ COD\ concentration - Final\ COD\ Concentration}{Initial\ COD\ Concentration}\ x\ 100 \qquad (Equation\ 5)$$

The reagent for the DNS method was prepared by adding the following chemicals to 1 L of distilled water: 7.5 g dinitrosalicylic acid, 14 g NaOH, 216 g $KNaC_4H_4O_6 \cdot 4H_2O$, 5.4 mL phenol, and 5.9 g $Na_2S_2O_5$. A 1.5 mL of this reagent was then mixed with 0.75 mL of wastewater. The mixture was then heated at 100°C for 5 min and cooled in an ice water bath to develop color. The absorbance of this color was then measured using a spectrophotometer at 540 nm and compared to a standard curve to determine the COD concentration in the wastewater. The standard curve was generated by making standard solutions of glucose with concentrations of 0.2 g L^{-1} to 1.2 g L^{-1}.

RESULTS

Plastic Recycling Wastewater Characteristics

The collected wastewater from the plastic recycling industry was subjected to wastewater characteristic analysis using standard methods. The results are shown in Table 1. From the table, the BOD, nitrate, phosphate and TSS concentration in the wastewater were 651 mg L^{-1}, 337 mg L^{-1}, 3.16 mg L^{-1}, and 338 mg L^{-1} respectively. Meanwhile, the COD concentration of the wastewater was 5682 mg L^{-1}. Fecal coliform was also found in the wastewater at 1.8 MPN per 100 mL. The color of the wastewater was measured at 25 TCU. The pH and temperature of the wastewater were 6.47 and 28.2 °C, respectively.

Bacterial Isolates from Activated Sludge

Tables 2 and 3 summarize the colony and bacterial characteristics observed in the isolates. In total, 18 unique isolates were observed. Seven aerobic isolates were identified from the PCA plates while eleven anaerobic isolates were identified from the PCA plates.

Performance of the AO and AO_2 System

The percent COD reduction and the COD reduction rate of the AO system are shown in Figure 5. The figure shows that on the first day, there was a COD reduction rate of 60.42 mg L^{-1} h^{-1}, which translates to a 99.01% reduction. This high reduction rate was maintained throughout the process. Overall, the process was highly effective, with all reduction rates above 92%. Meanwhile, the percent COD reduction and the COD reduction rate of the AO_2 system are shown in Figure 6. The figure shows that the system was stable at the start of the experiments but was unstable towards the end. The AO system showed a more stable treatment efficiency as compared to the AO_2 system in terms of COD reduction performance.

Table 1. Wastewater characteristics of plastic recycling industry effluent as compared to DENR general effluent standards. SM – standard methods for the examination of water and wastewater.

Analysis	Method	Unit	Wastewater	DENR GES Class C
Fecal Coliform	SM 9221 E	MPN per100 mL	1.8	400
Color	SM 2120 B	TCU	25	150
Nitrate	SM 4500 – NO_3 E.	mg L^{-1}	337	14
COD	SM 5220 B	mg L^{-1}	5682	100
BOD	SM 5210 B.	mg L^{-1}	651	50
TSS	SN 2540 D.	mg L^{-1}	338	100
Phosphate	SN 4500-P D.	mg L^{-1}	3.16	4
pH	-	pH	6.47	6.0-9.5
Temperature	-	°C	28.2	25-31

Table 2. Colony and bacterial characteristics of isolates from aerobic conditions.

Isolate	Colony Characteristics			Bacterial Characteristics	
	Color	Form	Elevation	Gram Stain	Shape
WW O_2 1	Creamy	Circular	Raised	Gram-negative	Rod
WW O_2 2	White	Circular	Flat	Gram-negative	Rod
WW O_2 3	Bright Orange	Circular	Raised	Gram-negative	Rod
WW O_2 4	Whitish Yellow	Circular	Flat	Gram-positive	Rod
Sol'n O_2 1	Creamy	Irregular	Flat	Gram-negative	Rod
Sol'n O_2 2	Whitish Yellow	Irregular	Flat	Gram-positive	Rod
Iso 1 O_2	White	Circular	Raised	Gram-positive	Cocci

Table 3. Colony and bacterial characteristics of isolates from anaerobic conditions.

Isolate	Colony Characteristics			Bacterial Characteristics	
	Color	Form	Elevation	Gram Stain	Shape
Sol'n An 1	Creamy	Circular	Flat	Gram-negative	Cocci
Sol'n An 2	White	Circular	Flat	Gram-negative Gram-positive	Rod Cocci
Sol'n An 3	Yellow	Circular	Flat	Gram-positive	Rod
WW An 1	White	Circular	Flat	Gram-negative	Rod
WW An 2	Creamy	Circular	Flat	Gram-negative Gram-positive	Rod Cocci
WW An 3-1	Creamy	Circular	Flat	Gram-negative	Rod
WW An 3-2	Yellow	Circular	Raised	Gram-negative	Rod
WW An 4	Yellow	Circular	Flat	Gram-negative	Rod
Sludge An 1	Creamy	Irregular	Flat	Gram-negative	Cocci
Sludge An 2	Creamy	Irregular	Flat	Gram-negative Gram-positive	Rod Rod
Iso 2 An	Faint Orange	Circular	Flat	Gram-negative	Cocci

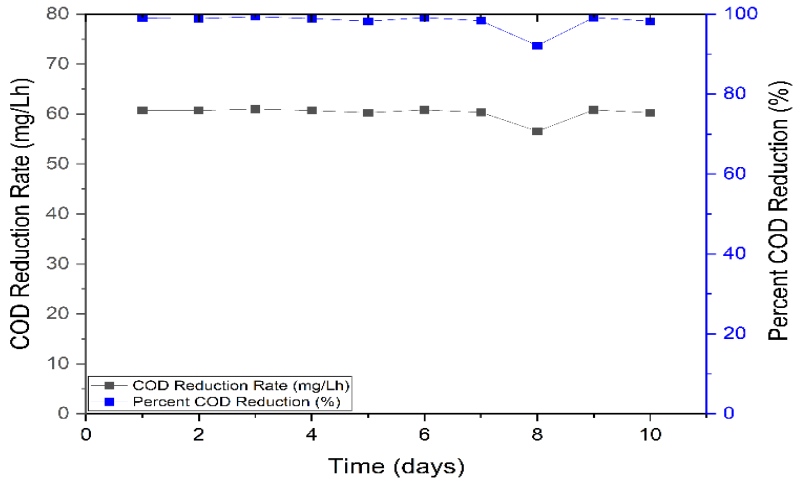

Figure 5. Chemical Oxygen Demand reduction performance of Anoxic-oxic system.

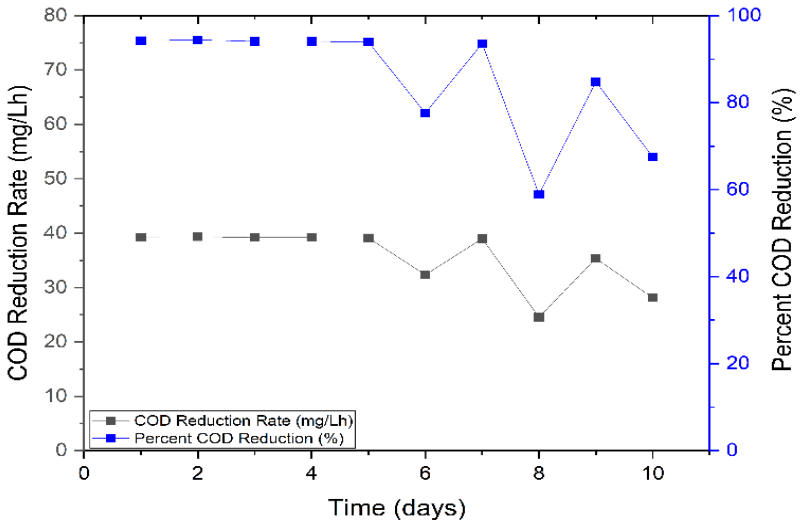

Figure 6. Chemical Oxygen Demand reduction performance of the Anoxic-oxic-oxic system.

DISCUSSION

Plastic Recycling Wastewater Characteristics

Table 1 shows the wastewater characteristics of the plastic recycling wastewater from local plastic recycling facilities in the Philippines as compared to the Class C general effluent guidelines set by the DENR. The plastic recycling industry falls under the Philippine Standard Industrial Classification Code (PSIC Code) 38210. Based on DENR Administrative Order 2016-08, the significant parameters that should be monitored for the effluent of industries under PSIC Code 38210 are pH, temperature, color, COD, total coliform, ammonia, nitrate, phosphate, and TSS. The BOD in the wastewater (651 mg L^{-1}) was significantly higher than the effluent standard set by the Department of Environment and Natural Resources (DENR) (50 mg L^{-1}). This result indicates that the wastewater has a high level of organic matter, which can deplete oxygen levels in water bodies. The COD of the wastewater (5682 mg L^{-1}) was also found to be significantly higher than the DENR effluent standard (100 mg L^{-1}). This high COD level suggests a substantial presence of organic pollutants in the wastewater, which can have adverse effects on the receiving water bodies (Tchobanoglous et al. 2003). Also, nitrate concentration in the wastewater (337 mg L^{-1}) was above the DENR effluent standard (14 mg mg L^{-1}). High levels of nitrates can pose a risk to aquatic life and can also contaminate groundwater (Tay et al. 2003). The total suspended solids (TSS) of the wastewater (338 mg L^{-1}) also exceeded the DENR effluent standard (100 mg L^{-1}). High levels of TSS can reduce the clarity of water, making it unsuitable for various purposes, including industrial and agricultural uses (Tchobanoglous et al. 2003). The phosphate concentration (3.16 mg L^{-1}) was observed to be barely below the DENR effluent standard (4 mg L^{-1}). High levels of phosphate can lead to eutrophication, which can cause algae blooms and oxygen depletion in water bodies (Tay et al. 2003). The fecal coliform, color, pH, and temperature of the plastic recycling wastewater were well below the effluent standards. However, it has higher concentrations of nitrates (337 mg L^{-1}), BOD (651 mg L^{-1}), TSS (338 mg L^{-1}), and phosphates (3.16 mg L^{-1}) than the general effluent standards. This data proves that it is unsafe to discharge wastewater from these industries without proper treatment.

The plastic recycling wastewater from the local industry had higher concentrations of COD than the wastewater from all the characterized wastewaters (Table 4). Also, this wastewater had higher BOD than the wastewater from the studies of Kolbl (2016) and Setiawan et al. (2021). The plastic recycling wastewater also had higher concentrations of nitrates than the study of Altieri et al. (2021). However, it also contains lower concentrations of phosphates than the wastewater from the study of Kolbl (2016) and had a lower pH than all the wastewater (Table 4).

Table 4. Wastewater characteristics of plastic recycling industry wastewater from different sources.

Source	Wastewater	COD (mg L^{-1})	TSS (mg L^{-1})	BOD_5 (mg L^{-1})	TN (mg L^{-1})	TP (mg L^{-1})	NO_2-N (mg L^{-1})	NO_3-N (mg L^{-1})	NH_3-N (mg L^{-1})	pH
Altieri et al. (2021)	Plastic solid waste washing wastewater	1371.5	-	398	45.35	8.4	0.1	0.55	22.75	7.6
Setiawan et al. (2021)	Polyester synthetic fiber industry wastewater	579	269	264	-	-	-	-	5.4	-
Santos et al. (2005)	Effluents from washing steps of polyethylene terephthalate (PET) and polyolefins cleaning process	677.5	702.5	-	-	-	-	-	-	9.45
Ramirez-Camperos et al. (2004)	Bottle washings wastewater from soft drinks industry	64.9	66	-	-	-	-	-	-	11.5
Santhmayor et al. (2020)	Wastewater from waste plastic recycling machines	354	400	-	-	-	-	-	-	7.9
Kolbl (2016)	Plastic processing plant wastewater	457	294.3	112.3	-	933.3	248.3	940	456.3	7.6

Isolated Bacteria in Activated Sludge

There are seven unique bacteria colonies identified in aerobic plates. There are four gram-negative bacterial isolates and three gram-positive bacterial isolates from the aerobic conditions. The color of the colonies of these isolates ranges from white to yellow. Most isolates found in aerobic conditions are rod-shaped with one isolate having a cocci shape. The bacteria colonies isolated from aerobic plates are potential nitrifying bacteria as well as biological phosphorous removal bacteria (Tay et al. 2003). Meanwhile, there are 11 unique bacterial colonies identified in anaerobic plates. Seven are found to be gram-negative while the other four are gram-positive. The color of the colony of these isolates ranges from white to yellow as well. Five isolates have a cocci shape, while the rest are rod-shaped. These bacterial colonies in anaerobic plates can serve as denitrifiers in the anoxic or anaerobic chambers of wastewater treatment (Tay et al. 2003). The presence of both aerobic and anaerobic bacterial colonies gives insight into an effective biological treatment of wastewater.

Out of the 18 isolates, 11 are gram-negative and 7 are gram-positive. The majority of the isolates being gram-negative is an indication that the bacterial community found in the activated sludge is composed of bacteria that are commonly found in wastewater treatment facilities. *Proteobacteria, Bacteroidetes, Chloroflexi*, and *Acidobacteria* are generally found in wastewater treatment systems and are gram-negative (Hu et al. 2012). Meanwhile, the gram-positive isolates may be due to fecal coliforms such as *Enterococcus faecalis* (He et al. 2021).

Chemical Oxygen Demand Reduction Performance of the AO and AO_2 Systems

The laboratory-scale reactors were used to treat synthetic wastewater. Chemical oxygen demand was measured every day for 10 days using the DNS method. The AO system had a minimum COD reduction rate of 56.20 mg L^{-1} h^{-1}, a maximum of 60.24 mg L^{-1} h^{-1}, and a mean of 59.88 mg L^{-1} h^{-1}. The system also had a minimum removal of 92.10% COD, a maximum of 99.37%, and a mean of 98.13%. The AO system showed performance stability during the 10-day experiment with a decrease in both the COD reduction rate and percent COD removal on the 8th day. However, it stabilized again to a comparable COD reduction rate and percent COD removal on the 9th and 10th day.

Meanwhile, the AO_2 system had a minimum reduction rate of 24.55 mg l^{-1} h^{-1} COD, a maximum of 39.35 mg L^{-1} h^{-1}, and a mean of 35.55 mg L^{-1} h^{-1}. The system also had a minimum removal of 58.92% COD, a maximum of 94.44%, and a mean of 85.33%. The AO_2 system showed performance stability until the 5th day. However, it experienced an erratic performance from the 6th day to the 10th day, with a characteristic decrease and then an increase in both the COD reduction rate and percent COD reduction. The erratic performance may be due to the change in pH in the reactor from the 6th day until the 10th day of the experiment.

Overall, the AO system performed better than the AO_2 system in removing COD from the wastewater. The percent COD removal of the AO system as compared to other systems has a comparable percent COD removal. In Table 5, a comparable percent COD removal was observed in the treatment of raw washing wastewater using a sequencing batch biofilter granular reactor with a removal of 95.24% COD and in the treatment of synthetic wastewater using an intermittently aerated and decanted single-reactor process with a removal of 95% COD (Yoo et al. 1999; Altieri et al. 2021). Meanwhile, the AO_2 system has comparable percent COD removal performance with the coagulation-flocculation process, with 82.58% COD removal (Setiawan et al. 2021). Both the AO system and the AO_2 system have significant COD reduction rates compared to other systems (Balku 2007; Munz et al. 2007; Liu et al. 2013; Kim et al. 2019; Nikmanesh et al. 2018; Altieri et al. 2021).

The above results showed the potential of biological treatment for treating plastic recycling wastewater. To further enhance the removal efficiencies of biological treatment systems, it is recommended to examine and optimize the different operating parameters of the systems, such as the pH, the HRT, the dissolved oxygen content, and the influent flowrate of the system. It is also important to upscale the system and evaluate and validate the laboratory results as compared to pilot-scale treatment efficiencies.

FUNDING

This research is funded by the Department of Science and Technology (DOST) - Philippine Council for Industry, Energy and Emerging Technology Research and Development (PCIEERD).

ETHICAL CONSIDERATIONS

No human or animals were involved in the conduct of the study.

DECLARATION OF COMPETING INTEREST

The authors declare that there are no competing interests for any authors.

Table 5. Chemical oxygen demand (COD) and percent COD removal of different systems from various sources.

Wastewater	System	COD Reduction Rate ($mg\ L^{-1}\ h^{-1}$)	Percent COD Removal	Source
Raw washing wastewater	Sequencing batch biofilter granular reactor (SBBGR)	27.00	95.24	Altieri et al. (2021)
Tannery wastewater	Activated sludge process that was enhanced by coagulation and reverse osmosis	123.97	67.00	De Gisi et al. (2009)
Septic tank effluent	Circulating fluidized bed bioreactor	18.23	78.48	Liu et al. (2013)
Polyester synthetic fiber industry wastewater	Coagulation-flocculation	209.42	82.58	Setiawan et al. (2021)
Tannery wastewater	Powdered activated carbon and membrane bioreactors (MBRPAC)	42.92	79.46	Munz et al (2007)
Synthetic wastewater	Intermittently aerated and decanted single-reactor process	12.44	95.00	Yoo et al. (1999)
Synthetic wastewater	Conventional activated sludge system	32.46	70.11	Balku (2007)
Municipal wastewater	Circulating fluidized bed bioreactor	126.29	92.08	Patel et al. (2006)
Actual WWTP influent	Aerobic-anoxic process	10.54	89.53	Kim et al. (2019)
	Activated sludge process	8.86	75.19	
Municipal wastewater	UASB (Upflow anaerobic sludge blanket) - Activated sludge system	61.42	89.67	Von Sperling et al. (2001)
Municipal wastewater	Extended aeration activated sludge system	2.21	61.40	Nikmanesh et al. (2018)
Synthetic plastic recycling wastewater	Anoxic-oxic system	59.88	98.13	This study
Synthetic plastic recycling wastewater	Anoxic-oxic-oxic system	35.55	85.33	

ACKNOWLEDGMENTS

This study is part of the DOST PCIEERD funded project entitled "ENVITECS: NanoSiliCage (NSC): Nanocaged silicate composite for treatment of wastewater from Valenzuela City plastic industries" in collaboration with Material Science and Engineering Program – UP Diliman and Department of Engineering Science – UP Los Baños. We also want to express our gratitude to the reviewers for their insightful comments and suggestions, which helped us improve the quality of our research paper.

REFERENCES

Adney B and Bake J. 2008. Measurement of Cellulase Activities Laboratory Analytical Procedure (LAP). U.S. Department of Energy and Office of Energy Efficiency and Renewable Energy. 8pp. https://www.nrel.gov/docs/gen/fy08/42628.pdf . Accessed on 22 May 2023.

Altieri VG, De Sanctis M, Sgherza D, Pentassuglia S, Barca E and Di Iaconi C. 2021. Treating and reusing wastewater generated by the washing operations in the non-hazardous plastic solid waste recycling process: Advanced method vs. Conventional method. Journal of Environmental Management, 284: 112011. https://doi.org/10.1016/j.jenvman.2021.112011

Alzate-Gaviria LM, Pérez-Hernández A, Nevárez-Moorillón VG, Rinderknecht-Seijas N and Poggi-Varaldo HM. 2003. Comparison of two anaerobic coupled systems for biomethanization of the organic fraction of municipal solid wastes. Interciencia, 28(8): 436-490.

Aryal S. 2022. Plate Count Agar (PCA)- Composition, Principle, Preparation, Results, Uses. https://microbenotes.com/plate-count-agar-pca/ Accessed on 29 May 2023.

Balku S. 2007. Comparison between alternating aerobic–anoxic and conventional activated sludge systems. Water Research, 41(10): 2220–2228. https://doi.org/10.1016/j.watres.2007.01.046

Curtin K, Duerre S, Fitzpatrick B and Meyer P. 2011. Biological nutrient removal manual. https://www.pca.state.mn.us/sites/default/files/wq-wwtp8-21.pdf. Accessed on 29 May 2023.

De Gisi S, Galasso M and De Feo G. 2009. Treatment of tannery wastewater through the combination of a conventional activated sludge process and reverse osmosis with a plane membrane. Desalination, 249(1): 337–342. https://doi.org/10.1016/j.desal.2009.03.014

Gunarathna GPN, Bandara NJGJ and Liyanage S. 2010. Analysis of Issues and Constraints Associated with Plastic Recycling Industry in Sri Lanka. Department of Forestry and

Environmental Science University of Sri Jayewardenepura, Nugegoda, Sri Lanka, 11pp.

He J, Zheng Z and Lo IMC. 2021. Different responses of gram-negative and gram-positive bacteria to photocatalytic disinfection using solar-light-driven magnetic TiO2-based material, and disinfection of real sewage. Water Research, 207: 117816. https://doi.org/10.1016/j.watres.2021.117816

Hopewell J, Dvorak R and Kosior E. 2009. Plastics recycling: Challenges and opportunities. Philosophical Transactions of the Royal Society B: Biological Sciences, 364(1526): 2115–2126. https://doi.org/10.1098/rstb.2008.0311

Hu M, Wang X, Wen X and Xia Y. 2012. Microbial community structures in different wastewater treatment plants as revealed by 454-pyrosequencing analysis. Bioresource Technology, 117: 72–79. https://doi.org/10.1016/j.biortech.2012.04.061

Kolbl S. 2016. Biological wastewater treatment of different organic loading from recycling and fabrication plant of PET, HDPE and LDPE plastic products. Acta Hydrotechnica, 29(51): 125-143.

Kim IT, Lee YE, Yoo YS, Jeong W, Yoon YH, Shin DC and Jeong Y. 2019. Development of a combined aerobic–anoxic and methane oxidation bioreactor system using mixed methanotrophs and biogas for wastewater denitrification. Water, 11(7): 1377. https://doi.org/10.3390/w11071377

Liu G, Xu X, Zhu L, Xing and Chen J. 2013. Biological nutrient removal in a continuous anaerobic–aerobic–anoxic process treating synthetic domestic wastewater. Chemical Engineering Journal, 225: 223–229. https://doi.org/10.1016/j.cej.2013.01.098

Munz G, Gori R, Mori G and Lubello C. 2007. Powdered activated carbon and membrane bioreactors (MBRPAC) for tannery wastewater treatment: long term effect on biological and filtration process performances. Desalination, 207(1–3): 349–360. https://doi.org/10.1016/j.desal.2006.08.010

Nasr Esfahani K, Zandi MD, Travieso-Rodriguez JA, Graells M and Pérez-Moya M. 2021. Manufacturing and Application of 3D Printed Photo Fenton Reactors for Wastewater Treatment. International Journal of Environmental Research and Public Health, 18(9): 4885. https://doi.org/10.3390/ijerph18094885

Nikmanesh M, Eslami H, Momtaz SM, Biabani R, Mohammadi A, Shiravand B and Mahmoudabadi TZ. 2018. Performance evaluation of the extended aeration activated sludge system in the removal of physicochemical and microbial parameters of municipal wastewater: a case study of Nowshahr wastewater treatment plant. Journal of Environmental Health Sustainable Development, 3(2): 509-17

Ogodo AC, Agwaranze DI, Daji M and Aso RE. 2022. Chapter 13 - Microbial techniques and methods: basic techniques and microscopy. In: Egbuna C, Patrick-Iwuanyanwu KC, Shas MA and Ifemeje JC (eds). Analytical Techniques in Biosciences: From Basics to Applications. Elsevier Science, Amsterdam, The Netherlands. pp 201-220. https://doi.org/10.1016/B978-0-12-822654-4.00003-8

Patel A, Zhu J and Nakhla G. 2006. Simultaneous carbon, nitrogen and phosphorous removal from municipal wastewater in a circulating fluidized bed bioreactor. Chemosphere, 65(7): 1103–1112. https://doi.org/10.1016/j.chemosphere.2006.04.047

Ramirez Camperos E, Mijaylova Nacheva P and Diaz Tapia E. 2004. Treatment techniques for the recycling of bottle washing water in the soft drinks industry. Water Science and Technology, 50(2): 107–112. https://doi.org/10.2166/wst.2004.0101

Santhmayor KD, Shiri ND, Asiya I, Krafft MS and Thurm W. 2020. Development of water filtration unit for wastewater generated from waste plastics recycling machines. AIP Conference Proceedings. 15pp.

Santos ASF, Teixeira BAN, Agnelli JAM and Manrich S. 2005. Characterization of effluents through a typical plastic recycling process: An evaluation of cleaning performance and environmental pollution. Resources, Conservation and Recycling, 45(2): 159–171. https://doi.org/10.1016/j.resconrec.2005.01.011

Setiawan Y, Taufik Rizaludin A, Nur Aini M and Saepuloh S. 2021. Chemical Treatment in Industrial Wastewater of Polyester Synthetic Fiber Made from Recycled Polyethylene Terephthalate Bottles: Minimize Environmental Impacts. Iranian Journal of Energy and Environment, 12(3): 192–197. https://doi.org/10.5829/IJEE.2021.12.03.02

Tay JH, Chui PC and Li H. 2003. Influence of COD:N:P Ratio on Nitrogen and Phosphorus Removal in Fixed-Bed Filter. Journal of Environmental Engineering, 129(4): 285–290. https://doi.org/10.1061/(ASCE)0733-9372(2003)129:4(285)

Tchobanoglus G, Burton F and Stensel HD. 2003. Wastewater engineering: treatment and reuse. American Water Works Association. Journal, 95(5): 201.

von Sperling M, Freire VH and de Lemos Chernicharo CA. 2001. Performance evaluation of a UASB - activated sludge system treating municipal wastewater. Water Science and Technology, 43(11): 323–328. https://doi.org/10.2166/wst.2001.0698

Yoo H, Ahn KH, Lee HJ, Lee KH, Kwak YJ and Song KG. 1999. Nitrogen removal from synthetic wastewater by simultaneous nitrification and denitrification (SND) via nitrite in an intermittently-aerated reactor. Water Research, 33(1): 145–154. https://doi.org/10.1016/S0043-1354(98)00159-6

ROLE OF AUTHORS: *JUT - data collection, data gathering, data analysis, manuscript writing, and editing; JSV – conceptualization, supervision, manuscript writing, and editing.*

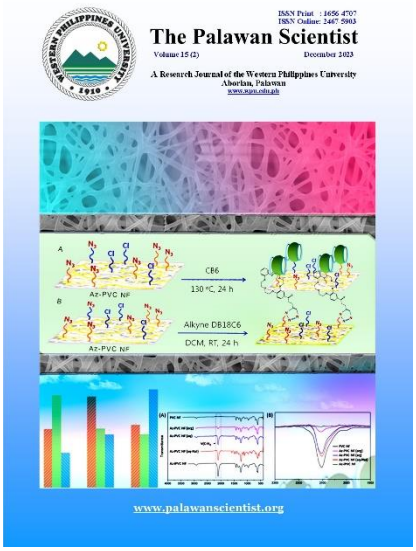

Selected physiological requirements of Purple non-sulfur bacteria isolated from Los Baños, Laguna for potential biohydrogen production

Leo Agustin F. Barcelo[1], Nacita B. Lantican[2], Ruby Lynn G. Ventura[3] and Jey-R S. Ventura[1]*

[1]Department of Engineering Science, University of the Philippines Los Baños
[2]Institute of Biological Sciences, University of the Philippines Los Baños
[3]UP Rural High School, Los Baños, Laguna
**Correspondence: jsventura@up.edu.ph*

Received: 31 May 2023 || Revised: 17 Oct. 2023 || Accepted: 10 Nov. 2023

ISSN: 1656-4707
E-ISSN: 2467-5903
Homepage: www.palawanscientist.org

How to cite:

Barcelo LAF, Lantican NB, Ventura RLG and Ventura JS. 2023. Selected physiological requirements of Purple non-sulfur bacteria isolated from Los Baños, Laguna, for potential biohydrogen production. The Palawan Scientist, 15(2): 31-40.

ABSTRACT

Biohydrogen is gaining traction in energy research due to its high energy content and minimal carbon footprint. A typical method of producing biohydrogen is photofermentation using purple non-sulfur bacteria (PNSB). Exploring novel strains of PNSB and studying their versatile metabolism can aid in bioprospecting their potentially valuable by-products and applications, particularly in energy generation. This study investigated the physiological requirements of top biohydrogen-producing PNSB isolated from various Los Baños, Laguna, Philippines sites by measuring their biogas production and growth when subjected to different incubation conditions and macronutrient requirements. Results showed that the three local isolates grown anaerobically in mesophilic conditions without agitation preferred incandescent light. The high biogas yield and growth may be attributed to the light-harvesting pigments in PNSB, which are excited primarily by infrared and near-infrared wavelengths of incandescent light. Furthermore, the isolates can grow from various carbon sources, such as volatile fatty acids (malate, succinate, acetate, butyrate, and propionate) and sugars (glucose and starch). However, two of the isolates (MAY2 and PR2) did not produce biogas when supplied with acetate as a carbon source, which suggests a competing pathway that may have affected the photofermentation of the isolates. Also, the isolates prefer more complex organic sources such as yeast extract and peptone than inorganic sources such as ammonium and less complex organic sources such as urea. Finally, experiments on salt tolerance showed that 0.04% and 0.85% NaCl concentration favors biohydrogen production and growth, as exhibited by high biogas production, yield, and optical density. Results from this study can serve as a basis for future research on optimizing media composition and conditions for biohydrogen production from these isolates.

Keywords: biohydrogen, photofermentation, purple non-sulfur bacteria

INTRODUCTION

The threat of global warming and the world's energy dilemma have urged experts to find more sustainable energy sources. Along with other alternatives, biobased systems are being explored as replacements for hydrocarbon fuels. Recently, research on biohydrogen has been gaining traction, as it is an efficient energy carrier with around three times more energy than gasoline (EIA 2022) and has negligible greenhouse gas emissions (Kotay and Das 2008). Hydrogen (H_2) production can be achieved sustainably (Ahmed et al. 2021) through dark fermentation, direct and indirect biophotolysis, and photofermentation. Nevertheless, despite these various biological routes, H_2 technology is limited due to the low efficiency of the production process (Saratale et al. 2019; Tiang et al. 2020).

Photofermentation using purple non-sulfur bacteria (PNSB) is among the widely studied methods for biohydrogen production. Photofermentation can ultimately convert carbon and nitrogen sources to H_2 but is limited by various factors such as light and enzyme activity (Chandrasekhar 2015). In photofermentation, H_2 is generated as a by-product of energy generation via anoxygenic photosynthesis, where electrons from the tricarboxylic acid cycle are subsequently transferred to redox proteins embedded in the intracellular membrane, resulting in a proton gradient that powers the adenosine triphosphate cycle synthase. The nitrogenases and hydrogenases then convert the electrons and the protons to H_2. Thus, researchers are exploring ways to improve the photofermentation pathway by bio-prospecting novel species, improving strains, and identifying culture conditions that complement the growth requirements of PNSB. Among the growth requirements considered include macronutrients such as carbon and nitrogen sources, which constitute the significant biomolecules in living systems (Bonnet et al. 2020). It is already established that the amount and the type of carbon and nitrogen sources have considerable effects on the H_2 productivity of PNSB, making them primary candidates for optimization studies (Abdullah et al. 2020; Hakobyan et al. 2019). Furthermore, the H_2 photofermentative pathway requires light as an energy source, and light's spectrum and intensity have significant effects on H_2 productivity (Bosman et al. 2023; Rashid et al. 2022). Hence, the light requirement of the isolates is one essential consideration for optimization. On the other hand, there are known salt tolerant PNSBs studied mainly for their ability to utilize waste and wastewater as substrates (Chen et al. 2020; Hülsen et al. 2019). Plans for hybrid setups of wastewater treatment and photofermentation plants could benefit from salt tolerant PNSB isolates. There are limited local studies on the isolation of purple non-sulfur bacteria. One of which is by Montano et al. (2009), which isolated PNSB from rice paddies in Bulacan. Another local study is by Del Socorro et al. (2013), which isolated PNSB from rice paddies and aquatic sediments in Iligan City. These studies, however, have no emphasis on the biohydrogen production capability of the isolates and are, therefore, currently untapped in the Philippines.

This study characterized selected physiological requirements of the top biogas producers from the pool of PNSB isolates from various areas in Los Baños, Laguna. Specifically, this study investigated the effects of light (blue light-emitting diode (LED), red LED, fluorescent and incandescent), carbon (volatile fatty acids (VFAs), succinate, malate, glucose, and starch), nitrogen (ammonium, urea, glutamate, peptone, yeast extract), and NaCl concentrations (0.04%, 0.85%, 3.0%, 10.0%) on the biohydrogen production potential of the isolates. Studies suggest that the gas generated by PNSB photofermentation is composed primarily of H_2 (Craven 2019; Turon 2018; Ventura et al. 2019). Thus, biogas was measured to approximate biohydrogen production potential

METHODS

Purple Non-sulfur Bacteria Isolates

The top three biohydrogen-producing strains (MAY2, IRRI1, PR2) out of the 19 PNSB isolates obtained from water sediments in Los Banos, Laguna, Philippines (Ventura et al. 2021) were the focus of this study. MAY2 and PR2 isolates were identified under the genus *Rhodobacter*, and IRRI1 was verified to be under the genus *Rhodopseudomonas* using 16s rRNA sequencing.

Main Culture Preparation

The main cultures of these isolates were revived by multiple subsequent transfers in an acetate-yeast extract medium (AYE) (Montano et al. 2009). This medium has the following components (in g L^{-1}): K_2HPO_4, 1.0; $MgSO_4 \cdot 7H_2O$, 0.2; $CaCl_2 \cdot 2H_2O$, 0.02; $Na_2S_2O_3$, 0.10; $NaCH_3COO$, 2.2; and yeast extract, 4.0. A loopful of each culture from stock was streak-plated in Acetate Yeast Extract (AYE) agar. Cultures were incubated under incandescent light using an anaerobic set-up previously described by Maiti et al. (2013). The isolate grown from this stage was then used for the succeeding experiments.

Seed Culture Preparation

Modified Biebl and Pfennig (MBP) medium was used for the seed culture preparation. The medium contains the following components (in g·L^{-1}): $MgSO_4 \cdot 7H_2O$, 0.2; NaCl, 0.4; KH_2PO_4, 0.5; $CaCl_2 \cdot 2H_2O$, 0.05; ferric citrate, 0.005; yeast extract, 0.3; vitamin solution (nicotinic acid, 0.0002; nicotinamide, 0.0002; thiamine HCl, 0.0004; and biotin, 0.008); and 1 ml trace element solution. Trace element solution

has the following composition (in mg·L^{-1}): $ZnCl_2$, 0.07; H_3BO_3, 0.06; $MnCl_2 \cdot 4\ H_2O$, 0.1 mg; $CoCl_2 \cdot 2\ H_2O$, 0.2; $CuCl_2 \cdot 2\ H_2O$, 0.02; $NiCl_2 \cdot 6H_2O$, 0.02; $(NH_4)2MoO_4 \cdot 2\ H_2O$, 0.04 and HCl, 0.025%v/v. The pH of MBP was adjusted to pH 6.5, particularly when supplied with volatile fatty acids as the carbon source.

Before the biogas production set-up, a pre-activated seed culture was prepared. A loopful of each isolate from the AYE medium was grown in a 40 ml MBP medium supplied with 7 mm malate and 10 mm glutamate in 150 ml glass vials. The set-ups were then purged with argon gas for 3 min and crimp sealed to simulate anaerobic conditions, vortex-mixed, and incubated under incandescent light (300 nm to 1400 nm) for 3-5 days at room temperature (20-25ºC). Growth from the pre-activated cells was then harvested via centrifugation (4000 x g for 5 min) and then transferred to a fresh batch of MBP medium supplied with 7.0 mm malate and 10 mm glutamate. Their optical density (OD) was adjusted to 0.5. Four milliliters of the adjusted culture were then transferred to 36 ml of fresh MBP medium; they were purged with argon and crimp-sealed, vortex-mixed, and then incubated for three days as previously described.

Biogas Production Set-up

Four milliliters from the adjusted culture was collected and centrifuged. The pellet was then placed in 150 ml serum bottles with 40 ml fresh MBP. The setup was purged with argon gas for 3 min and then crimp-sealed. The reactor bottles were incubated without agitation under anaerobic conditions at room temperature.

Effect of Different Light Source

The biogas production set-up used for the investigation of the effect of light source utilized MBP with mixed acids - 15 mm acetate, 7.5 mm butyrate, and 10 mm propionate (approximately 2.0 g·L^{-1} in total), and 2.0 mm glutamate as nitrogen source. The set-ups were incubated under different light types: red LED (660 nm), blue LED (460 nm), incandescent light (300-1400 nm), and fluorescent light (400-700 nm). The light intensity of each light source was also measured using a lux meter (see Table 1).

Effect of Carbon and Nitrogen Sources

Using the previously mentioned biogas production setup, the capability of the three isolates to utilize different carbon sources was also investigated. Instead of mixed acids, the set-ups used individual carbon sources- malate, succinate, acetate, butyrate, propionate, glucose, and soluble starch. The concentration of each carbon source was 2.0 g L^{-1} (Basak and Das 2007; Assawamongkholsiri 2019).

Similarly, the nitrogen requirements of the isolates were also investigated using the same biogas assay setup with modification on the nitrogen source. The nitrogen sources investigated were ammonium, urea, glutamate, yeast extract, and peptone. 2.0 mM of ammonium, glutamate, and urea were used for MBP (Ventura et al. 2021), while 2.0 g L^{-1} concentration was used for peptone and yeast extract (Hakobyan et al. 2012). The setups were processed and incubated as previously described.

Effect of Salt (NaCl) Concentration

The isolates were subjected to different salt (NaCl) concentrations by adjusting the amount present in the MBP medium. The variation in salt concentrations was as follows: 0.04% (recommended amount in standard MBP medium), 0.85% (physiological saline), 3.0% (marine saline concentration), and 10% (hypersaline) (Xiao et al. 2022; Irwin 2020). The MBP medium used in the investigation of the effect of NaCl concentration was similar to the light source investigation setup. The setups were processed and incubated as previously described.

Measurement of Biogas Production and Optical Density

The cumulative biogas was measured by recording the displaced gas using a sterile syringe every 24 hours, and the cumulative readings were plotted. Biogas yield was calculated according to the method of Wu et al. (2016; equation 1).

The sampling for biogas assay in the investigation of light source ran for 20 days; while that of carbon and nitrogen sources and salt tolerance ran for ten days.

The optical density in each setup was measured on the last day of observation to approximate cell growth. Two ml of the culture broth was placed in disposable cuvettes, and optical density was measured using a Shimadzu® 1800 UV-Vis spectrophotometer set at 660 nm.

$$\text{Biogas yield ml g}^{-1} = \frac{Total\ biogas\ generated\ per\ set{-}up\ (ml)}{Volume\ of\ media\ \ (ml) \times substrate\ concentration\ (g \cdot ml^{-1})} \qquad \text{equation (1)}$$

Table 1. Light sources used in the experiment.

Light type	Brand/Model	Wattage (W)	Illuminance (lux)	Wavelength (nm)	Intensity (lux)
Incandescent	Firefly® FINS60F	60	1000	300-1400	~700
Fluorescent	Firefly® 3S32	32	1000	400-700	~3,200
Red LED	Perfin® PFLG02	10	200	660 nm	~200
Blue LED	Perfin® PFLG02	10	300	460	~200

RESULTS

Effect of Different Light Source

The isolates MAY2, PR2, and IRRI1 prefer incandescent light for biogas production. As shown in Figures 1A and 1B, the highest biogas production (in ml) of the three isolates was recorded in setups incubated under incandescent light. MAY2, IRRI1, and PR2 produced 63.6 ml (795 ml·g^{-1} substrate), 59.6 ml (745 ml·g^{-1} substrate), and 47.4 ml (592.5 ml·g^{-1} substrate) biogas, respectively. Incubation under different light sources produced minimal to almost negligible amounts of biogas. Setups incubated under red LED light did not produce biogas, while those exposed to blue LED and fluorescent light produced minimal amounts only (< 5.0 ml). Optical density was found to have the highest biomass in set-ups exposed to fluorescent and incandescent light (Table 2). As listed in Table 2, the highest OD recorded for setups under incandescent light were 1.667 and 1.574, respectively, for PR2 and MAY2, while IRRI1 gave the highest OD (1.446) for the reactors incubated under fluorescent light. The highest recorded OD for IRRI was 1.446 in fluorescent light setups, while the lowest OD values (< 0.5) were recorded in setups exposed to red LED.

Carbon and Nitrogen Requirements

The isolates were observed to variedly utilize different carbon sources (Figures 2A and 2B). For MAY2 and PR2, the highest biogas production was recorded in butyrate at 67.6 ml (845 ml·g^{-1} substrate) and 55.0 ml (687 ml·g^{-1} substrate) of biogas, respectively. On the other hand, IRRI1 supplied with acetate produced 62.7 ml of biogas (781.25 ml·g^{-1}substrate). Interestingly, PR2 and MAY2, which both belong to the genus *Rhodobacter*, did not produce biogas in acetate. These two isolates were also able to produce gas when supplied with glucose, while IRRI1 did not. All the isolates did not produce biogas when supplied with soluble starch. In terms of OD, low OD was observed in setups supplied with succinate, as shown in Table 3. The highest recorded OD was in IRRI1 supplied with butyrate at 2.091. The highest OD for MAY2 and PR2 were also recorded in setups supplied with butyrate at 1.817 and 1.419, respectively.

While there was an observed variation in the utilization of carbon sources for the three isolates, a similarity was observed in the preference for nitrogen sources (Figures 3A and 3B). The three isolates produced biogas when supplied with glutamate, yeast extract, and peptone. However, they did not yield gas in ammonium (< 0.5) and urea setups. The three isolates exhibited the highest biogas production in setups supplied with yeast extract: MAY2, PR2, and IRRI1 produced 132 ml (1650 ml·g^{-1}substrate), 107.3 ml (1446.25 ml·g^{-1} substrate), and 88.5 ml (1106.25 ml·g^{-1} substrate) of biogas, respectively. The highest OD values were also observed in yeast extract set-ups of MAY2 and PR2 (Table 4). The highest OD value for IRRI1 was recorded in set-ups supplied with peptone.

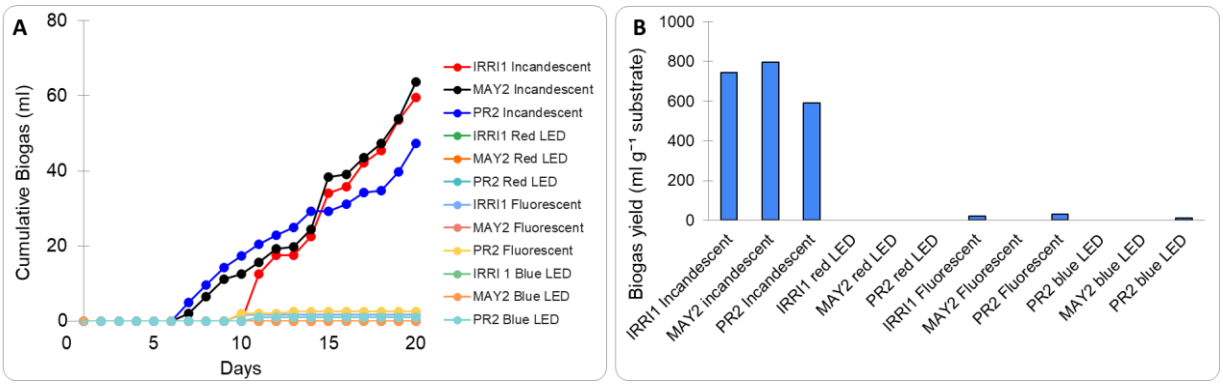

Figure 1. (A) Cumulative biogas production and (B) biogas yield of the purple-non-sulfur bacteria isolates incubated under different light conditions.

Table 2. Optical density at 660 nm (OD_{660}) measurement of purple non-sulfur bacteria (PNSB) isolates set-ups incubated under different light types.

Isolate	Light Type			
	Incandescent	Fluorescent	Red LED	Blue LED
IRRI1	1.011	1.446	0.294	1.183
MAY2	1.574	1.002	0.613	0.977
PR2	1.667	1.651	0.363	0.965

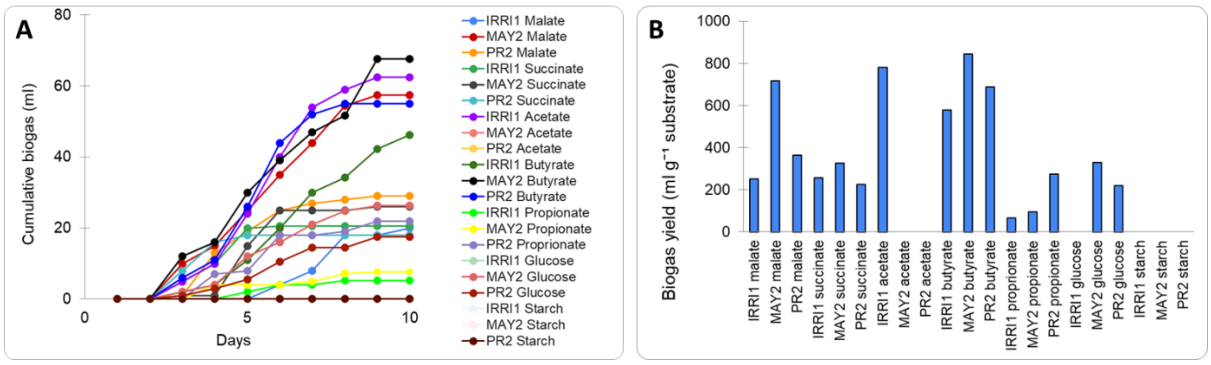

Figure 2. (A) Cumulative biogas production and (B) biogas yield of the purple non sulfur bacteria isolates under different carbon sources.

Table 3. Optical density at 660 nm (OD_{660}) measurement of the purple non-sulfur bacteria (PNSB) isolates set-ups incubated across different carbon sources.

Isolate	Carbon source						
	Malate	Succinate	Acetate	Butyrate	Propionate	Glucose	Starch
IRRI1	0.604	0.736	1.329	2.091	1.569	0.459	1.693
MAY2	1.323	0.717	1.417	1.817	0.736	1.645	1.485
PR2	0.814	0.712	1.408	1.419	0.514	1.225	1.114

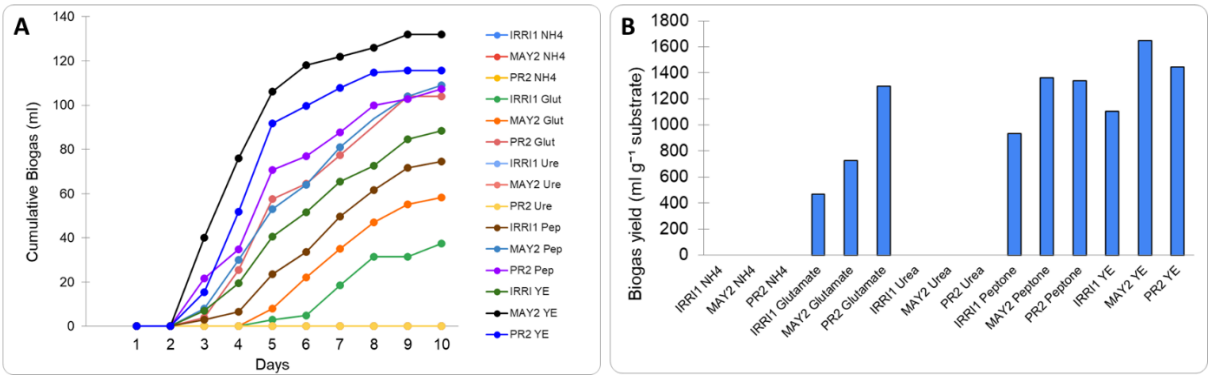

Figure 3. (A) Cumulative biogas production and (B) biogas yield of the purple non sulfur bacteria isolates under different nitrogen sources.

Table 4. Optical density at 660 nm (OD_{660}) measurement of the purple non-sulfur bacteria (PNSB) isolates set-ups incubated across different nitrogen sources.

Isolate	Nitrogen Source				
	NH_4	Glutamate	Peptone	Yeast Extract	Urea
IRRI1	0.534	0.598	0.765	0.614	0.398
MAY2	0.170	0.561	0.449	1.208	0.973
PR2	0.205	0.940	0.431	1.133	0.823

Effect of Salt (NaCl) Concentration

Thus, the salt tolerance of the isolates was also investigated. The results in Figures 4A and 4B showed that the isolates produced the highest amount of biogas in set-ups supplemented only with 0.04% NaCl. This concentration is the standard NaCl concentration of the MBP medium. MAY2, PR2, and IRRI1 produced 139.6 ml (1745 ml·g^{-1}substrate), 64 ml (800 ml·g^{-1} substrate), and 117 ml (1462.5 ml·g^{-1} substrate) of biogas, respectively. Adjusting the salt concentration to 0.85% (physiological concentration) decreased the production of biogas. Moreover, set-ups supplemented with 3.0% and 10% NaCl did not produce biogas. As shown in Table 5, cell growth is also affected by the salt concentration, as OD also decreased with the increase in NaCl. A 0.85 salt concentration exhibited the highest OD for MAY2 (1.129), followed by PR2 (0.936). IRRI1, on the other hand, produced the highest OD (0.949) at 3.0% NaCl concentration. The 10% salt concentration barely supported the cell growth of the isolates, as evidenced by an OD below 0.5.

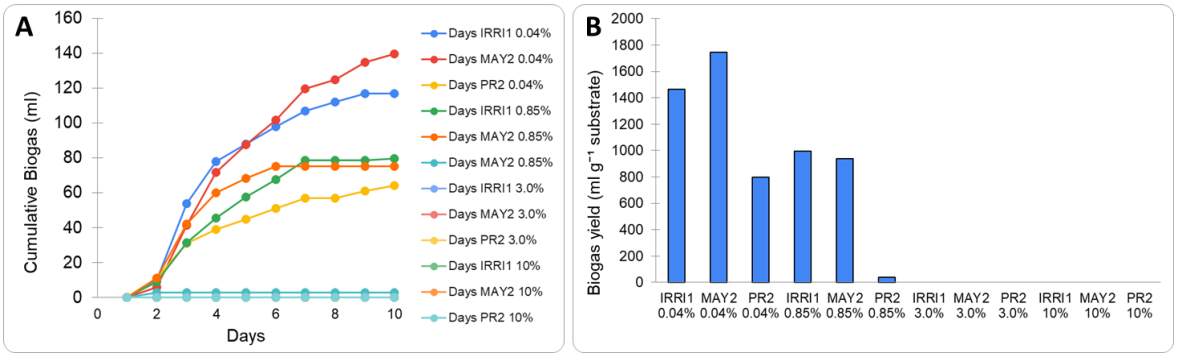

Figure 4. (A) Cumulative biogas production and (B) biogas yield of the purple non-sulfur bacteria isolates at varying salt concentrations.

Table 5. OD_{660} measurement of the purple non-sulfur bacteria isolates set-ups incubated under different salt concentration.

Isolate	Salt Concentration			
	0.04%	**0.85%**	**3.0%**	**10%**
IRRI1	0.798	0.872	0.949	0.223
MAY2	1.020	1.129	0.836	0.373
PR2	0.877	0.936	0.690	0.141

DISCUSSION

Biogas Production and Optical Density of the PNSB Isolates under Different Light Sources

Purple non-sulfur bacteria produce light-harvesting complexes (LHC) such as LH-I and LHII, which contain pigments that absorb far-red and near-infrared spectrum (Law et al. 2004). These pigments are mostly carotenoids and bacteriochlorophylls, which typically absorb light at 500 nm and above 800 nm, respectively. The absorbed light provides energy for photofermentation, which is the main pathway that generates H_2 (Deo et al. 2012). Incandescent lamps emitting an infrared spectrum (800 nm – 500 µm) were found to be the best option for H_2 production for *Rhodobacter capsulatus* (Monroy et al. 2013; Fox 2020). Furthermore, H_2 productivity is improved by the presence of both visible (400 nm – 750 nm) and infrared spectra provided by incandescent lamps (Turon et al. 2018; Halabe 2013). Therefore, the broad wavelength spectra of incandescent light provide the wavelength that complements the light absorption requirements of LHCs present in most PNSB. Observations from previous studies support the observed preference of the PNSB isolates in this study. For example, a study on *Rhodobacter capsulatus* found that replacing incandescent lamps with LED that only emit near-infrared light reduced H_2 production by 50% (Turon et al. 2018). In another study by Hu et al. (2018), the cell growth rate and H_2 production of four different species of PNSB were significantly higher when exposed to incandescent light systems compared to fluorescent. In contrast, LEDs and fluorescent are known to emit limited colored spectra (Abdel-Rahman et al., 2017), which may not provide the infrared and full visible spectra needed for optimized photofermentation, possibly limiting H_2 production. It is important to note, however, that light requirements for biohydrogen production may vary between species and can be affected by factors such as intensity and exposure time (Nath and Das 2009; Androga 2012). Additionally, the biogas production setups in the study took a more prolonged time (6 days) to produce biogas than what was usually observed (3-4 days). So, the 10-day observation period was extended to 20 days.

Based on the optical density results listed in Table 2, all the light source types used in the experiment can support the growth of the three isolates, but the cell growth of each isolate varies according to the type of source. For MAY2, incandescent light is favorable for biomass production, as evidenced by the high OD (1.574). For IRRI1, fluorescent light (1.446), while for PR2, both fluorescent and incandescent lights support high cell growth (1.667 and 1.651, respectively). Overall, many studies suggested that incandescent light best suits PNSB cultivation (Yu et al. 2021; Yu et al. 2022). For example, a study on *Rhodobacter sphaeroides* found that incandescent light generated the most biomass (5.66 g DCW L^{-1}) and protein (4.43 g L^{-1}) after 7-day cultivation compared to halogen lamp, infrared light, and variously colored LEDs. Full-spectrum incandescent light was also found to produce 3.2 times more biomass than spectral bands incandescent light (Yu et al. 2022). However, some studies focused on using other light types depending on the intended output or product. For example, Hülsen et al. (2019) utilized infrared light to selectively enrich PNSB in a non-sterile-rich medium for COD, NH_4-N, and PO_4 removal. In a study by Kuo et al. (2012), LED blue

light produced the highest cell and carotenoid concentration in cultures of *Rhodopseudomonas palustris* compared with incandescent, fluorescent, and other colors of LED lights. In a different study by Zhuo et al. (2014), red LED light was found to support higher biomass in production and COD removal of locally isolated *Rhodopseudomonas* compared with other sources of light. Moreover, the highest production of carotenoids was observed under yellow LED light. These studies suggest that blue and red light generally supports cell growth, although the optimum effect on productivity can be species-specific (Rashid et al. 2022).

These results suggest that higher biomass does not automatically mean higher biogas or H_2 production, and different light sources can support biomass growth but may not favor photofermentative biohydrogen production.

Biogas Production and Optical Density of the PNSB Isolates across Different Carbon and Nitrogen Sources.

The metabolic flexibility of PNSB allows them to assimilate different carbon sources. They are mainly studied for their capability to use volatile fatty acids as carbon sources for H_2 production. Most species of *Rhodobacter* prefer malate, succinate, butyrate, propionate, lactate, and pyruvic acid for H_2 production (Androga et al. 2012). This trend reported in the literature was also observed in the high H_2 productivity of MAY2 and PR2, both members of *Rhodobacter*. This preference can be due to the direct assimilation of the short-chain organic acids to the TCA cycle, which primarily provides electrons and protons to the photofermentation pathway. As the electrons are transferred in the pathway, a proton gradient is created, which drives the ATP synthase to generate energy, after which the protons and electrons are captured by nitrogenase to produce H_2 (Gabrielyan et al. 2015). Nonetheless, these isolates did not produce gas in acetate, which could be attributed to other competing pathways, such as the polyhydroxybutyrate (PHB) synthesis. In some *Rhodobacter* species, acetate is preferentially utilized for PHB synthesis, a pathway that competes with photofermentation for electrons obtained from the oxidation of VFAs. This relationship between the pathways puts a limit on how *Rhodobacter* can utilize acetate. *Rhodopseudomonas* members can utilize various VFAs with efficient acetate utilization (Oh et al. 2004; Touloupakis et al. 2021).

Although gas production was observed in glucose for MAY2 and PR2, the amount of gas produced was relatively lower compared to the VFA setups; starch, likewise, did not fare better. For PNSB to utilize glucose, it must be converted first to VFAs, resulting in inadvertent lowering of pH and a longer time in assimilating the substrate (Jeong et al. 2008). Starch also requires acid or enzymatic hydrolysis for it to be utilized by photosynthetic bacteria for photofermentation (Vendruscolo 2015).

The observed high biogas productivity of the isolates in setups supplied with yeast extract as a nitrogen source can be attributed to other micronutrients present in yeast extracts, such as amino acids, vitamins, minerals, and growth-stimulating compounds (Gabrielyan et al. 2015; Hay et al. 2013). These micronutrients may serve as co-enzymes and co-factors to the enzymes found in the photosynthetic electron transfer chain of the photofermentation pathway, as well as cofactors to the nitrogenases and hydrogenases. A study by (Hakobyan et al. (2012) compared the H_2 production of *Rhodobacter sphaeroides* supplied with yeast extract and glutamate as a nitrogen source. Yeast extract setups produced 6 times more H_2 than glutamate set-ups, which is attributed to the presence of growth-stimulating compounds, vitamins, and a variety of amino acids present in yeast extract. In another study by Liu et al. (2015), a novel strain of *Rhodopseudomonas* was able to grow and produce H_2 in setups supplied with peptone, beef extract, and glutamate but not in urea and ammonium. These results are similar to the obtained results of this study. The negligible production of biogas in setups supplied with ammonium can potentially be due to the inhibitory effect on ammonium ions to the nitrogenase enzyme, which either repressed the enzyme via feedback inhibition or by repression of nitrogenase-related genes (Androga et al. 2012). Similarly, urea can be broken down into carbamate and ammonium ions, possibly rendering the same effect (Alexandrova and Jorgensen 2007).

Salt (NaCl) Tolerance of the PNSB Isolates

Some PNSB members were found to withstand high salt concentrations even in seawater and hypersaline environments (Sakarika et al. 2019). Based on the results, high salt concentration halted the H_2 production of the isolates, although they were able to exhibit cell growth at 3.0% salt concentration. Many PNSB members were able to tolerate saline conditions, including species of *Rhodobacter* and *Rhodopseudomonas* (Asif et al. 2021). A study on one marine PNSB, *Rhodovulum sulfidophilum*, observed that biohydrogen production was still attained even at 3.0% salt concentration, and the optimum production is at 2.0% concentration (Cai and Wang 2012). However, for the isolates in this study, low NaCl concentration is still preferred for biogas production. These isolates were not obtained in saline or hypersaline environments and may not have the necessary adaptations for such conditions. Moreover, studies point out that increasing salinity can decrease the activity of the nitrogenase enzyme, which is the primary enzyme for photobiological hydrogen production (Severin et al. 2012).

Recommendations and Future Directions of the Study

Results from this study can serve as a baseline for future optimization experiments, as these results can narrow down the criterion and parameters of interest. Parameters such as carbon-to-nitrogen ratio and light intensity can also be explored. Furthermore, these can also be used for proper characterization and identification of the isolates.

The study relied only on crude measurement of biogas via displacement, that is why it is recommended to measure biohydrogen content and volatile fatty acid content via chromatography in future studies. Additionally, it is recommended to upscale the reaction and validate if it is comparable to the results from this study or other studies.

FUNDING

This study was funded by the National Research Council of the Philippines under the Department of Science and Technology.

ETHICAL CONSIDERATIONS

There were no animal or human subjects involved in the study.

DECLARATION OF COMPETING INTEREST

The authors declare that there are no competing interests of any authors.

ACKNOWLEDGMENTS

The authors would like to extend their gratitude to the funding agency, the National Research Council of the Philippines under the Department of Science and Technology, to our collaborating institutions, the Institute of Biological Sciences and the National Institute of Molecular Biology and Biotechnology (Biotech UPLB) and the reviewers for providing insightful comments and suggestions.

REFERENCES

Abdel-Rahman F, Okeremgbo B, Alhamadah F, Jamadar S, Anthony K and Saleh MA. 2017. Caenorhabditis elegans as a model to study the impact of exposure to light-emitting diode (LED) domestic lighting. Journal of Environmental Science and Health - Part A Toxic/Hazardous Substances and Environmental Engineering, 52(5): 433–439. https://doi.org/10.1080/10934529.2016.1270676

Abdullah MF, Jahim Md J, Abdul PM and Mahmod SS. 2020. Effect of carbon/nitrogen ratio and ferric ion on the production of biohydrogen from palm oil mill effluent (POME). Biocatalysis and Agricultural Biotechnology, 23: 101445. https://doi.org/10.1016/J.BCAB.2019.101445

Ahmed SF, Rafa N, Mofijur M, Badruddin IA, Inayat A, Ali MS, Farrok O and Khan TMY. 2021. Biohydrogen production from biomass sources: metabolic pathways and economic analysis. Frontiers in Energy Research, 9: 753878. https://doi.org/10.3389/fenrg.2021.753878

Alexandrova AN and Jorgensen WL. 2007. Why urea eliminates ammonia rather than hydrolyzes in aqueous solution. Journal of Physical Chemistry B, 111(4): 720–730. https://doi.org/10.1021/jp066478s

Androga DD, Özgür E, Eroğlu İ, Gündüz U and Yücel M. 2012. Amelioration of photofermentative hydrogen production from molasses dark fermenter effluent by zeolite-based removal of ammonium ion. International Journal of Hydrogen Energy, 37(21): 16421–16429. https://doi.org/10.1016/j.ijhydene.2012.02.177

Androga DD, Ozgur E, Eroglu I, Gunduz U and Yucel M. 2012. Photofermentative Hydrogen Production in Outdoor Conditions. In: Minic D (ed). Hydrogen Energy - Challenges and Perspectives. InTechOpen. https://doi.org/10.5772/50390

Asif A, Mohsin H and Rehman Y. 2021. Purple nonsulfur bacteria: An important versatile tool in biotechnology. Recent Advancement in Microbial Biotechnology. Agricultural and Industrial Approach, 309–337. https://doi.org/10.1016/B978-0-12-822098-6.00003-3

Assawamongkholsiri T, Reungsang A and Sittijunda S. 2019. Photo-hydrogen and lipid production from lactate, acetate, butyrate, and sugar manufacturing wastewater with an alternative nitrogen source by *Rhodobacter* sp. KKU-PS1. PeerJ 7: e6653. https://doi.org/10.7717/peerj.6653

Basak N and Das D. 2007. Microbial biohydrogen production by Rhodobacter sphaeroides OU 001 in photobioreactor. In Proceedings of the World Congress on Engineering and Computer Science, San Francisco, USA

Bonnet M, Lagier JC, Raoult D and Khelaifia S. 2020. Bacterial culture through selective and non-selective conditions: the evolution of culture media in clinical microbiology. New Microbes and New Infections, 34: 100622. https://doi.org/10.1016/J.NMNI.2019.100622

Bosman CE, Pott RWMC and Bradshaw SM. 2023. The effect of light emission spectrum on biohydrogen production by *Rhodopseudomonas palustris*. Bioprocess and Biosystems Engineering, 46: 913-919. https://doi.org/10.1007/s00449-023-02863-8

Cai J and Wang G. 2012. Hydrogen production by a marine photosynthetic bacterium, *Rhodovulum sulfidophilum* P5, isolated from a shrimp pond. International Journal of Hydrogen Energy, 37(20): 15070–15080. https://doi.org/10.1016/J.IJHYDENE.2012.07.130

Chandrasekhar K, Lee YJ and Lee DW. 2015. Biohydrogen production: strategies to improve process efficiency through microbial routes. International Journal of Molecular Sciences, 16(4): 8266–8293. https://doi.org/10.3390/ijms16048266

Chen J, Wei J, Ma C, Yang Z, Li Z, Xu Y, Wang M, Zhang H, Hu J and Chang Z. 2020. Photosynthetic bacteria-based technology is a potential alternative to meet sustainable wastewater treatment requirement? Environment International, 137: 105417. https://doi.org/10.1016/j.envint.2019.105417

Craven JD. 2019. Targeted Illumination Strategies for Hydrogen Production From Purple Non-sulfur Bacteria. University of Kentucky Institutional Repository. https://uknowledge.uky.edu/cme_etds/106/

Del Socorro MML, Mehid JB, Ladion WLB and Teves, FG. 2013. Purple Nonsulfur Bacteria (PNSB) Isolated from Aquatic Sediments and Rice Paddy in Iligan City, Philippines. J Multidisciplinary Studies, 1(1). http://dx.doi.org/10.7828/jmds.v2i1.394

Energy Information Administration (EIA). 2022. Hydrogen Explained. https://www.eia.gov/energyexplained/hydrogen/. Accessed on 30 May 2023.

Fox G. 2020. The brewing industry and the opportunities for Real-Time quality analysis using infrared spectroscopy. Applied Sciences, 10(2), 616. https://doi.org/10.3390/app10020616

Gabrielyan L, Sargsyan H and Trchounian A. 2015. Novel properties of photofermentative biohydrogen production by purple bacteria *Rhodobacter sphaeroides*: effects of protonophores and inhibitors of responsible enzymes. Microbial Cell Factories 14: 131. https://doi.org/10.1186/s12934-015-0324-3

Hakobyan L, Gabrielyan L and Trchounian A. 2012. Yeast extract as an effective nitrogen source stimulating cell growth and enhancing hydrogen photoproduction by *Rhodobacter sphaeroides* strains from mineral springs. International Journal of Hydrogen Energy, 37(8): 6519–6526. https://doi.org/10.1016/j.ijhydene.2012.01.077

Hakobyan L, Gabrielyan L and Trchounian A. 2019. Biohydrogen by *Rhodobacter sphaeroides* during photo-fermentation: Mixed vs. sole carbon sources enhance bacterial growth and H_2 production. International Journal of Hydrogen Energy, 44(2): 674–679. https://doi.org/10.1016/J.IJHYDENE.2018.11.082

Halabe UB. 2013. Non-destructive evaluation (NDE) of composites: techniques for civil structures. Sawston, Cambridge, Woodhead. 517pp. https://doi.org/10.1533/9780857093554.4.483

Hay JXW, Wu TY, Show PL and Jahim JM. 2013. Biohydrogen production through photo fermentation or dark fermentation using waste as a substrate: Overview, economics, and future prospects of hydrogen usage. Biofuels, Bioproducts and Biorefining, 7(3): 334–352. https://doi.org/10.1002/bbb.1403

Hu C, Choy S-Y and Giannis A. 2018. Evaluation of Lighting Systems, Carbon Sources, and Bacteria Cultures on Photofermentative Hydrogen Production. Applied Biochemistry and Biotechnology, 185(1): 257-269. https://doi.org/10.1007/s12010-017-2655-5

Hülsen T, Hsieh K and Batstone DJ. 2019. Saline wastewater treatment with purple phototrophic bacteria. Water Research, 160: 259–267. https://doi.org/10.1016/j.watres.2019.05.060

Irwin JA. 2020. Overview of extremophiles and their food and medical applications. In: Salwan R and Sharma V (eds). Physiological and Biotechnological Aspects of Extremophiles. Elsevier Incorporated, pp. 65-87. https://doi.org/10.1016/B978-0-12-818322-9.00006-X

Jeong TY, Cha GC, Yeom SH and Choi SS. 2008. Comparison of hydrogen production by four representative hydrogen-producing bacteria. Journal of Industrial and Engineering Chemistry, 14(3): 333–337. https://doi.org/10.1016/j.jiec.2007.09.014

Kotay SM and Das D. 2008. Biohydrogen as a renewable energy resource-Prospects and potentials. International Journal of Hydrogen Energy, 33(1): 258–263. https://doi.org/10.1016/j.ijhydene.2007.07.031

Kuo F, Chien Y and Chen C. 2012. Effects of light sources on growth and carotenoid content of photosynthetic bacteria Rhodopseudomonas palustris. Bioresource Technology, 113: 315–318. https://doi.org/10.1016/j.biortech.2012.01.087

Law CJ, Roszak AW, Southall J, Gardiner AT, Isaacs NW and Cogdell RJ. 2004. The structure and function of bacterial light-harvesting complexes. Molecular Membrane Biology, 21(3): 183–191. https://doi.org/10.1080/09687680410001697224

Liu BF, Jin YR, Cui QF, Xie GJ, Wu YN and Ren NQ. 2015. Photo-fermentation hydrogen production by *Rhodopseudomonas* sp. nov. strain A7 isolated from the sludge in a bioreactor. International Journal of Hydrogen Energy, 40(28): 8661–8668. https://doi.org/10.1016/j.ijhydene.2015.05.001

Maiti P, Haldar J, Mukherjee P and Dey R. 2013. Anaerobic culture on growth efficient bi-layered culture plate in a modified candle jar using a rapid and slow combustion system. Indian Journal of Medical Microbiology, 31(2): 173–176. https://doi.org/10.4103/0255-0857.115218

Monroy CI, Zlatev R, Stoytcheva M, González RER, Valdez B and Gochev V. 2013. Light spectra and luminosity influence on photosynthetic hydrogen production by *Rhodobacter capsulatus*. Biotechnology and Biotechnological Equipment, 27(1): 3513–3517. https://doi.org/10.5504/bbeq.2012.0130

Montano GL, Chan JS, Jarabelo RE, Pastor ABI, Dela Cruz TEE. 2009. Isolation and Characterization of Purple Non-Sulfur Bacteria from a Rice Paddy Soil in Bulacan, Philippines. Philippine Journal of Systematic Biology, 3: 57-67. http://dx.doi.org/10.3860/pjsb.v3i1.1013

Nath K and Das D. 2009. Effect of light intensity and initial pH during hydrogen production by an integrated dark and photofermentation process. International Journal of Hydrogen Energy, 34(17), 7497–7501. https://doi.org/10.1016/j.ijhydene.2008.11.065

Oh YK, Seol EH, Kim MS and Park S. 2004. Photoproduction of hydrogen from acetate by a chemoheterotrophic bacterium *Rhodopseudomonas palustris* P4. International Journal of Hydrogen Energy, 29(11): 1115–1121. https://doi.org/10.1016/j.ijhydene.2003.11.008

Rashid N, Onwusogh U and Mackey HR. 2022. Exploring the metabolic features of purple non-sulfur bacteria for waste carbon utilization and single-cell protein synthesis. Biomass Conversion and Biorefinery. https://doi.org/10.1007/s13399-022-03273-8

Sakarika M, Spanoghe J, Sui Y, Wambacq E, Grunert O, Haesaert G, Spiller M and Vlaeminck SE. 2019. Purple non-sulphur bacteria and plant production: benefits for fertilization, stress resistance and the environment. Microbial Biotechnology, 13(5): 1336–1365. https://doi.org/10.1111/1751-7915.13474

Saratale GD, Saratale RG, Banu JR and Chang JS. 2019. Biohydrogen Production From Renewable Biomass Resources. In: Pandey A, Mohan SV, Chang JS, Hallenbeck PC and Larroche C (eds). Biomass, Biofuels, Biochemicals: Biohydrogen. Elsevier, pp 247-277. https://doi.org/10.1016/B978-0-444-64203-5.00010-1

Severin I, Confurius-Guns V and Stal LJ. 2012. Effect of salinity on nitrogenase activity and composition of the active diazotrophic community in intertidal microbial mats. Archives of Microbiology, 194(6): 483–491. https://doi.org/10.1007/s00203-011-0787-5

Tiang MF, Fitri Hanipa MA, Abdul PM, Jahim JMd, Mahmod SS, Takriff MS, Lay CH, Reungsang A and Wu SY. 2020. Recent advanced biotechnological strategies to enhance photo-fermentative biohydrogen production by purple non-sulphur bacteria: An overview. In International Journal of Hydrogen Energy, 45(24): 13211-13230. https://doi.org/10.1016/j.ijhydene.2020.03.033

Touloupakis E, Poloniataki EG, Ghanotakis DF and Carlozzi P. 2021. Production of Biohydrogen and/or Poly-β-hydroxybutyrate by *Rhodopseudomona*s sp. Using Various Carbon Sources as Substrate. Applied Biochemistry and Biotechnology, 193(1): 307–318. https://doi.org/10.1007/s12010-020-03428-1

Turon V, Anxionnaz-Minvielle Z and Willison JC. 2018. Replacing incandescent lamps with an LED panel for hydrogen production by photofermentation: Visible and NIR wavelength requirements. International Journal of Hydrogen Energy, 43(16): 7784–7794. https://doi.org/10.1016/j.ijhydene.2018.03.019

Vendruscolo F. 2015. Starch: A potential substrate for biohydrogen production. International Journal of Energy Research. 39(3): 293-302 https://doi.org/10.1002/er.3224

Ventura JS, Lantican NB, Nayve Jr FRP, Ventura RLG, Roxas SM and Querubin FD. 2021. Isolation and Characterization of Photofermenting Microorganism for Biohydrogen Production. R&D Terminal Report. National Research Council of the Philippines.

Ventura RLG, Ventura JS and Oh Y-S. 2019. Photoheterotrophic Hydrogen Production of Rhodobacter sphaeroides KCTC 1434 under Alternating Ar and N 2 Headspace Gas. In Philippine Journal of Science, 148(1):63-72

Wu ATH, Lovett D, McEwan M, Cecelja F and Chen T. 2016. A spreadsheet calculator for estimating biogas production and economic measures for UK-based farm-fed anaerobic

digesters. Bioresource Technology, 220: 479–489. https://doi.org/10.1016/j.biortech.2016.08.103

Xiao T, Li Y, Hu L, Nie P, Ramaswamy HS and Yu Y. 2022. Demonstration of Escherichia coli Inactivation in Sterile Physiological Saline under High Pressure (HP) Phase Transition Conditions and Analysis of Probable Contribution of HP Metastable Positions Using Model Solutions and Apple Juice. Foods, 11(8): 1080. https://doi.org/10.3390/foods11081080

Yu S, Peng L, Xu Y, Song S, Xie G, Liu Y and Ni B. 2021. Optimizing light sources for selective growth of purple bacteria and efficient formation of value-added products. Journal of Cleaner Production, 280 (Part 2): 124493. https://doi.org/10.1016/j.jclepro.2020.124493

Yu S, Xu Y, Liang C, Lou W and Peng L. 2022. Spectral bands of incandescent lamp leading to variable productivity of purple bacteria biomass and microbial protein: Full is better than segmented. Science of the Total Environment, 823: 153736. https://doi.org/10.1016/j.scitotenv.2022.153736

Zhou Q. Zhang P and Zhang G. 2015. Biomass and pigments production in photosynthetic bacteria wastewater treatment: Effects of light sources. Bioresource Technology, 179: 505–509. https://doi.org/10.1016/j.biortech.2014.12.077

ROLE OF AUTHORS: *LAFB – data collection, data gathering, data analysis, manuscript writing, and editing; NBL – supervision, manuscript writing, and editing; RLGV – supervision, manuscript writing, and editing; JSV – conceptualization, project administration, supervision, manuscript writing, and editing.*

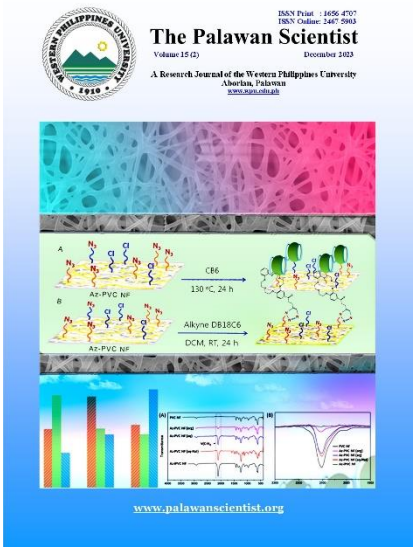

Comparative analysis of unidirectional and bidirectional electric vehicle charging stations (EVCS) optimal configuration in an IEEE 37-bus feeder system using Genetic Algorithm

Aurelio A. Balmeo, Jr.*, Rodolfo A. Aguirre, Jr., Ma. Danica G. Castillo, Edward Joseph H. Maguindayao and John Paul P. Manzano

Department of Electrical Engineering, College of Engineering and Agro-Industrial Technology, University of the Philippines Los Baños, Laguna, Philippines
**Correspondence: aabalmeo@up.edu.ph*

Received: 30 Apr. 2023 || Revised: 13 Oct. 2023 || Accepted: 27 Nov. 2023

ISSN: 1656-4707
E-ISSN: 2467-5903
Homepage: www.palawanscientist.org

How to cite:
Balmeo Jr. AA, Aguirre Jr. RA, Castillo MDG, Maguindayao EJH and Manzano JPP. 2023. Comparative analysis of unidirectional and bidirectional electric vehicle charging stations (EVCS) optimal configuration in an IEEE 37-bus feeder system using Genetic Algorithm. The Palawan Scientist, 15(2): 41-54.

ABSTRACT

Various power system problems and challenges may arise in the future due to the large scale of deployment of electric vehicles (EVs). Hence, the proper placement of EV charging stations (EVCS) effectively mitigates the impact of high EV loads connected to the grid. The research intends to explore and analyze differences between the regulation effectiveness of unidirectional and bidirectional charging technologies by utilizing different comparison evaluation indices. Moreover, considering their penetration level, this study tackles the impact analysis of EV and EVCS integration through time. Specifically, this paper aims to identify the optimal EVCS sites in an IEEE 37-bus test feeder system to minimize power loss brought by EV integration. Through MATLAB R2022b simulation and OpenDSS power flow analysis, the EVCS are optimally located near the supply bus. The findings show a direct relationship between the EV penetration level and system power loss. Due to the EV technology growth, there is an observed voltage profile degradation of up to 1.7094 p.u. The paper also highlights that although EV bidirectional charging technology (BCT) might reduce the load on the grid in the next few years of low penetration compared to unidirectional charging technology (UCT), it will give no significant difference due to the rapid increase of load connected during its high EV penetration.

Keywords: electric vehicles, MATLAB, optimization, power loss reduction, voltage profile improvement

INTRODUCTION

Today's global challenges include reducing carbon footprints and mitigating energy risks. True enough, these will eventually become huge problems if not prevented. Thus, modernizing the transportation mode to electric vehicles (EV) is eyed to cut down the usage of internal combustion engines (ICEs)—the primary contributor to problems in energy security, air pollution, and global warming (Jacobson 2017). Sofana Reka et al. (2022) proved in their study that EVs have an enormous impact on the environmental aspects of ICEs, in particular with the emissions of CO_2 gas and maintenance costs. Meanwhile, EVs make a way towards sustainability by reducing greenhouse gas (GHG) emissions and fossil fuel consumption (Bayani et al. 2022).

However, other works disagree on the drive range aspect of EVs since they are unsuitable for long-distance travel and ownership cost is currently less cost-competitive (Sofana Reka et al. 2022; Bayani et al. 2022; Danielis et al. 2018). At present, three main charging methods have been conceptualized and developed: battery exchange, conductive charging, and wireless charging (Arif et al. 2021). EV users find the battery swap station (BSS) technique a convenient option since they will only pay a monthly rental fee for quick battery swapping for their convenience. However, this technique requires users to have high payments for the BSS owner to utilize high-end batteries with a long life span and can be recharged multiple times (Gschwendtner et al. 2021; Brenna et al. 2021). Meanwhile, the wireless power transfer (WPT) differs among the three, for it can recharge the battery conveniently and safely. Even so, due to the weak inductive power and a large amount of eddy current loss, it is not advisable in the long run (Sanguesa et al. 2021). The most widely accepted charging method is the conductive charging (CC), which has a high charging efficiency through direct connection. Moreover, a vehicle-to-grid (V2G) facility can be a way to incentivize compensation, lessen losses, and prevent power grid overload (Arif et al. 2021).

Aside from the charging methods, charging modes are continuously being improved to attain charging speeds comparable to gas refueling for ICEs. Currently and generally, there are three different EV charging levels, as defined by Narasipuram and Mopidevi (2021). In the level I charging, there is an AC to DC converter integrated inside the car and charges within the current range of 15–20 A at 120 V. Research found that the ratio of driving-mile distance per charging hour is 2:1. There have been many innovations over time. Level II charging station has charging characteristics of 80 A at 240 V, which can have a 9–52-mile travel distance after an hour of charging. Meanwhile, the level III charging provides DC power and is already attached to the station. It gives 300 A current flow at 480 V, which can have 170 miles of travel in just thirty minutes of charging. However, type III is only compatible with a few EV models, leaving the rest to choose between types I and II charging. For the purpose of this research, the paper utilizes the level II type of charging. The charging level of this type is the most preferable among all the abovementioned charging types since it enables sufficiently long-distance trips and charges an EV at a reasonable length of time (Lee et al. 2020).

Conversely, the switch to vehicle modernization through EVs also creates another issue requiring plenty of accessible EV charging stations (EVCS) to recharge their batteries, as ICE vehicles need gas stations for refueling purposes. Thus, EV owners expect to have available EVCS to charge their vehicles quickly and hassle-free, maximizing the growth of this particular technology. However, this innovation might challenge government policies on how to steer the market toward full electrification in transportation despite its growing disadvantages (Sofana Reka et al. 2022).

Even though it gives users convenience, large-scale EVCS deployment negatively impacts the power grid, such as transformer overloading and power quality degradation (Zhou et al. 2017). This impact is especially true given that the distribution systems are reaching their maximum capacities. This anticipated load growth, which is dynamic and highly intermittent, would be a challenging job for the electric power sector (Gupta et al. 2020). Implementing countermeasures, such as appropriate siting of EVCS and developing coordinated unidirectional and bidirectional charging types, plays a crucial role in effectively reducing the load impacts in the distribution network (Zheng et al. 2019).

Identifying suitable EVCS location in the distribution system is fundamental for maintaining the balance between load and generation, reducing power losses, and improving system stability (Rajendran and Kumar 2022). If not arranged properly, this will significantly affect the grid, including voltage fluctuations, flickering, sag, swell, imbalances, harmonics, and notches (Narasipuram and Mopidevi 2021). Researchers have been working on this issue, exploring the optimal location of the EVCS by delving into different perspectives and patterns necessary to real-life situations. Incorporating influencing parameters such as system buses and parking availability plays a significant role in solving the optimal EVCS problem (Zeb et al. 2020). Previous studies have analyzed different power systems such as in the work of Yenchachalit et al. (2018), which utilized the IEEE 30-bus test system to determine the trend in power loss with and without an EVCS installed. Moreover, Clairan et al. (2022), an actual distribution system in Quinto, Ecuador, to determine the effect of increasing electric taxi penetration; while Janamala (2022) investigated the optimal siting of EVCS considering EV load growth in IEEE 33-, 69-, and 85-bus systems.

Various emerging optimization methods are consistently used to compare power distribution and transmission system performances. For example, the hybrid technique consisting of moth-flame optimization (MFO) algorithm and particle swarm optimization (PSO) has been done in the paper of Shaikh et al. (2023) to examine the advantages of using different numbers of bundled conductors. On the other hand, the improved MFO has been applied to AC transmission line estimations considering different test case parameters (Shaikh et al. 2022). In calculating the transmission line parameters with load modeling uncertainty, Shaikh et al. (2021) used the whale optimization algorithm (WAO).

To determine the optimal EVCS location in the power network, a balanced mayfly algorithm was

utilized to identify the best proposal for optimal allocation and sizing on a distribution system in India (Chen et al. 2021). Another literature used the Harris hawk optimization with differential evolution to solve the optimization problem in the EVCS allocation in a radial distribution network (Pal et al. 2021). The placement of EVCS in distribution systems, shunt capacitors, and distributed generators in the work of Gampa et al. (2020) used a grasshopper optimization algorithm to improve different electrical power system parameters. Lazari and Chassiakos (2023) used a genetic algorithm (GA) to minimize the overall cost of deploying the charging networks. Meanwhile, a modified GA in another study developed a mathematical program with equilibrium constraints (MPEC) in EVCS location and its discrete transport network designs (Qiao et al. 2023).

Determining possible locations not only by EVCS but also with distributed PV stations through GA was used based on chance-constrained programming (Zhang et al. 2021). Also, GA was utilized for efficient EVCS placements, taking Tunisia's urban area in North Africa as the research locale (Mehouachi et al. 2022). Nonetheless, the above-cited works of literature did not use any statistical test but instead focused on the objective function used in their respective research.

Most of these studies have only considered the unidirectional charging type, where EVs can only draw power from the grid. Bidirectional charging, as the improved type, which enables energy stored in EV batteries to discharge back to the grid, has received little attention. With the expectation that more EVs capable of bidirectional charging in the future, investigating its effect on the present distribution system is crucial in anticipating its benefits and adverse impacts (Isa et al. 2015).

Against this backdrop, this paper is primarily focused on the following aspects: (1) the investigation of the effects of new charging technologies on the power losses and voltage profiles with increasing penetration levels and its compatibility with the grid through EVCS modeling; (2) the optimal siting of EVCS to avoid negative impacts on the grid, particularly in the minimization of the additional system losses in the IEEE 37-bus test system; and (3) the comparison of the effectiveness of unidirectional and bidirectional charging types using four evaluation indices: voltage profile improvement index (VPII); real power loss reduction index (PLRI); reactive power loss reduction index (QLRI); and apparent power loss reduction index (SLRI). Cover cost-effectiveness in locating the EVCS in the test system is not covered in this paper.

The main contributions of this paper are as follows: (1) the increasing penetration levels will give theoretical trend for the simulation of EVCS optimal configuration between the two charging technologies to differentiate them in terms of power losses and total voltage deviation; (2) for the energy department of the country to pinpoint through genetic algorithm where in the bus system should the EVCS be located to obtain the minimized power losses in the grid; (3) for the policymakers to gain insight on the difference between the two charging technologies in terms of the charging behavior, and to decide on the EV charging policies that can help in grid load management.

The rest of the research paper is structured as follows: Section 2, the methods, explains the profile of the feeder, the selection method, EV specifications and modeling, the optimal model and algorithm implementation, the model construction, and indices for evaluation; Section 3, the results, includes reflecting the effect of the total integration of the new technology in increasing penetration levels, the EVCS optimal distribution configuration through genetic algorithm optimization, and charging technology comparison; and Section 4, the discussion, tackles the implications of the total integration of the advancing technology, the causes of the EVCS optimal arrangement, and the prospects, conclusions, and implications of charging implementation of unidirectional and bidirectional charging technologies.

METHODS

Institute of Electrical and Electronics Engineers (IEEE) 37-bus Test Feeder Profile and Optimal Location Selection

This research considered the medium voltage IEEE 37-bus test system. It has highly unbalanced load characteristics, differentiating it from other feeder systems. Shown in Figure 1 is the single-line diagram of the renumbered IEEE 37-bus feeder system adopted from the work of Miras et al. (2019).

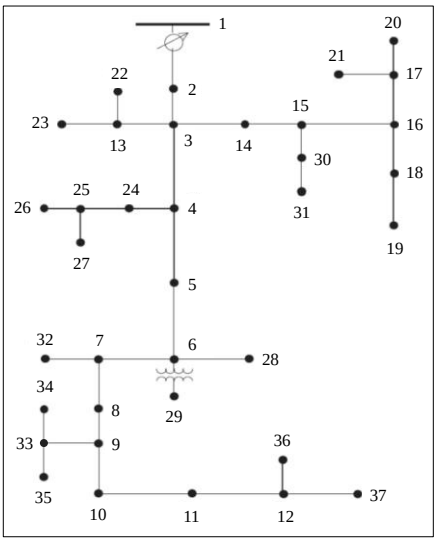

Figure 1. Single line diagram of the renumbered Institute of Electrical and Electronics Engineers (IEEE) 37-bus test system (Miras et al. 2019).

Different approaches can be used to select the optimal locations in a test bus system. In studying bus feeders, the researchers can include a constraint in geographical location employing divisions into different clusters or zones. Considering the whole network is the best option for this paper to achieve the optimal EVCS configuration. Thus, it will exclude the geographical location aspect as a constraint. Moreover, this assessment focuses on taking the feeder as a pure distribution system, minimizing power loss and improving voltage profiles.

Electric Vehicles (EV) Specifications and Modeling

Electric vehicles (EV) charging and discharging rates. The charging and discharging rates, integral to this study, were adopted from Khan et al. (2021) and are expressed in Equations 1 and 3. These mathematical models can be further elaborated expressed as Equations 2 and 4 to determine both the charging and discharging rates and the state-of-charge (SOC) trend per 15-minute interval, respectively.

$$P_{charging}(t) = [V_i(t) - 1] * Chr_{rate} \quad (1)$$

$$SOC_{new} = SOC_{old} + \frac{[V_i(t)-1]*Chr_{rate}}{(TEV)(B_{cap})} * \Delta t \quad (2)$$

$$P_{discharging}(t) = [1 - V_i(t)] * \ Dischr_{rate} \quad (3)$$

$$SOC_{new} = SOC_{old} - \frac{[1-V_i(t)]*Dischr_{rate}}{(TEV)(B_{cap})} * \Delta t \quad (4)$$

where:

$P_{charging}$	is the charging wattage (kW)
$P_{discharging}$	is the discharging wattage (kW)
V_i	is the specific voltage at bus *i* (kV)
Chr_{rate}	is the charging rate (A)
$Dischr_{rate}$	is the discharging rate (A)
B_{cap}	is the EV battery capacity (kWh)
SOC_{new}	is the updated state-of-charge
SOC_{old}	is the previous state-of-charge
Δt	is the change in time (hr)
TEV	is the total number of EVs
$E_{useable}$	is the useable battery capacity (kWh)
$\Delta SOC_{charging}$	is the SOC difference for charging
$\Delta SOC_{disharging}$	is the SOC difference for discharging

State-of-charge (SOC) based EV charging and discharging load modeling. The equation used to identify SOC-based coordinated instantaneous charging and discharging powers, which was lifted from Akil et al. (2022), is employed in this study. This relationship was formulated from the real-time charging profiles of EVs, as shown in Equation 5.

As per the piecewise model dictates, SOC-based instantaneous charging and discharging power reach their maximum when SOC is less than 73%. When SOC is at least 73% but less than 93%, there is a gradual decline in the maximum charging and discharging power. Finally, once SOC reaches 93% and above, the power remains constant.

$$P_i^n(SOC) = \begin{cases} P_i^c = P_{max} & if\ SOC < 73\% \\ P_i^c = P_{max} \cdot 3.17 \cdot -\ln(SOC) & if\ 73\% \leq SOC < 93\% \\ P_i^c = 0 & if\ SOC \geq 93\% \end{cases} \quad (5)$$

where:

P_i^n *(SOC)*	is the SOC-based instantaneous charging/discharging power (kW)
P_i^c	is the maximum instantaneous charging/discharging power (kW)
P_{max}	is the maximum charging power (kW)
SOC	is the state of charge

Electric vehicle (EV) load growth and penetration model. The penetration level is used in power engineering to anticipate the future possible impacts and real-case scenarios for power distribution networks. For instance, the Grid Integration Tech Team (GITT) and the Integrated Systems Analysis Tech Team (ISATT) of the United States have developed a real-life diagram that proposes low, medium, and high penetration scenarios from 2010 to 2050 (GITT and ISATT 2019) as shown in Figure 2.

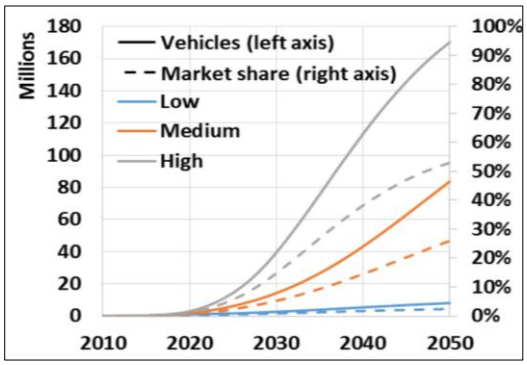

Figure 2. Electric vehicles market penetration scenarios (GITT and ISATT 2019).

In examining the differences in the optimal placement between two possible types of EVCS installations, the unidirectional charging and bidirectional charging stations serve as the two main test cases in this study. These are examined through subtest cases according to EV penetration forecast and its corresponding optimal sites: 23% in 2030, 62% in 2040, and 94% in 2050 (GITT and ISATT 2019). The three subtest cases have corresponding optimal site parameters of 11, 30, and 25, respectively (Zambrano-Perilla 2016). The base, observed in 2015, serves as a reference point when no EV penetration rate recorded (GITT and ISATT 2019).

Genetic Algorithm Implementation

Genetic algorithm (GA) is an iterative method inspired by the Darwinian theory of the survival of the fittest (Kathoch et al. 2021). It is a common optimization method used in investigating the behavior of the power system. It starts with the random generation of *n* chromosomes in a population. After the initialization, the fitness function is computed for each chromosome in the population, followed by ranking for the whole generation. Next, offspring are produced by selecting parents from the existing population using the single-point crossover. The resulting offspring will undergo mutation to produce new offspring. This cycle continues until the desired number of generations is achieved (Liu 2013).

Using MATLAB R2022b, the implementation of the GA in the study involving EVCS integration to the distribution network is shown in Figure 3. Various penetration levels at different periods were introduced, with 100 population and 100 generations as GA parameters. Single-point crossover and a 0.05 mutation rate were utilized to optimize the location of EVCS.

The integration of EVs and EVCS into the distribution network results in an increase in average real and reactive power losses (Khalkali et al. 2015). The parameters were analyzed using OpenDSS as a power flow tool.

In the first subcase, UCT considers only the charging process, while the second subcase, BCT, considers both charging and discharging setup. Moreover, half of the BCT participated in two-way charging, and the other half only utilized one-way charging (Mehrabi et al. 2020). Simulation time varies based on the number of EVCS to be located and the consideration of charging/discharging setups. Overall, more than a day of simulation runtime was spent for six subcases. The simulations were conducted on a computer with an i5-8500 CPU Processor @ 3.00 GHz, 8.00 GB installed RAM and a 64-bit operating system.

Objective Function

This paper primarily focused on the grid performance with the integration of EVCS into the network, in particular, to minimize the additional losses in the distribution network with the increase in EV penetration. Mathematically, the objective function is expressed in Equation 6:

$$F = \min \sum (S_{loss,EVCS} - S_{loss,base}) \quad (6)$$

where:

F	is the minimum additional losses (kVA)
$S_{loss,\ EVCS}$	is the total system apparent losses with EV integration (kVA)
$S_{loss,\ base}$	is the total system apparent losses without EV integration (kVA)

For the different cases, the voltage profile, system losses, and optimal sites were compared before and after the addition of EVCS. Moreover, the VPII, PLRI, QLRI, and SLRI were utilized to differentiate unidirectional and bidirectional charging.

Constraints

Maximum EVCS of each bus. It is highly recommended to have at least one charging station at each optimally selected bus to ensure the proper operation of the power distribution network. In this

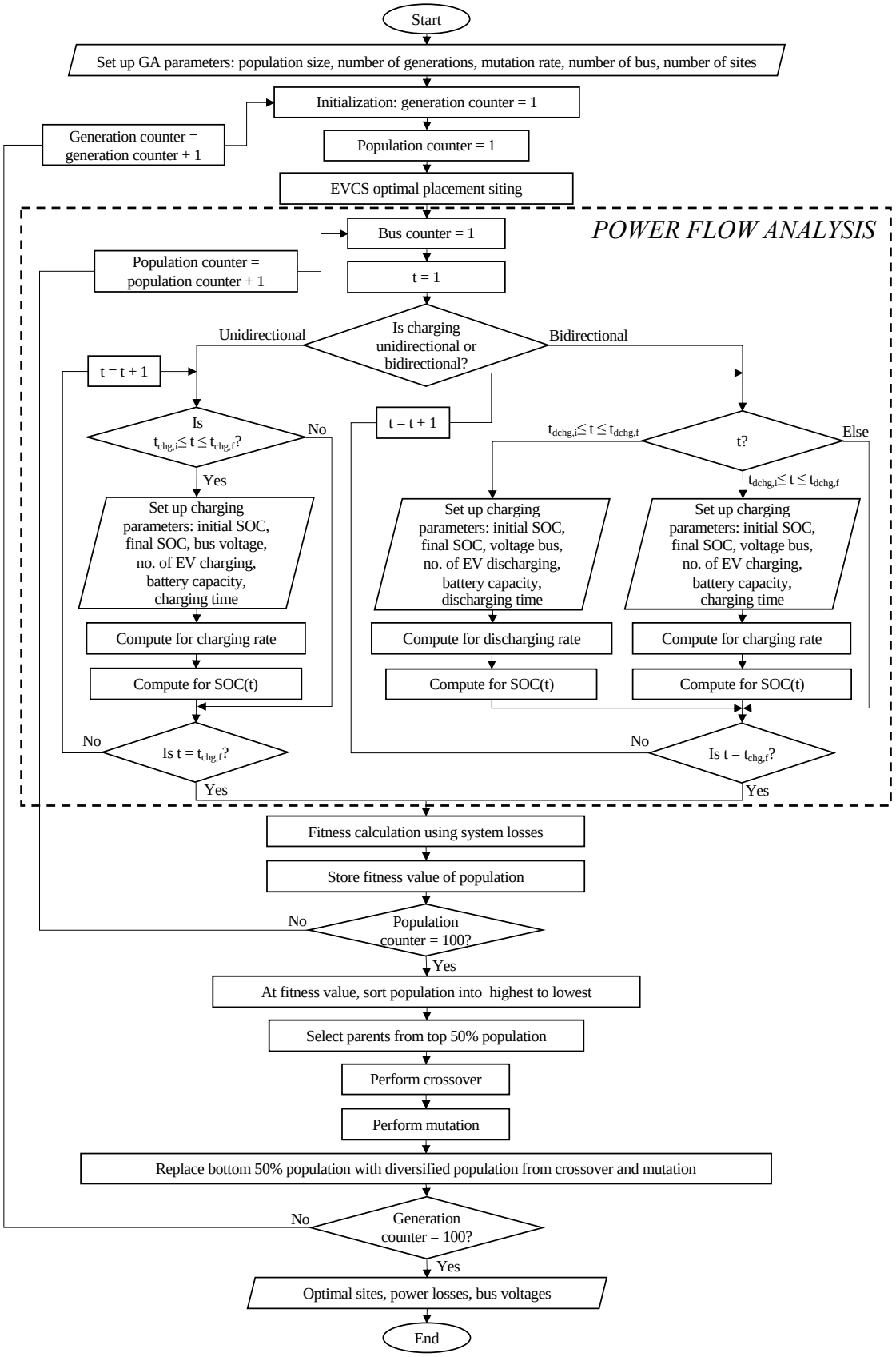

Figure 3. The process of integrating electric vehicle charging station (EVCS) unidirectional and bidirectional charging technologies into the distribution network.

scenario, the algorithm will accommodate a possible transportation route area without sacrificing the objective function (Fredriksson et al. 2019). However, for the purpose of this paper, particular buses suitable for station placements were limited to one to ensure that the EVCS infrastructure planning does not negatively affect the power grid.

Maximum capacity of EVCS. Each charging station within the specific area has limited charging ports. This limitation is attrivuted either to the connection's point inaability to serve a large load or lack of budget. According to US DOE EERE (2023), the public EVCS at the Sacramento Parking Garage, located at #939, 10th Street, Sacramento, California, has a total electric vehicle supply equipment of 27 charging ports by which the same number of EVs can charge at the same time. Taking a real-life scenario, the assumed maximum charging capacity of a standard charging station is 27 EVs. However, due to the vast penetration of EVs in the last subcase, 50 charging ports per EVCS was assumed instead, which were used as the capacity in other studies (Kunj and Pal 2020). Equation 7 shows the allowable number of charging ports in each EVCS located at bus *i*:

$$CS(i) \leq CS_{max};\ \sum_{i=1}^{N_{CS}} = N_{ch,max} \tag{7}$$

where:

CS (i) is the charging station capacity at bus *i*
CS_{max} is the maximum charging station capacity
N_{CS} is the number of charging ports
$N_{ch,\,max}$ is the maximum number of charging ports

Permissible state of charging and discharging. EV usage, mainly when it is to be charged, depends on the owner's decision. This study used the SOC range of 10% to 90% for charging, which is typical for an EV battery (Khalkali et al. 2015). Meanwhile, a range of 20% to 80% is used for discharging purposes due to the anticipation that EV owners will aim to maximize the sale of unused EV battery charge during peak electricity prices (Su et al. 2019). Thus, the limitation of the charging or discharging process as expressed in Equation 8 should be:

$$\begin{cases} SOC_n \leq SOC_{n,min}\ ; for\ charging\ only \\ SOC_{n,min} \leq SOC_n \leq SOC_{n,max};\ for\ charging/discharging \\ SOC_n \geq SOC_{n,max}; for\ discharging\ only \end{cases} \tag{8}$$

where:

SOC_n is the chosen state-of-charge (%)
$SOC_{n,\,max}$ is the maximum state-of-charge (%)
$SOC_{n,\,min}$ is the minimum state-of-charge (%)

Bus voltage tolerance. Bus voltage can vary provided that it does not exceed the range of allowable voltage values and does not have an adverse effect on the distribution network operation. To maintain the voltage range, it must be restricted between 0.9 and 1.1 per unit, as shown in Equation 9:

$$0.9\ p.u. \leq V_i \leq 1.1\ p.u. \tag{9}$$

where:

V_i is the voltage at bus *i* (p.u.)

Evaluation Indices

Voltage profile improvement index (VPII). One of the significant parameters that must be observed in the distribution network is its voltage deviation. The indicator assesses the nodal voltages concerning reference nodes and must be within acceptable limits. In evaluating the given cases, the voltage profile and system losses of different penetration scenarios were compared to the base case. Then, the optimal sites were compared after adding EVCS for charging and charging-discharging scenarios. The mathematical equations are shown in Equations 10 to 11:

$$TVD_x = \frac{1}{n}\sum_{i=1}^{n}(V_i - V_{ref}^i) \tag{10}$$

$$VPII = \frac{TVD_A + TVD_B + TVD_C}{3} \tag{11}$$

where:

TVD_x is the total voltage deviation of the system per unit at phase *x*
V_i is the bus voltage at the bus *i* per unit
V^i_{ref} is the reference bus voltage
n is the total number of buses
VPII is the voltage profile improvement index

System power loss reduction indices. The system losses and their respective reduction indices were used to compare the two charging technologies and their corresponding optimal sites. The mathematical equations of the indices are given in Equations 12 to 14:

$$PLRI = \frac{P_{withUCT} - P_{withBCT}}{P_{with\ UCT}} x\ 100 \quad (12)$$

where:

PLRI is the real power loss reduction index due to EV integration (%)
$P_{withUCT}$ is the real power losses with EVCS UCT (kW)
$P_{withBCT}$ is the real power losses with EVCS BCT (kW)

The second evaluation indicator in Equation 12 assesses whether the EVCS charging technology enhances or minimizes power losses. In particular, it also indicates the loss reduction trend due to the bidirectional participation of the EVCS in the grid relative to the unidirectional charging process.

$$QLRI = \frac{Q_{withUCT} - Q_{withBCT}}{Q_{withUCT}} x\ 100 \quad (13)$$

where:

QLRI is the reactive power loss reduction index due to EV integration (%)
$Q_{withUCT}$ is the reactive power losses with EVCS UCT (kVAR)
$Q_{withBCT}$ is the reactive power losses with EVCS BCT (kVAR)

One of the indicators of a stable grid is when the reactive power losses do not exceed a threshold value (Chen et al. 2021). The QLRI in Equation 13 aims to determine if reactive power loss is within the definite threshold value to maintain the power grid stability. Thus, the QLRI has been included in the study.

Shown in Equation 14 is the SLRI, which is one of the important parameters to assess whether the distribution network has improved. When it goes beyond the threshold value, the distribution network is unstable.

$$SLRI = \frac{S_{withUCT} - S_{withBCT}}{S_{withUCT}} x\ 100 \quad (14)$$

where:

SLRI is the apparent power loss reduction index due to EV integration (%)
$S_{withUCT}$ is the apparent power losses with EVCS UCT (kVA)
$S_{withBCT}$ is the apparent power losses with EVCS BCT (kVA)

RESULTS

Total Integration of EVs and EVCS Considering Increasing Penetration Levels

The graph in Figure 4 illustrates the power losses at each penetration stage for their respective technologies. The anticipated apparent power loss of EV integration in the year 2050 is extremely high at 465.2930 kVA for both charging technologies, as its penetration level is expected to reach 94%. Meanwhile, the year 2040 in the graph has a relatively lower penetration than the year 2050 at 62%, which gives apparent power losses of 364.5683 kVA for both unidirectional and bidirectional modes. In the year 2030 EV integration, forecasted losses are at 96.3131 kVA for unidirectional charging and 92.0304 kVA for bidirectional charging, given a 23% penetration rate. All these values are relatively higher than the base power loss of 82.5268 kVA in the year 2015 when there was no EV integration.

In Figures 5 and 6, the plots of UCT and BCT per-unit bus voltage for phase A of the system depict a gradual decrease in bus voltages with increasing EV penetration levels, regardless of the charging technology. On the other hand, in terms of VPII, as shown in Table 1, there is an increase in the indices concerning the considered years. Moreover, in the years 2040 and 2050, similar results were observed for both unidirectional and bidirectional charging. Meanwhile, the UCT in the year 2030 has a higher VPII than the BCT.

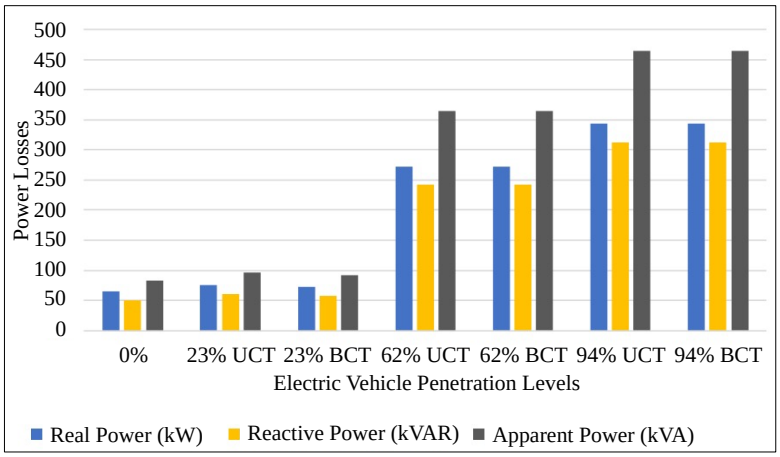

Figure 4. The graph of power losses vs. EV penetration levels. UCT- unidirectional charging technology; BCT- bidirectional charging technology.

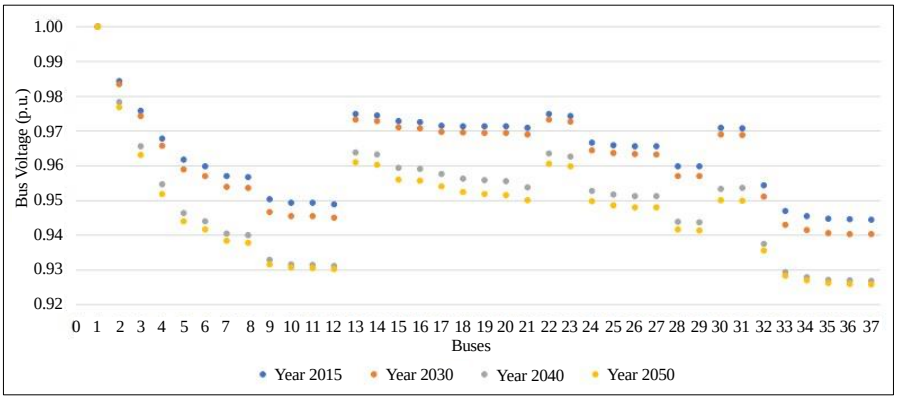

Figure 5. The per-unit bus voltage profile in different test case scenarios in unidirectional charging technology setup for phase A.

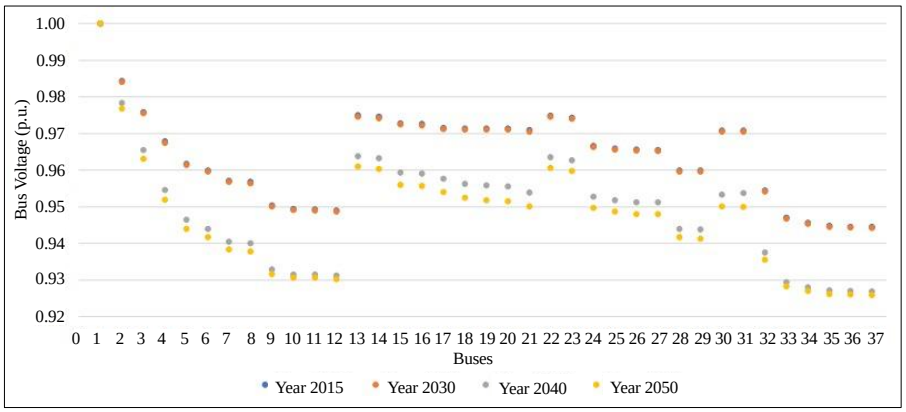

Figure 6. The per-unit bus voltage profile in different test case scenarios in bidirectional charging technology setup for phase A.

Table 1. The voltage profile improvement index (VPII) between undirectional charging technology (UCT) and bidirectional charging technology (BCT) for different penetration levels.

Year	Subcase (penetration level)	VPII (p.u.)	
		UCT	BCT
2015	0%	1.1139	
2030	23%	1.2020	1.1249
2040	62%	1.6260	1.6259
2050	94%	1.7094	1.7094

Electric Vehicle Charging Station (EVCS) Optimal siting

Optimal placement assesses the possible site combinations to attain the objective function. To facilitate a comparison of optimal locations for each subcase based on the penetration level, Table 2 presents a summary of the optimization results. The same buses were identified in the subcases of both power charging technology for every penetration level. Lastly, Figure 7 illustrates that the resulting optimal sites are concentrated in specific locations.

Table 2. Optimal electric vehicle charging station sites at different penetration levels.

Main Cases	Subcase (penetration level)	Year	Optimal Sites
Unidirectional	23%	2030	2, 3, 4, 5, 13, 14, 15, 22, 23, 30
Bidirectional			2, 3, 4, 5, 13, 14, 15, 22, 23, 30
Unidirectional	62%	2040	2, 3, 4, 5, 6, 7, 8, 9, 10, 13, 14, 15, 16, 17, 18, 19, 20, 21, 22, 23, 24, 25, 26, 27, 28, 29, 30, 31, 32, 33
Bidirectional			2, 3, 4, 5, 6, 7, 8, 9, 10, 13, 14, 15, 16, 17, 18, 19, 20, 21, 22, 23, 24, 25, 26, 27, 28, 29, 30, 31, 32, 33
Unidirectional	94%	2050	2, 3, 4, 5, 6, 7, 8, 13, 14, 15, 16, 17, 18, 19, 21, 22, 23, 24, 25, 26, 27, 28, 30, 31, 32
Bidirectional			2, 3, 4, 5, 6, 7, 8, 13, 14, 15, 16, 17, 18, 19, 21, 22, 23, 24, 25, 26, 27, 28, 30, 31, 32

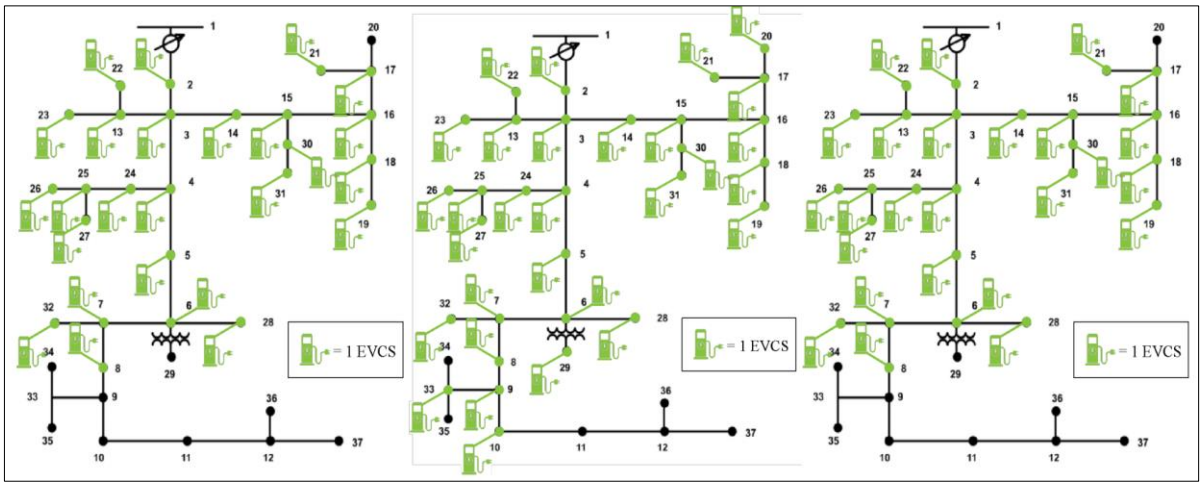

(a) **(b)** **(c)**

Figure 7. The electric vehicle charging stations (EVCS) installation at (a) 23%, (b) 62%, and (c) 94% EV penetration rates.

Comparison of Index Values Between Charging Technologies

The VPII of all buses connected to phase A in the test system was calculated with the year 2015 as the reference. Figure 8 reveals that there is almost no difference in VPII for the bidirectional case of the year 2030 compared to the base case. On the other hand, a slight distortion is apparent in the graph of unidirectional charging.

Using the results of unidirectional charging as reference values for the bidirectional case, system power losses were analyzed to compare the characteristics of the charging technologies. Table 3 shows that only the year 2030 has non-zero index values.

Table 3. Real, reactive, and apparent power loss reduction indices. PLRI - real power loss reduction index; QLRI- reactive power loss reduction index; SLRI-apparent power loss reduction index.

Subcase (penetration level)	Year	Evaluation Indicators of Comparison		
		PLRI	QLRI	SLRI
23%	2030	4.142878856	4.916659909	4.44664329
62%	2040	0	0	0
94%	2050	0	0	0

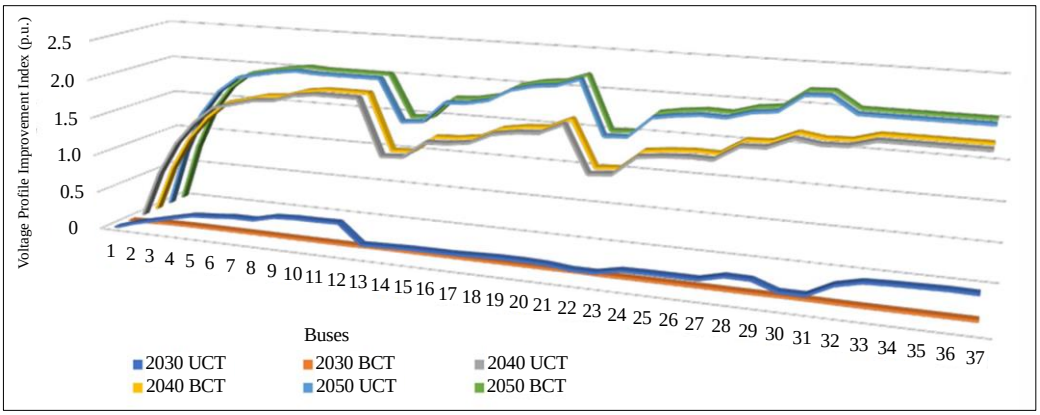

Figure 8. Phase A voltage profile improvement index (VPII) of the entire network. UCT- undirectional charging technology; BCT- bidirectional charging technology

DISCUSSION

Total Integration of EVs and EVCS Considering Increasing Penetration Levels

As observed in the graph presented in Figure 4, there exists a direct relationship between the penetration of EVs and the apparent power loss. Higher integration of EVs results in a higher apparent power loss, regardless of the charging technology employed in the system. The anticipated transition from ICE vehicles to EVs is expected to contribute to higher apparent losses in the power grid. Variations in the penetration level have caused changes in the power loss, the number of optimal sites, and the capacity of the EVCS. It can be concluded that there is a significant increase in real, reactive, and apparent power losses. Thus, the higher anticipation of EV loads due to the increasing penetration level through time is expected to be caused by the advancements in the transportation sector. Without proper intervention, additional EV loads could alter the normal grid operations.

On the other hand, the varying penetration levels in this study assessed the impacts of the EV integration. The dramatic increase in penetration rate has a negative effect on the voltage profile of the power grid. As the injected EV load increases, the bus voltages deviate from the ideal value. With the expected technological advancement in EVs, there is an anticipated voltage profile deterioration by as much as 1.7094 p.u. Based on the trend analysis of Table 1 values, the voltage profile is deteriorating in the subsequent years.

Electric Vehicle Charging Station (EVCS) optimal siting

Overall, there is a commonality among the respective penetration levels where the resulting optimal sites in the test system cluster in the nodes near the supply bus. Indeed, these results are consistent with recent works. One of these studies has presented that connecting an EVCS at any bus in the distribution network increases the active power loss due to the resistance of the branches from the slack bus to the considered node (Bilal et al. 2021). Thus, to reduce the resulting power loss, the EVCS should be located closer to the upstream network near the supply (Hadian et al. 2020).

The observation shows similar results when the number of optimal sites increases in the distribution network. Another factor contributing to this trend is the bidirectional participation of EV owners. According to Mehrabi et al. (2020), the willingness of the drivers to participate in the bidirectional charging is 50%. This means the ratio of charging and discharging in the bidirectional technology is 2:1, indicating that for every two charging vehicles, only one can discharge. With this, the research suggests that all EVs still need to be charged before this half undergoes discharging energy into the power system. Hence, UCT and BCT had the same optimal sites since they usually acted as a load.

Comparison of Index Values Between Charging Technologies

After identifying the optimal sites where minimum power losses are observed, there is a noticeable difference between the two power charging directions. During the years with low penetration, there is less power loss in UCT than in BCT. However, during higher EV penetration beyond the year 2040, the distribution network experiences more apparent power losses, considering that BCT has become the norm in society. Correspondingly, power losses increase as the EV penetration rate increases from the base case year 2015 when there is no EV integration.

The BCT in the year 2030 exhibits a more improved power loss relative to the UCT of the same year since it deviates mainly from the base case. On the other hand, the EV load integrated into the system

contributes to the fluctuations in the UCT in 2030, as observed in Figure 8. Meanwhile, power losses in both charging technologies are the same for the years 2040 and 2050, where EV penetration is higher than in the former cases. The discharging scenario in BCT positively affects the distribution network by providing additional power to the system. Nevertheless, due to the high EV loads, both the UCT and BCT negatively affect the grid, which resulted in high VPII values.

Table 3 presents the system loss indices for the BCT subcases relative to their corresponding UCT counterparts. For 2030, the power loss index values of 4.14%, 4.92%, and 4.45% are determined for PLRI, QLRI, and SLRI, respectively. Since there is a positive value in PLRI at 4.14%, there is a minimization and loss reduction trend this year brought by utilizing BCT over the UCT case. Moreover, the 4.92% QLRI implies a more stable power grid from BCT application in the said year. Lastly, the 4.45% SLRI shows an overall improvement in the system due to the reduction in apparent power losses from using bidirectional charging.

Meanwhile, the three evaluation indices have zero values at higher penetration rates of 62% and 94%. These results signify that the system losses from using BCT and UCT are the same, and there is no advantage in using the former over the latter.

The results suggest that bidirectional charging can provide opportunities to improve the distribution system if more EV owners utilize it. A 50% EV bidirectional participation is insufficient to make the distribution system better since the result shows no difference compared to unidirectional charging at high EV penetration. Hence, further studies can examine the possibility of incentivizing participation in bidirectional charging through tariffs and tax credits. The distribution system operator can do proper grid interventions, such as replacing the lines with lower resistance and utilizing power loss compensator equipment in anticipation of higher EV loads in the future. Moreover, another path of future research on differentiating the two charging technologies is studying the cost-effectiveness, battery efficiency and deterioration, and grid communication, particularly with traffic demand management of the mixed flow of two charging technologies.

FUNDING

The authors declare that this research did not receive any specific grant from funding agencies in the public, commercial, or not-for-profit sectors.

ETHICAL CONSIDERATIONS

This study is guided by ethical and legal principles, responsibly ensuring that this is free of research misconduct and presents the results accurately. Moreover, the authors of the references were duly acknowledged and cited with proper citations.

DECLARATION OF COMPETING INTEREST

The authors declare that there are no competing interests among any authors.

ACKNOWLEDGMENTS

The authors acknowledge the support of the University of the Philippines Los Baños and the valuable comments of the external reviewers who evaluated this paper.

REFERENCES

Akil M, Dokur E and Bayindir R. 2022. Modeling and evaluation of SOC-based coordinated EV charging for power management in a distribution system. Turkish Journal of Electrical Engineering and Computer Sciences, 30(3): 678-694. https://doi.org/10.55730/1300-0632.3805

Arif SM, Lie TT, Seet BC, Ayyadi S and Jensen K. 2021. Review of electric vehicle technologies, charging methods, standards and optimization techniques. Electronics, 10(16):1910. https://doi.org/10.3390/electronics10161910

Bayani R, Soofi AF, Waseem M and Manshadi SD. 2022. Impact of transportation electrification on the electricity grid—a review. Vehicles, 4(4): 1042-1079. https://doi.org/10.3390/vehicles4040056

Bilal M, Rizwan M, Alsaidan I and Almasoudi FM. 2021. AI-based approach for optimal placement of EVCS and DG with reliability analysis. Institute of Electrical and Electronics Engineers, 9: 154204–154224. https://doi.org/10.1109/ACCESS.2021.3125135

Brenna M, Foiadelli F, Zaninelli D, Graditi G and Di Somma M. 2021. The integration of electric vehicles in smart distribution grids with other distributed resources. In: Graditi G and Di Somma M (eds). Distributed Energy Resources in Local Integrated Energy Systems. Elsevier, Amsterdam, Netherlands, pp. 315–345. https://doi.org/10.1016/B978-0-12-823899-8.00006-6

Chen L, Xu C, Song H and Jermsittiparsert K. 2021. Optimal sizing and sitting of EVCS in the distribution system using metaheuristics: a case study. Energy Reports, 7: 208–217. https://doi.org/10.1016/J.EGYR.2020.12.032

Clairan JM, Gonzales-Rodriguez M, Kumar R, Vyas S and Escriva-Escriva G. 2022. Optimal siting and sizing of electric taxi charging stations considering transportation and power system requirements. Energy, 256: 124572. https://doi.org/10.1016/j.energy.2022.124572

Danielis R, Giansoldati M and Rotaris L. 2018. A probabilistic total cost of ownership model to evaluate the current and future prospects of electric cars uptake in Italy. Energy Policy, 119: 268-281. https://doi.org/10.1016/j.enpol.2018.04.024

Fredriksson H, Dahl M and Holmgren J. 2019. Optimal placement of charging stations for electric vehicles in large-scale transportation networks. Procedia Computer Science, 160: 77–84. https://doi.org/10.1016/J.PROCS.2019.09.446

GITT and ISATT (Grid Integration Tech Team and Integrated Systems Analysis Tech Team). 2019. Summary report on EVs at scale and the U.S. electric power system. U.S. Department of Energy. 21pp. https://www.energy.gov/eere/vehicles/articles/summary

-report-evs-scale-and-us-electric-power-system-2019. Accessed on 29 April 2023.

Gampa SR, Jasthi K, Goli P, Das D and Bansal RC. 2020. Grasshopper optimization algorithm based two stages fuzzy multi-objective approach for optimum sizing and placement of distributed generations, shunt capacitors and electric vehicle charging stations. Journal of Energy Storage, 27: 101117. https://doi.org/10.1016/J.EST.2019.101117

Gschwendtner C, Sinsel SR and Stepan A. 2021. Vehicle-to-X (V2X) implementation: An overview of predominate trial configurations and technical, social and regulatory challenges. Renewable and Sustainable Energy Reviews, 145: 110977. https://doi.org/10.1016/j.rser.2021.110977

Gupta K, Achathuparambil R, Narayanankutty, Sundaramoorthy K and Sankar A. 2020. Optimal location identification for aggregated charging of electric vehicles in solar photovoltaic powered microgrids with reduced distribution losses. Energy Sources, Part A: Recovery, Utilization, and Environmental Effects. https://doi.org/10.1080/15567036.2020.1745335

Hadian E, Akbari H, Farzinfar M and Saeed S. 2020. Optimal allocation of electric vehicle charging stations with adopted smart charging/discharging schedule. Institute of Electrical and Electronics Engineers, 8: 196908–196919. https://doi.org/10.1109/ACCESS.2020.3033662

Isa NBM, Wei TC and Yatim AHM. 2015. Smart grid technology: communications, power electronics and control system. 2015 International Conference on Sustainable Energy Engineering and Application (ICSEEA), Bandung, Indonesia, pp. 10-14. https://doi.org/10.1109/ICSEEA.2015.7380737

Jacobson MZ. 2017. Roadmaps to transition countries to 100% clean, renewable energy for all purposes to curtail global warming, air pollution, and energy risk. Earth's Future, 5(10): 948–952. https://doi.org/10.1002/2017EF000672

Janamala V. 2022. Optimal siting of capacitors in distribution grids considering electric vehicle load growth using improved flower pollination algorithm. Serbian Journal of Electrical Engineering, 19(3): 329-349. https://doi.org/10.2298/SJEE2203329J

Katoch S, Chauhan SS and Kumar V. 2021. A review on genetic algorithm: past, present, and future. Multimedia Tools and Applications, 80(5): 8091–8126. https://doi.org/10.1007/s11042-020-10139-6

Khalkali K, Abapour S, Moghaddas-Tafreshi SM and Abapour M. 2015. Application of data envelopment analysis theorem in plug-in hybrid electric vehicle charging station planning. Institute of Engineering and Technology (IET) Generation, Transmission and Distribution, 9(7): 666–676. https://doi.org/10.1049/IET-GTD.2014.0554

Khan R, Mehmood KK, Bukhari SBA, Imran K, Wadood A, Rhee SB and Park S. 2021. An optimization-based reliability enhancement scheme for active distribution systems utilizing electric vehicles. Institute of Electrical and Electronics Engineers, 9: 157247–157258. https://doi.org/10.1109/ACCESS.2021.3127802

Kunj T and Pal K. 2020. Optimal location planning of EV charging station in existing distribution network with stability condition. 2020 7th International Conference on Signal Processing and Integrated Networks (SPIN), Noida, India, pp. 1060-1065. https://doi.org/10.1109/SPIN48934.2020.9071396

Lazari V and Chassiakos A. 2023. Multi-objective optimization of electric vehicle charging station deployment using genetic algorithms. Applied Sciences. 13(8): 4867. https://doi.org/10.3390/app13084867

Lee JH, Chakraborty D, Hardman SJ and Tal G. 2020. Exploring electric vehicle charging patterns: Mixed usage of charging infrastructure. Transportation Research Part D: Transport and Environment, 79: 102249. https://doi.org/10.1016/J.TRD.2020.102249

Liu Z, Wen F and Ledwich G. 2013. Optimal planning of electric-vehicle charging stations in distribution systems. Institute of Electrical and Electronics Engineers Transactions on Power Delivery, 28(1): 102–110. https://doi.org/10.1109/TPWRD.2012.2223489

Mehouachi I, Trojette M and Grayaa K. 2022. Optimal placement of electric vehicle charging infrastructure: study case of an urban area of Tunisia. Institute of Electrical and Electronics Engineers, 8: 189-194. https://doi.org/10.1109/CoDIT55151.2022.9803893.

Mehrabi A, Nunna HSVSK, Dadlani A, Moon S and Kim K. 2020. Decentralized greedy-based algorithm for smart energy management in plug-in electric vehicle energy distribution systems. Institute of Electrical and Electronics Engineers, 8: 75666–75681. https://doi.org/10.1109/ACCESS.2020.2987970

Miras AJJ, Manzano JPP, Aguirre RA and Aquino KMV. 2019. Sizing and siting of a concentrating solar power plant in an unbalanced radial distribution system. 2019 Institute of Electrical and Electronics Engineers, Power and Energy Society, Asia-Pacific Power and Energy Engineering Conference, Macao, China, pp. 1-6. https://doi.org/10.1109/APPEEC45492.2019.8994631

Narasipuram RP and Mopidevi S. 2021. A technological overview & design considerations for developing electric vehicle charging stations. Journal of Energy Storage, 43:103225. https://doi.org/10.1016/j.est.2021.103225

Pal A, Bhattacharya A and Chakraborty AK. 2021. Allocation of electric vehicle charging station considering uncertainties. Sustainable Energy, Grids and Networks, 25: 100422. https://doi.org/10.1016/J.SEGAN.2020.100422

Qiao D, Wang G and Xu M. 2023. Mathematical program with equilibrium constraints approach with genetic algorithm for joint optimization of charging station location and discrete transport network design. The International Journal of Transportation Research: Transportation Letters. https://doi.org/10.1080/19427867.2023.2237740

Rajendran A and Hari Kumar R. 2022. Optimal placement of electric vehicle charging stations in utility grid - a case study of Kerala state highway network. PESGRE 2022 – Institute of Electrical and Electronics Engineering International Conference on Power Electronics, Smart Grid, and Renewable Energy, Trivandrum, India, pp. 1-6. https://doi.org/10.1109/PESGRE52268.2022.9715934.

Sanguesa JA, Torres-Sanz V, Garrido P, Martinez FJ and Marquez-Barja JM. 2021. A review on electric vehicles: technologies and challenges. Smart Cities, 4(1): 372–404. https://doi.org/10.3390/smartcities4010022

Shaikh MS, Hua C, Hassan M, Raj S, Jatoi MA and Ansari MM. 2021. Optimal parameter estimation of overhead transmission line considering different bundle conductors with the uncertainty of load modeling. Optimal Control Applications and Methods, 43(3): 652-666. https://doi.org/10.1002/oca.2772

Shaikh MS, Raj S, Babu R, Kumar S and Sagrolikar K. 2023. A hybrid moth–flame algorithm with particle swarm optimization with application in power transmission and distribution. Decision Analytics, 6: 100182. https://doi.org/10.1016/j.dajour.2023.100182

Shaikh MS, Raj S, Ikram M and Khan W. 2022. Parameters estimation of AC transmission line by an improved moth flame optimization method. Journal of Electrical Systems and Information Technology, 9: 25. https://doi.org/10.1186/s43067-022-00066-x

Sofana Reka S, Venugopal P, V R, Haes Alhelou H, Al-Hinai A and Pierluigi S. 2022. Analysis of electric vehicles with an economic perspective for the future electric market. Future Internet, 14(6): 172. https://doi.org/10.3390/fi14060172

Su J, Lin M, Wang S, Li J, Coffie-Ken J and Xie F. 2019. An equivalent circuit model analysis for the lithium-ion

battery pack in pure electric vehicles. Measurement and Control, 52(3-4): 193-201. https://doi.org/10.1177/0020294019827338

US DOE EERE (United States Department of Energy Energy Efficiency and Renewable Energy). 2023. The electric vehicle charging stations locations. Version 2023. https://afdc.energy.gov/fuels/electricity_locations.html#/find/nearest?fuel=ELEC. Accessed on 29 April 2023.

Yenchamchalit K, Kongjeen Y, Bhumkittipich K and Mithulnanthan N. 2018. Optimal sizing and location of the charging station for plug-in electric vehicles using the particle swarm optimization technique. 2018 International Electrical Engineering Congress, Krabi, Thailand, pp. 1-4. https://doi.org/10.1109/IEECON.2018.8712336

Zambrano-Perilla S, Ramos G and Rodriguez DFC. 2016. Modeling and impacts of plug-in electric vehicles in residential distribution systems with coordinated charging schemes. International Review on Modelling and Simulations (IREMOS), 9(4): 227–237. https://doi.org/10.15866/IREMOS.V9I4.9198

Zeb MZ, Imran K, Khattak A, Janjua, AK, Pal A, Nadeem M, Zhang J and Khan S. 2020. Optimal placement of electric vehicle charging stations in the active distribution network. Institute of Electrical and Electronics Engineers, 8: 68124–68134. https://doi.org/10.1109/ACCESS.2020.2984127

Zhang X, Xu Y, Lu S, Lu C and Guo Y. 2021. Joint planning of distributed PV stations and EV charging stations in the distribution systems based on chance-constrained programming. Institute of Electrical and Electronics Engineers, 9: 6756- 6768. https://doi.org/10.1109/ACCESS.2021.3049568

Zheng Y, Niu S, Shang Y, Shao Z and Jian L. 2019. Integrating plug-in electric vehicles into power grids: a comprehensive review on power interaction mode, scheduling methodology and mathematical foundation. Renewable and Sustainable Energy Reviews, 112: 424–439. https://doi.org/10.1016/J.RSER.2019.05.059

Zhou X, Zou L, Ma Y and Gao Z. 2017. Research on impacts of the electric vehicles charging and discharging on power grid. Proceedings of the 29th Chinese Control and Decision Conference, Chongqing, China, pp. 1398–1402. https://doi.org/10.1109/CCDC.2017.7978736

ROLE OF AUTHORS: *AABJ - conceptualized the study, designed, and implemented the case studies, analyzed the data, wrote the paper; RAAJ - conceptualized and supervised the study, analyzed the data, reviewed, and edited the paper; MDGC - reviewed and edited the paper; EJHM - reviewed and edited the paper; JPPM - reviewed and edited the paper.*

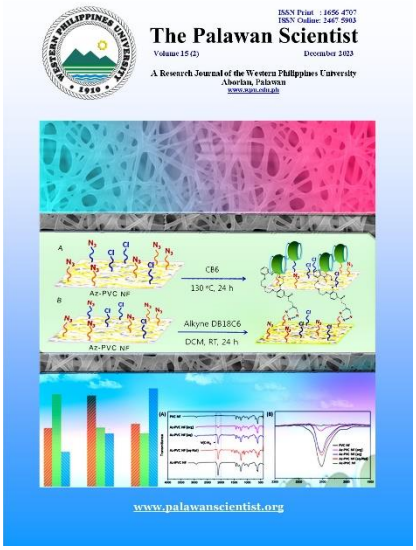

Numerical modeling of the drying behavior of Adlai (*Coix lacryma-jobi* L.) grain

Alvin M. Ante[1*], Arnold R. Elepaño[2], Kevin F. Yaptenco[2] and Delfin C. Suministrado[3]

[1]*Department of Agricultural and Biosystems Engineering, College of Engineering, Dr. Emilio B. Espinosa Sr. Memorial State College of Agriculture and Technology, Mandaon, Masbate, Philippines*
[2]*Agricultural, Food and Bio-process Engineering Division, Institute of Agricultural and Biosystems Engineering, College of Engineering and Agro-Industrial Technology, University of the Philippines Los Baños, Laguna, Philippines*
[3]*Agribiosystems Machinery and Power Engineering Division, Institute of Agricultural and Biosystems Engineering, College of Engineering and Agro-Industrial Technology, University of the Philippines Los Baños, Laguna, Philippines*
**Correspondence: amante@up.edu.ph or antealvin@gmail.com*

Received: 31 May 2023 || Revised: 17 Oct. 2023 || Accepted: 28 Nov. 2023

ISSN: 1656-4707
E-ISSN: 2467-5903
Homepage: www.palawanscientist.org

How to cite:
Ante AM, Elepaño AR, Yaptenco KF and Suministrado DC. 2023. Numerical modeling of the drying behavior of Adlai (*Coix lacryma-jobi* L.) grain. The Palawan Scientist, 15(2): 55-68.

ABSTRACT

The study aimed to develop computational fluid dynamics (CFD) models for simulating the drying performance of Adlai grain during convective drying with an air temperature range of 30°C to 60°C at around 10% to 80% relative humidity (RH). Before CFD modeling, the calculation of selected thermophysical properties of Adlai through mathematical modeling of its food constituents and thin-layer drying experiments were conducted. The simulation of heat and mass (moisture) transfer and visualization of moisture and temperature gradients in Adlai grain during drying were carried out using Analysis Systems (Ansys) Student 2020 R2 software package, specifically the Fluent solver. Results showed that the CFD models exhibited good agreement with the actual drying performance of Adlai. The models were validated using three statistical parameters: coefficient of determination (R^2), standard error (S), and percent mean deviation modulus (P%). The R^2 values ranged from 0.94-0.98; the S values ranged from 0.0018-0.0066; and the P% values ranged from 6.5%-8.68%. Overall, the models were deemed acceptable in estimating the moisture content of Adlai due to high R^2 values, low S values, and P% values of less than 10%. The results validate the use of CFD as a reliable method for predicting the drying performance of Adlai, which contributes to the optimization of the drying process, the improved designing of drying systems, and the enhancement of product quality.

Keywords: grain drying, hot air, multiphysics, simulation

INTRODUCTION

The Bureau of Agricultural Research (BAR) has initiated research and development activities on Adlai (*Coix lacryma-jobi*) since 2011. It saw the highly nutritious Adlai grain or "Job's tears" as a potential alternative to rice as a staple food. Approximately, the Adlai grain contains the following: 9.9-10.8% water; 13.6-19.1% protein; 5.7-6.1% fat; 58.5–62.7% carbohydrate; 8.4% fiber and 2.2-2.6% ash (Aradilla 2018). Compared to rice and corn, Adlai has higher food energy, carbohydrates, protein, fat, and dietary fiber. It also has the following minerals: calcium, phosphorus, iron, niacin, thiamine, and riboflavin (Peñaflor et al. 2014). Three of its varieties are endemic in the Philippines – "guilian", "ginampay", and "pulot". Research and other related activities have also been done by other agencies such as the Department of Agriculture (DA) and the Philippine Center for Post-Harvest Mechanization and

Development (PhilMech) to study and enhance Adlai's production, post-harvest operations, and commercialization.

Currently, Adlai is grown and consumed in areas such as Zamboanga del Sur, Isabela, Batangas, Caraga Region, and the Bicol Region. The production of Adlai follows the same traditional method for rice production. The "ginampay" variety of Adlai could produce a yield of 3.4 tons/ha, which is just slightly lower than the average rice yield of 3.87 tons/ha. The traditional processing of Adlai after harvesting involves drying and milling. Sun-drying of threshed grains occurs two days before milling (Aradilla 2018). Unhulled Adlai grains sell for around PHP 200.00 per kg, while milled grains go for around PHP 300.00 to PHP 500.00 per kg.

There are studies on the processing of Adlai into several products, such as ice cream (Khongjeamsiri 2007), yogurt (Keeratibunharn and Krasaekoopt 2013), and saltine crackers (Andoy et al. 2019). However, some of its post-harvest qualities, such as its drying characteristics and equilibrium moisture content (EMC), remain unknown. Drying is one of the most fundamental and indispensable unit operations in grain processing. It is performed to reduce the moisture content level in food and other biological materials with the aim to prolong its shelf life, reducing the probability of fungi development, and facilitating further processing to obtain a finished product available for consumption, utilization, and other purposes. For cereal grains like Adlai, proper drying must be performed to improve grain quality and storage time. Convective and radiation drying methods are the two general types of drying methods used for grains. These methods are embodied in the commonly used and preferred drying operations in the Philippines: sun-drying and convective drying. The latter is a complex process that involves simultaneous heat and mass (moisture) transfer, change in physical properties, and shrinkage of biological material (Kumar et al. 2012). Convection drying is performed by supplying heated air to a batch of grains via a blower or fan. Moisture removal results from the vaporization of moisture before being taken away by the air stream.

Convection drying of agricultural products, such as grains, is both energy and time-consuming. The food processing industry needs to obtain high-quality dry products utilizing only the lowest possible amount of energy input, including labor, and the shortest drying time. With the powerful computing capabilities of programs like Ansys Fluent, Ansys CFX, COMSOL Multiphysics, etc. numerical modeling of the drying phenomena in grains became achievable. This is done by computational fluid dynamics (CFD) simulation employed by such programs to aid engineers and scientists in solving multiphysics problems involving mass, momentum, and energy transfer. In studying the drying kinetics of agricultural and biological products, CFD has become a common practice among food engineers and technologists due to its energy, time, and cost-saving benefits in contrast to laborious experimentation. However, actual experiments are still helpful in validating the models. For grains like Adlai, a well-developed CFD model can provide a more accurate and efficient description of its drying behavior.

The study aimed to develop CFD models for simulating the drying performance of Adlai grain by numerical modeling of the heat and mass (moisture) transfer in the kernel during convective drying. Specifically, the study aimed to calculate the selected thermophysical properties of Adlai grain needed for CFD simulation; to perform a thin-layer drying experiment of Adlai grain, to perform CFD modeling using multiphysics software, and to validate the CFD-generated drying curves of Adlai grain with the experimental results. Through numerical simulations, predicting the drying behavior of Adlai under various drying conditions would be possible and would contribute to optimizing further drying systems, equipment, and practices for Adlai.

METHODS

Thermophysical Properties of Adlai

Values for selected thermophysical properties of Adlai were calculated using mathematical models developed by Choi and Okos (1986) that used the proximate composition or fraction of food constituents of the product (Ibarz and Barbosa-Canovas 2014). The models or equations used in the study were expressed as a function of temperature in the range of -40°C to 150°C. These equations are presented in Table 1.

Properties of the Drying Air

The properties of the drying air used in the convection drying of Adlai are necessary in developing the CFD models. They were used in the material properties panel of the fluid cell zone of the models. Table 2 presents the values for the different air properties used in the CFD simulations.

Thin-Layer Drying Experiment

The initial moisture content of sample Adlai grains in MC d.b. (moisture content dry basis) was calculated using the conventional air oven method, following the recommended procedures from the American Society of Agricultural Engineers (ASAE) Standards for moisture measurement of unground grain and seeds. There is no recommended oven temperature, sample size, and heating period for Adlai yet. However, for the purpose of the study, the maximum allowable oven temperature of 130°C was used along with the standard sample size of 10 g and

heating period of 18 h. This method was also adopted by Kim et al. (2016) in thin-layer drying of sorghum. The study used the "guilian" variety of Adlai due to its availability and cultivation for human consumption.

The grain samples were stored at 10°C in cold storage for seven days and were subjected to room temperature 24 h prior to the commencement of the thin-layer drying experiment. A tunnel dryer consisting of a blower, ducts, a heating element, and a temperature controller was used to supply heated drying air to the single layer of Adlai grains resting on a perforated stainless-steel drying tray. The mass of the grains used was around 35 g per replication. The dryer's schematic design is shown in Figure 1.

Table 1. Mathematical models used to estimate the thermophysical properties of Adlai (Ibarz and Barbosa-Canovas 2014; Carson et al. 2016).

Property	Food Component	Property Model (*t = temperature in °C*)	Equation/s
Thermal conductivity (k), W/m-K	Protein	$k = 1.7881E\text{-}01 + 1.1958E\text{-}03t - 2.7178E\text{-}06t^2$	$k_I = \frac{\Sigma(k_i v_i)}{\Sigma v_i}$ $k_{III} = \frac{(3v_a-1)k_a+[3(1-v_a)-1]k_I+\sqrt{\{(3v_a-1)k_a+[3(1-v_a)-1]k_I\}^2+8k_Ik_a}}{4}$ where: k_I = thermal conductivity from Parallel Model, W/m-K k_{III} = thermal conductivity from Effective Medium Theory model, W/m-K v_a = volume fraction of air v_i = volume fraction of food constituent k_a = thermal conductivity of air, W/m-K
	Fat	$k = 1.8071E\text{-}01 - 2.7604E\text{-}04t - 1.7749E\text{-}07t^2$	
	Carbohydrate	$k = 2.0141E\text{-}01 + 1.3784E\text{-}03t - 4.3312E\text{-}06t^2$	
	Fiber	$k = 1.8331E\text{-}01 + 1.2497E\text{-}03t - 3.1683E\text{-}06t^2$	
	Ash	$k = 3.2962E\text{-}01 + 1.4011E\text{-}03t - 2.9069E\text{-}06t^2$	
Density (ρ), kg/m³	Protein	$\rho = 1.3299E\text{-}03 - 5.1840E\text{-}01t$	$\rho = \frac{(1-\varepsilon)}{\Sigma(x_i/\rho_i)}$ where: ρ = true density, kg/m³ ε = porosity x_i = mass fraction of food constituent ρ_i = density of food constituent, kg/m³
	Fat	$\rho = 9.2559E02 - 4.1757E\text{-}01t$	
	Carbohydrate	$\rho = 1.5991E03 - 3.1046E\text{-}01t$	
	Fiber	$\rho = 1.3115E03 - 3.6589E\text{-}01t$	
	Ash	$\rho = 2.42385E03 - 2.8063E\text{-}01t$	
Specific heat (C_p), kJ/kg-K	Protein	$c_p = 2.0082 + 1.2089\ E\text{-}03t - 1.3129\ E\text{-}06t^2$	$c_u = \Sigma(c_i x_i)$ where: c_u = specific heat, kJ/kg-K c_i = specific heat of food constituent, kJ/kg-K x_i = mass fraction of food constituent
	Fat	$c_p = 1.9842 + 1.4733E\text{–}03t - 4.8008E\text{-}06t^2$	
	Carbohydrate	$c_p = 1.5488 + 1.9625E\text{-}03t - 5.9399\ E\text{-}06t^2$	
	Fiber	$c_p = 1.8459 + 1.8306E\text{-}03t - 4.6509E\text{-}06t^2$	
	Ash	$c_p = 1.0926 + 1.8896\ E\text{-}03t - 3.6817\ E\text{-}06t^2$	
Water	Thermal conductivity	$k_w = 5.7109\ E\text{-}01 + 1.7625E\text{-}03t - 6.7036E\text{-}06t^2$	
	Density	$\rho_w = 9.9718E02 + 3.1439E\text{-}03t - 3.7574E\text{-}03t^2$	
	Specific heat (for temperature range of 0 to 150 °C)	$c_w = 4.1289 - 9.0864\ E\text{-}05t + 5.4731E\text{-}06t^2$	

The Adlai grain samples were subjected to forced heated air drying at three drying air temperatures: 30°C (ambient), 45°C, and 60°C. These temperature values were selected for the study since a drying air temperature of 30°C represents the average ambient air temperature; 45°C drying air was used relative to maintaining seed viability; and 60°C drying air was used for commercial drying. A constant air velocity of around 1 m/s was used during the experiment. The drying air temperature was maintained during drying via a temperature controller (Elitech STC-1000 Temperature Controller), while the velocity of the drying air was monitored via an anemometer (PEAKMETER® Digital Anemometer PM6252A).

Table 2. Air properties used at various drying air temperatures.

Property	Drying Air Temperature (°C)			References
	30	45	60	
Density, kg/m^3	1.164	1.109	1.059	Cengel and Cimbala 2014
Specific heat, J/kg-K	1007	1007	1007	
Thermal conductivity, W/m-K	0.02588	0.02699	0.02808	
Dynamic viscosity, kg/m-s	1.87 x 10^{-05}	1.94 x 10^{-05}	2.01 x 10^{-05}	
Diffusion coefficient of water into air, kg/m-s	3.118 x 10^{-05}	3.299 x 10^{-05}	3.469 x 10^{-05}	The Engineering ToolBox 2018

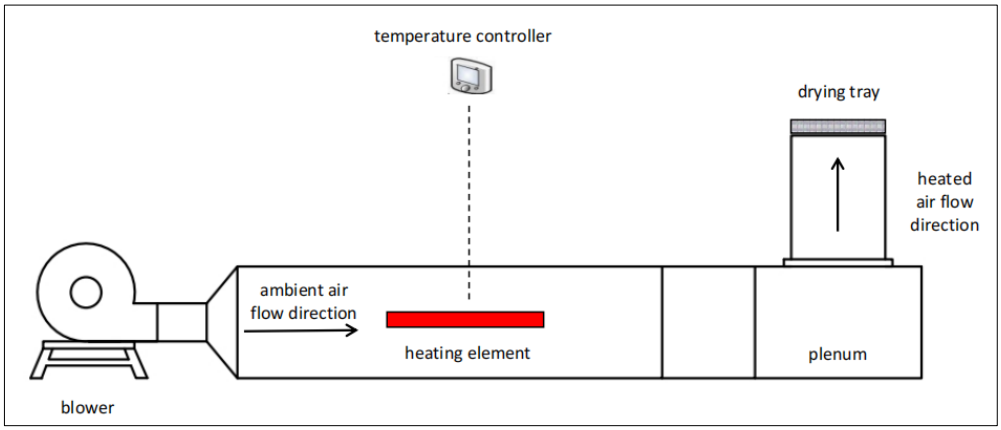

Figure 1. Schematic of the dryer used for thin-layer drying of Adlai.

The relative humidity (RH) during drying was monitored using a digital thermohygrometer (Senze Instruments Digital Hygro Thermometer TH-D-TH06OH). The change in mass of the grains was recorded manually at intervals recommended by ASAE standards: every 5 seconds during the first 5 min, every 1 min during the next hour, and every 15 min after that. An electronic balance was used for calculating the change in mass of the grain samples (Shenzhen Big Dipper Scale Co., Ltd., BDS-PN PN602A). Subsequently, the drying curve was generated from the experiment. Drying was performed until equilibrium was reached between the Adlai grains and the drying air. The experiment was conducted in triplicate per treatment of drying air temperature.

Fick's second law of diffusion was also used to describe the drying phenomenon since thin-layer drying occurred in the falling rate period, and diffusion of moisture inside the kernel is the resistance factor governing the process. The simplified diffusion model is based on the solution of Henderson's moisture diffusion law (Kim et al. 2016). The model is expressed as:

$$MR=Aexp(-kt) \quad (1)$$

where A and k are model constants. The drying constant, k, is expressed as per unit time. The time duration of drying is represented by t, usually in hours or minutes.

The average effective diffusivity (D_e) values of Adlai grain moisture at different drying air temperatures were calculated from the experimental drying curves and were used in the CFD simulations. It was assumed to be constant during the drying process. The effect of drying air temperature on effective diffusivity was represented through an exponential model (Peleg et al. 2012) expressed as

$$D_e = D_o exp(cT_a) \quad (2)$$

where D_e is the effective diffusivity (m^2/s), D_o is a diffusivity at infinite high temperature, c is a constant (1/K), and T_a is the drying air temperature (K).

Computational Fluid Dynamics (CFD) Drying Simulation of Single Adlai Kernel

Thin-layer drying can be considered as grain being immersed in fluid (Prakash and Pan 2011); hence, its mechanism can be described by single kernel drying and its governing equations. This was reflected in the study of Chen et al. (2023) on the heat and mass transfer modeling of a single-particle peanut, wherein the numerical model was validated by a thin-layer drying experiment using hot air. The following steps were adopted to create the CFD drying models for a single Adlai kernel: (1) generating the model geometry, (2) mesh/grid generation, (3) setting up the Fluent solver, (4) numerical solution with Fluent, and (5) post-processing. The multiphysics software used for the study was Ansys Student 2020 R2, which is a free academic version of the Ansys software package. Computational fluid dynamics simulations were explicitly conducted using the Fluent solver of Ansys Student.

The 3D teardrop geometry representing the Adlai or "Job's tears" kernel was made using AutoCAD 2016 software by Autodesk®. The average major and minor axes of the kernel were calculated from the measurement of 20 Adlai grain samples using a Vernier caliper (1/128 in). The 3D Adlai model was further enhanced when imported into DesignModeler, an object-generating component of Fluent, as shown in Figure 2. The flow field for the drying air was added as an enclosure surrounding the kernel geometry. The mesh of the CFD simulations resulted in 212,436 elements and 43,710 nodes. Since the study used the Ansys Student version only, the mesh was refined to a level where further refinement did not enhance the results of the numerical solution. Unstructured tetrahedral elements were used as recommended for 3D meshing. Inflation was used on the walls of the kernel for improved gradient calculation. Quadrilateral cells were used for inflation along the surface of the kernel. The mesh of the kernel geometry is presented in Figure 3.

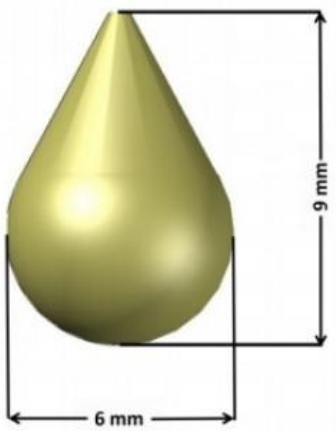

Figure 2. The 3D geometry of single Adlai grain.

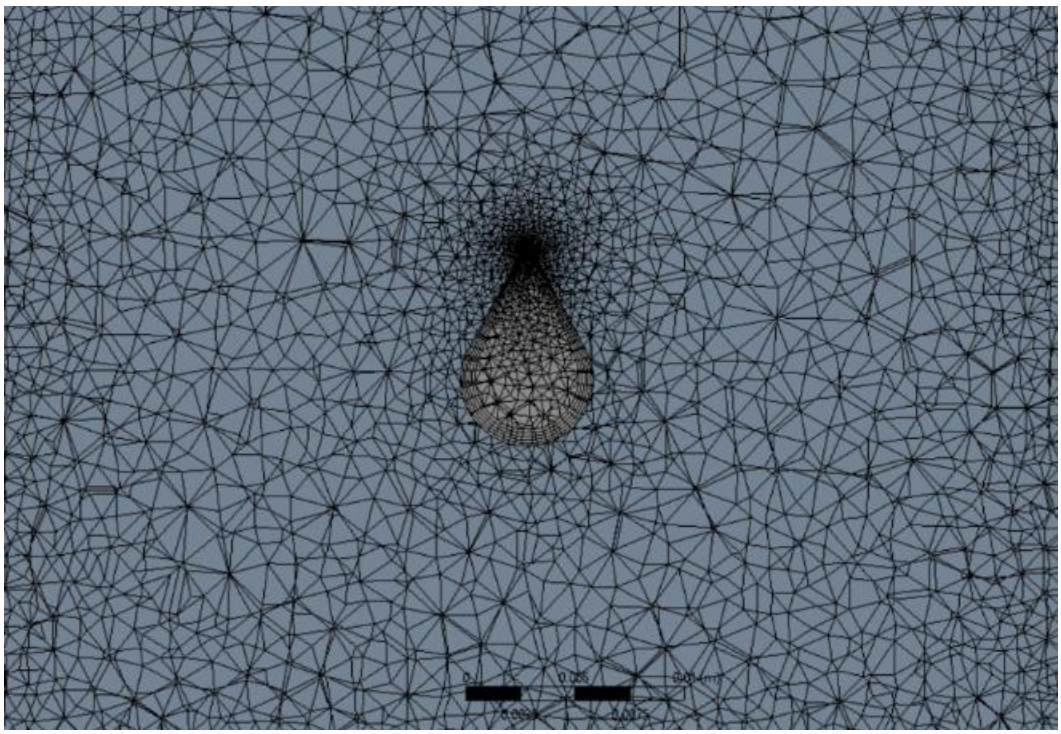

Figure 3. Unstructured mesh (cross-section) of the computational fluid dynamics (CFD) model for convective drying of Adlai grain.

Before proceeding with the development of the CFD simulations using Fluent, specific assumptions about the model were established based on the earlier works of other researchers in the field of CFD and its applications in drying biological products. The following were the governing assumptions adopted for the CFD models in the study: (1) no variation in shape and size of the kernel during drying, (2) the kernel is considered homogeneous, (3) uniform moisture distribution, (4) constant effective diffusivity and convective mass transfer coefficient during diffusion, (5) diffusion is the only transport mechanism of moisture inside the kernel, (6) moisture transfer to the drying air only occurs at the kernel surface, and (7) no volumetric heat generation within the kernel (ElGamal et al. 2014; Chilka and Ranade 2018). The geometry used in the simulations was considered a homogeneous lumped model of the Adlai grain. The thermophysical properties of the grain were applied to the lumped model's entirety because there is no available information from literature on the specific values for the endosperm, bran, and hull of Adlai. Furthermore, grains, in general, are practically dried as a whole with the kernel, bran, and husk layers intact, so a single-component model for Adlai grain is acceptable, at least for the study.

A non-conjugate diffusion-based model was used in this study wherein the heat and mass transfer inside the product are computed without affecting the flow, temperature, and water vapor concentration in the flow field of the drying air. To model the moisture content inside the product, an effective diffusivity is used, which is obtained only through experimentation. The boundary conditions at the interface require values of convective heat transfer coefficient and convective mass transfer coefficient to account for the heat and mass exchange between the product and the drying air (Sun 2019).

In the numerical solution using the Fluent solver, the steady state solution was done before conducting the transient simulation, where the drying air temperature near the kernel surface is set at the initial kernel temperature, and the moisture content of the air is in equilibrium with the kernel's (Sun 2007). Constant air velocity (1 m/s) and temperature (30°C, 45°C, and 60°C) were used at the air inlet. The drying air originated from the bottom of the domain. Zero temperature and moisture gradients were placed on the walls of the flow field. The moisture content of the drying air was not considered in the simulations due to the non-conjugate approach adopted for the study. The SST-kω model was used for turbulence modeling. An initial value for the temperature and moisture of the kernel was set. The initial moisture content (M_0) was 0.1867 MC d.b. while the kernel temperature (T_0) was set to 27°C. The initial conditions for the first stage of the solution were:

$$M(x,y,z,0) = M_0 \quad (3)$$

$$T(x,y,z,0) = T_0 \quad (4)$$

User-Defined Scalar (UDS) equation was used to simulate the moisture content within the kernel. Ansys Fluent solver uses the following UDS equation:

$$\frac{\partial \rho \phi_k}{\partial t} + \frac{\partial}{\partial x_i}\left(\rho u_i \phi_k - \Gamma_k \frac{\partial \phi_k}{\partial x_i}\right) = S_{\phi_k} \quad k=1,\ldots,N \quad (5)$$

From left to right, an unsteady term, convective term, diffusion term, and source term comprise the UDS equation as presented in Equation 5. Since it was assumed that the primary driving force for the drying of the kernel is diffusion, only the unsteady and diffusion terms were considered for the model (Chilka and Ranade 2018).

After the steady state solution, the weighted average values of the convective heat transfer coefficient (h) were calculated at the concentration profile of the air control volume next to the kernel surface. The h values were used for the heat flux at the air-kernel interface. The convective mass transfer coefficient (h_m) was calculated from its relationship with the effective diffusivity, D_e, and drying constant, k (1/s):

$$D_e = \frac{kr^2}{\pi^2} \quad (6)$$

$$k = h_m\,(A/V) \quad (7)$$

where r is the characteristic length of the grain (m), A is the surface area of the kernel (m^2), and V is the volume of the kernel (m^3). The volume and surface area of the kernel were obtained by calculating the cell volume and cell surface area of the 3D object (Adlai kernel) through Fluent, respectively.

The Neumann boundary condition was used at the air-kernel interface of the grain model. This boundary type assumes constant convective heat and mass transfer coefficients (ElGamal et al. 2014). This type of boundary condition is most commonly used due to its simplicity. The h_m values were assumed to be constant during the drying process and were used for the formulation of the mass flux equation at the interface, while the D_e values were used as inputs for the material properties of the kernel. The heat and mass flux boundary conditions at the air-kernel interface were as follows:

$$-q = h(T_s - T_\infty) \quad (8)$$

$$-\dot{m} = h_m(M_s - M_e) \quad (9)$$

In Equation 8, q is the heat flux (W/m^2), h is the convective heat transfer coefficient (W/m^2-K), T_s is the surface temperature of the kernel (K), and T_∞ is the drying air temperature (K). In Equation 9, $\dot{m}$ is the

mass flux, h_m is the convective mass transfer coefficient (m/s), M_s is the surface moisture of the grain ($kg_{water}/kg_{dry\ matter}$), and M_e is the equilibrium moisture content of the grain ($kg_{water}/kg_{dry\ matter}$).

The equations representing the boundary conditions were directly imposed on the air-kernel interface via the named expressions feature of Ansys Fluent. This has become an alternative method to the commonly used CFD technique of writing user-defined functions (UDFs).

The CFD simulations were run on an Acer Nitro AN515-55, Intel Core i7-10750H, 2.60 GHz laptop. For pressure-velocity coupling, the SIMPLE (Semi-Implicit Method for Pressure-Linked Equations) algorithm was used. For pressure, momentum, energy, turbulence, and UDS equations second order discretization scheme was used. Residuals for energy, flow, and UDS equations were set at 1×10^{-05}. Transient simulations were carried out at a time step size of 1s with 10 iterations per time step. This time step size was used in the study because there was observable modeling difficulty when using smaller time steps. For this reason, 1s was considered the minimum time step size for the best possible model accuracy given the study's parameters. The termination time of simulation was 1,265 min, 1,145 min, and 785 min for 30°C, 45°C, and 60°C drying air temperature, respectively. The modeling time went on from 16.5 h to 18 h per simulation.

The volume-weighted averages of the moisture content (UDS Scalar 0) in the kernel domain were calculated at the end of each specified number of time steps to determine the average moisture content of the kernel. These values were recorded to constitute the predicted drying performance by the CFD model.

Validation of the CFD Models

To validate the acceptability of the simulated drying curves resulting from CFD modeling, specific statistical parameters were used as basis. These parameters determine the model accuracy and goodness-of-fit with respect to the experimental data from the thin-layer drying experiment. These statistical parameters were the coefficient of determination (R^2), the standard error (S), and the percent mean deviation modulus (P%). The latter must be less than 10% for the model to be acceptable (Mohapatra and Rao 2005).

The R^2 and S values were calculated through the built-in data analysis tools in Microsoft Excel 2016 while the P% values were calculated using the equation:

$$P\% = \frac{100}{n} \Sigma \frac{abs(M_i - M_{pre})}{M_i} \quad (10)$$

where M_i is the moisture content from the experiments, M_{pre} is the predicted moisture content from the CFD simulations, and n is the number of observations. It should be noted that the predicted and experimental moisture values compared were of the same time step.

RESULTS

Thermophysical Properties of Adlai

The thermophysical properties of Adlai used in the CFD simulations were estimated using mathematical models involving the food constituents of the product. The estimated values of thermal conductivity, specific heat, and true density of Adlai are presented in Table 3. For drying air temperature range of 30°C to 60°C, the thermal conductivity of Adlai ranged from 0.1491 to 0.1628 W/m^2-K, the specific heat ranged from 1,986 to 2,024 J/kg-K, and the true density ranged from 885 to 892 kg/m^3.

Table 3. Estimated thermophysical properties, effective diffusivity and convective mass transfer coefficients of Adlai grain at different drying air temperatures.

Property	Drying Air Temperature (°C)		
	30	**45**	**60**
Thermal conductivity (W/m-K)	0.1491	0.1563	0.1628
Specific heat (J/kg-K)	1986	2006	2024
True density (kg/m^3)	892	889	885
Effective Diffusivity, D_e (m^2/s)	2.772×10^{-12}	4.678×10^{-12}	7.277×10^{-12}
Convective mass transfer coefficient, h_m (m/s)	2.701×10^{-08}	4.558×10^{-08}	7.090×10^{-08}

Thin-layer Drying of Adlai

A single layer of Adlai grains was subjected to forced heated air drying using 30°C, 45°C, and 60°C at around 10% to 80% RH. The initial moisture content of the sample grains was determined to be 0.1867 MC d.b. The moisture content at specified intervals during drying was measured and recorded manually. The moisture of the grains was expressed as moisture ratio (MR) and was plotted against the drying time to generate the drying curve at different drying air temperatures. Figure 4 presents the drying curves from the thin-layer drying experiments.

Since there are no EMC values for Adlai grain available in literature, the final moisture contents at the end of the thin-layer drying experiments were adopted as approximate EMC values. The EMC values for drying air temperatures of 30°C, 45°C, and 60°C were around 13%, 11%, and 9% MC d.b., respectively.

The average drying time for the grains to reach equilibrium with the drying air was 1,265 min (21 h), 1,145 min (19 h), and 785 min (13 h) for drying air temperatures of 30°C, 45°C, and 60°C, respectively at 10% to 80%. RH.

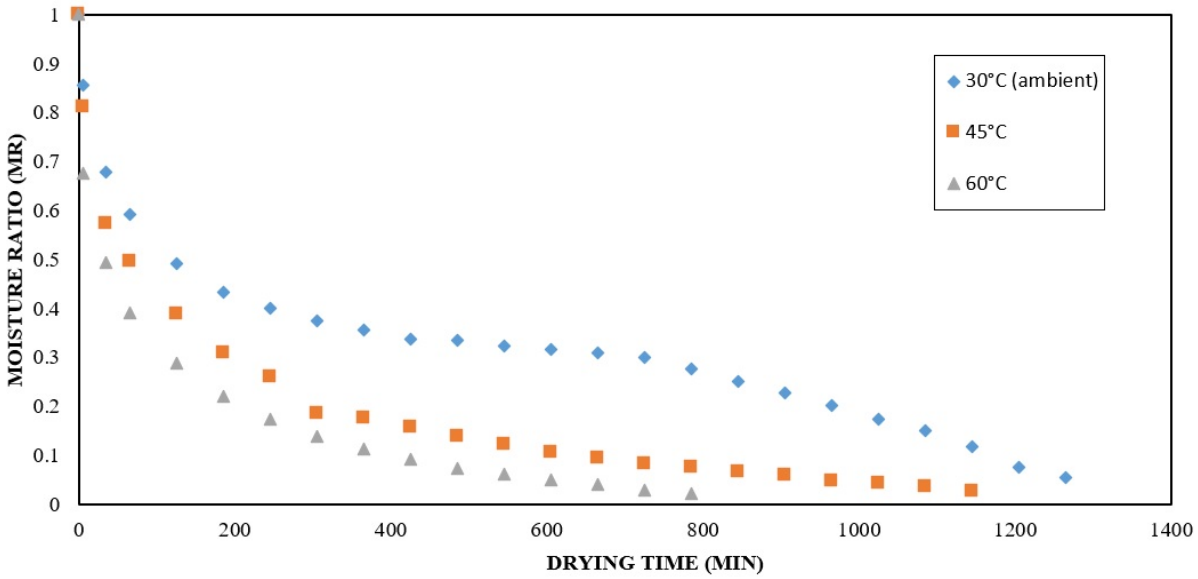

Figure 4. Experimental drying curves of Adlai grain at different drying air temperatures.

Table 4 summarizes the model constants and the average drying rates for each drying air temperature. At the drying air temperature range of 30°C to 60°C, the model constants *A* and *k* were observed to be 0.7386 to 0.8097 and 0.002 to 0.007 per min, respectively. For the same range, the average dying rate was between 0.2479 and 0.6969 % MC d.b. per h of drying.

Table 4. Simplified diffusion model constants and average drying rate during thin-layer drying of Adlai.

Drying Air Temperature (ºC)	MR = A·exp(-kt)		R^2	Average Drying Rate (% MC d.b./h)
	A	k (1/min)		
30	0.7386	0.002	0.8843	0.2479
45	0.8097	0.004	0.9451	0.3715
60	0.7878	0.007	0.9260	0.6969

The effective diffusivity (D_e) of moisture in the Adlai grain for each drying air temperature was calculated using Equation 6. The D_e values were calculated by plotting *lnMR* against drying time. The average values of the effective diffusivity are presented in Table 3. In the drying air temperature range of 30°C to 60°C, the effective diffusivity value of Adlai grain moisture ranged from 2.772×10^{-12} to 7.277×10^{-12} m^2/s.

Temperature has a more significant effect on the drying process of grains compared to the initial moisture content. The effect of temperature on the effective diffusivity was expressed through an exponential model. The values of lnD_e were plotted against the absolute drying air temperature. The plot is presented in Figure 5. The exponential model was formulated as follows:

$$D_e = 36.35exp(0.0322T_a) \quad (11)$$

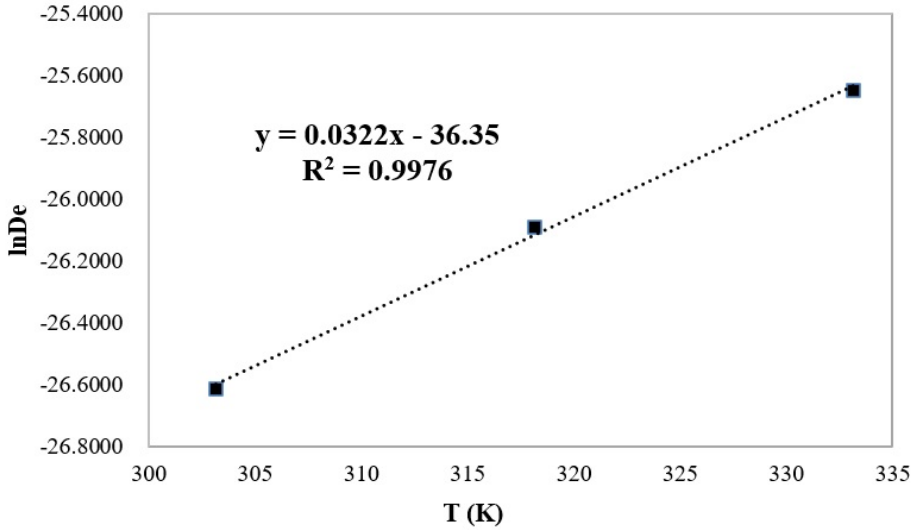

Figure 5. Plot of lnD_e vs drying air temperature (K) used in convective drying of Adlai grain.

The value for the diffusivity at infinite high temperature, D_o, was found to be 36.35, while the value of constant *c* was found to be 0.0322. The slope of the curve gives the constant *c* while the intercept gives the D_o.

The average convective mass transfer coefficient (h_m) values used to formulate the mass flux equation at the air-kernel interface of the CFD model were derived using Equation 7. The h_m values used in the study are presented in Table 3. The h_m values for Adlai kernel varied from 2.701×10^{-08} to 7.090×10^{-08} m/s for 30°C to 60°C drying air temperature. The values presented were necessary inputs for the mass flux equation at the air-kernel interface of the CFD simulations.

Computational Fluid Dynamics (CFD) Drying Simulation of Single Adlai Kernel

The average moisture content at each time interval was calculated by determining the volume-weighted average of the UDS Scalar 0 (moisture content) in the kernel domain. Figures 6-8 show the simulated moisture values from the CFD simulation and the experimental moisture values at different drying air temperatures. The drying performance of Adlai was described by the drying curves obtained by simulating the heat and moisture transfer within the Adlai grain at different drying air temperatures.

The temperature and moisture profiles within the Adlai kernel during drying can also be calculated and shown using the post-processing unit of the Fluent solver. Tables 5 and 6 show these profiles. Both the average temperature and moisture content of the kernel were determined by calculating the volume weighted average of static temperature and UDS Scalar 0 (moisture content), respectively.

Validation of the CFD Models

The experimental drying performance of Adlai grain was compared with the predicted drying performance generated by the CFD simulations. The accuracy of the fit was explained through the coefficient of determination (R^2) and the standard error (S). The percent mean deviation modulus (P%) was used to define model accuracy. These values are presented in Table 7. At the drying air temperature range of 30°C to 60°C, the R^2 values ranged from 0.94 to 0.98, S values ranged from 0.0018 to 0.0066, and P% values ranged from 6.5% to 8.68%, respectively.

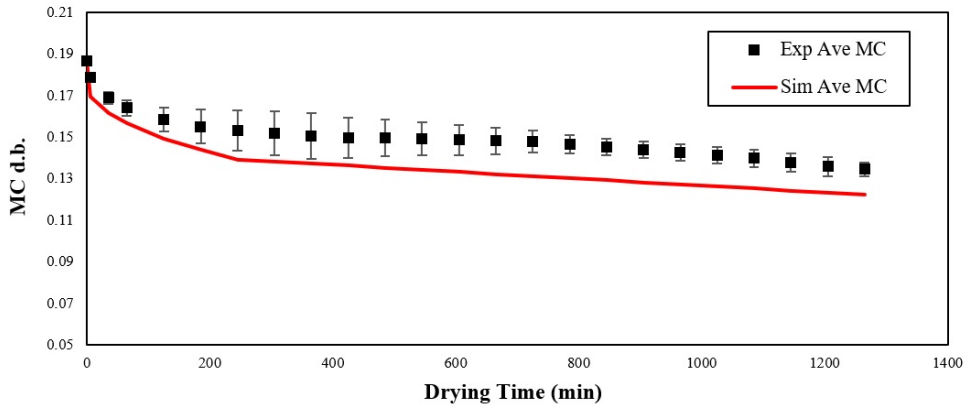

Figure 6. Experimental and predicted drying curves of Adlai at 30°C drying air temperature.

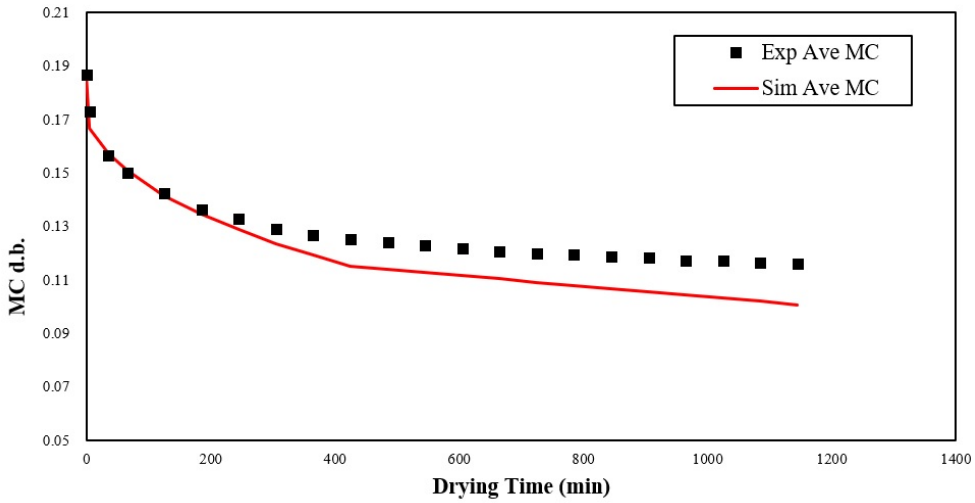

Figure 7. Experimental and predicted drying curves of Adlai at 45°C drying air temperature.

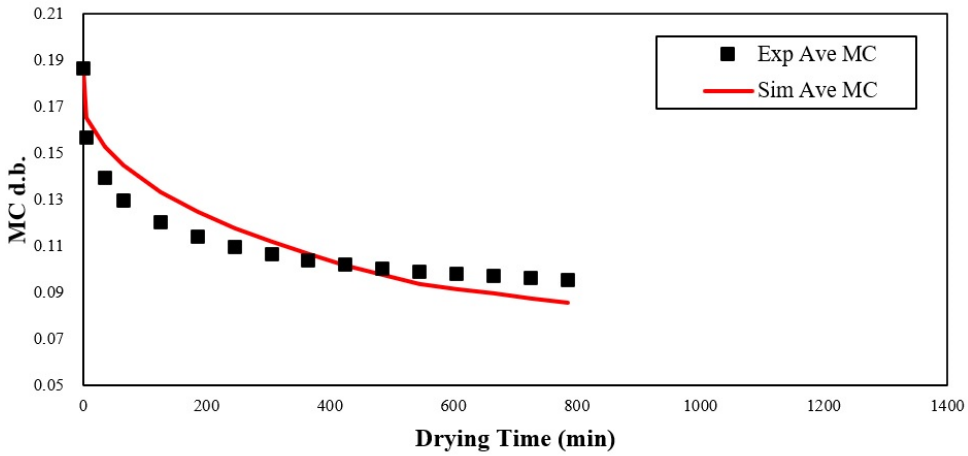

Figure 8. Experimental and predicted drying curves of Adlai at 60°C drying air temperature.

Table 5. Moisture profile of Adlai kernel at 60°C drying air temperature.

Legend	Moisture Profile			
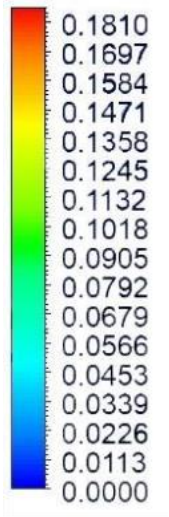	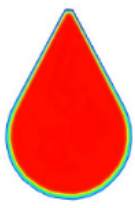	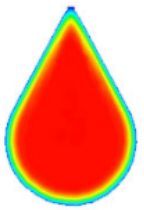	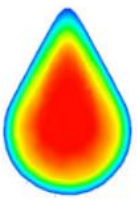	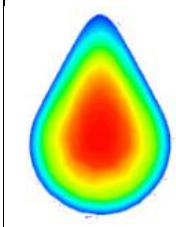
	Moisture Content (d.b.) and Drying Time (min)			
	0.1653 t = 5 min	0.1148 t = 65 min	0.1119 t = 305 min	0.0917 t = 605 min

Table 6. Temperature field and profile of Adlai kernel at 60°C (333.15 K) drying air temperature.

Legend	Temperature Profile		
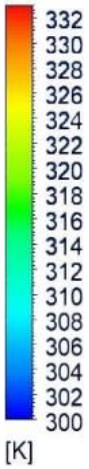	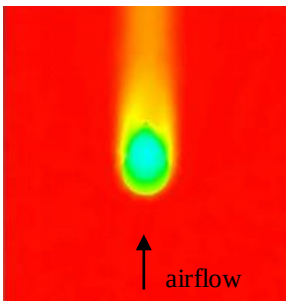	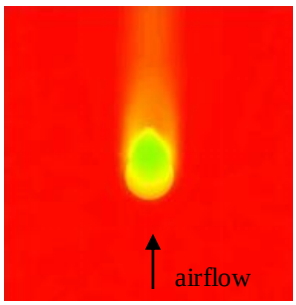	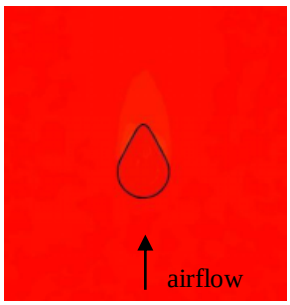
	Temperature (K) and Drying Time (s)		
	T = 316 K t = 30 s	T = 324 K t = 60 s	T = 332 K t = 150 s

Table 7. Statistical parameters indicating model accuracy.

Drying Air Temperature (°C)	R^2	S	P%
30	0.98	0.0018	8.68
45	0.98	0.0027	6.94
60	0.94	0.0066	6.50

DISCUSSION

Thermophysical Properties of Adlai

Standard experimental methods for calculating selected thermophysical properties of Adlai were not performed since the study was conducted during the COVID-19 pandemic when there were restrictions to travel, work, and other activities. Estimation of the values through mathematical modeling was the available alternative.

Mathematical modeling of the thermophysical properties of food was used in the study to calculate the values of thermal conductivity, specific heat, and true density of Adlai, which were necessary inputs for the CFD simulations. These values were used in the material properties panel for the solid cell zone of the CFD models, representing the Adlai kernel. It was observed that the estimated thermal conductivity and specific heat of the Adlai grain increased as the assumed kernel temperature increased, while the opposite was observed for the estimation of true density.

Thin-layer Drying of Adlai

According to the drying curves presented in Figure 3, it was observed that the lower the drying air temperature used, the longer the drying time to reach equilibrium. Higher drying air temperature is usually accompanied by a lower RH, allowing for higher moisture transfer between the kernel and the surrounding air. As shown in Table 4 higher average drying rates (% MC d.b. per h) are achieved at higher air temperatures and lower RH. The average drying rate shows the amount of percent moisture reduction during drying. However, it does not show the high initial moisture removal rate at the beginning of drying since it is averaged over the entire drying time.

The accuracy of the fit of the simplified diffusion model with the experimental drying curves of Adlai grain improved as the drying air temperature increased. This observation was based on the increase in the R^2 value between the models and the experimental drying curves. At higher drying temperatures, the R^2 values were over 0.9 which indicate better fit of the model values with the experimental moisture values from the thin-layer drying experiment.

It was observed that the effective diffusivity of moisture within the grain increased proportionally with the drying air temperature. This was also observed by Jha and Tripathy (2021) in their simulation of heat and mass transfer of solar drying of paddy. For cereal grains, the effective diffusivity found in literature falls within the range of 10^{-13} to 10^{-08} m^2/s. Based on this condition, the estimated D_e values of Adlai fall within the accepted range. The effective diffusivity of the Adlai grain's moisture is associated with higher drying rates when higher drying air temperatures are used. This is because more moisture diffuses and leaves the kernel when it is exposed to higher air temperatures at lower RH. The moisture diffusion within the kernel was less affected by the internal resistances at higher drying air temperatures.

The convective mass transfer coefficient (h_m) describes the rate of moisture transfer from the surface of the kernel to the drying air, thus affecting the moisture reduction rate within the kernel's volume. It was observed that the higher the temperature of the drying air, the higher the h_m value. This was also similar with the data of Nguyen et al. (2019) in the study of experimental and numerical investigation of transport phenomena and kinetics of convective shrimp drying. The convective mass transfer coefficient values calculated in this study indicate that the moisture removal at the kernel's surface is more significant and occurs more rapidly at higher drying air temperatures. This is because at higher drying air temperatures, the relative humidity is usually lower, allowing for greater moisture transfer from the grain to the surrounding air.

Computational Fluid Dynamics (CFD) Drying Simulation of Single Adlai Kernel

Visually, the simulated drying performance of the Adlai grain via CFD modeling fitted closely with the experimental drying performance when plotted together. Agreement between the simulated and the experimental drying curves was better during the initial hours of drying and gradually deteriorated in the latter stages, which was also reported by Chandramohan (2016) in his coupled CFD model for convective drying of a moist object. The numerical models for 30°C, 45°C, and 60°C have the same initial moisture content of 0.1867 and duration of drying time as with the thin-layer drying experiments. However, the final moisture contents were different for simulated and experimental drying curves. The final moisture contents from simulated and experimental drying using 30°C-60°C drying air temperature were 0.1221 to 0.0857 MC d.b. and 0.1344 to 0.0955 MC d.b., respectively. From the data presented, it is clear that the numerical moisture values underestimated the experimental moisture values because the simulations approached the EMC of Adlai at a much faster drying time than the thin-layer drying experiments. For drying temperatures of 30°C, 45°C, and 60°C, the simulation approached Adlai's EMC at around 785 min, 665 min, and 605 min, respectively. The reason behind this could be the constant average values of effective diffusivity and convective mass transfer coefficients. Variable effective diffusivity and convective mass transfer coefficient values would get smaller as the drying process proceeds such that at later stages in drying, the moisture reduction in the model would not be as significant as using constant

values. This would make the agreement between the simulated and experimental moisture values better. Furthermore, the study did not consider physical changes in the grain, which can cause resistance to moisture diffusion and evaporation during the drying phenomenon. Changes such as shrinkage, cracking, and case hardening were not investigated while conducting the thin-layer drying experiments at different drying air temperatures. Nevertheless, these physical changes in the grain have been found out to have an effect on the rate of moisture removal during drying.

Aside from the drying performance over time, the moisture and temperature profiles during the CFD simulations of convective drying of Adlai grain can be visualized through Ansys Fluent. The apex of the Adlai grain model was positioned away from the drying air inlet of the simulation such that the drying air hit the bottom of the grain first. This was the geometric presentation chosen for the study since different orientations of the kernel to airflow direction did not show any effect on the average moisture content of the grain with similar drying conditions. This was also reported by ElGamal et al. (2014) for the convective drying simulation of a single rice kernel. It was assumed that moisture transfer occurs at the kernel's surface, creating areas of varying moisture content within the kernel in the process, as shown in Table 5. It was observed that during the simulation of convective drying of a single kernel of Adlai, moisture reduction occurs much faster near the kernel's surface than the core. As shown in Table 5, as the drying time increased, the moisture content at the center of the grain decreased as well. The moisture diffused from the center of the grain to the surface, where moisture vaporization took place, leaving the regions near the surface with low moisture content. This was also observed in the numerical study of heat and mass transfer of peanut drying (Chen et al. 2023). Over time, the moisture at the core of the grain reduced further, as indicated by the recession of high moisture color bands in the model's geometric profile. The reduction of moisture content in the kernel affected the overall average moisture content of the entire kernel. This phenomenon eventually gave the final moisture content of the grain at the termination of the drying simulation. It was observed that high moisture concentration at the kernel's core would also give a high average kernel moisture value.

Heat transfer during the drying simulation occurred significantly faster than the mass transfer. This was also parallel in the works of Chilka and Ranade (2018) and Nguyen et al. (2019) in drying almond kernel and shrimp, respectively. It took only a short period of time for the kernel temperature to achieve thermal equilibrium with the drying air temperature as shown in Table 6. Over time, the color gradient in the kernel changed as the temperature increased and became approximately equal to the drying air temperature. At 150 s and further, the kernel temperature is in equilibrium with the drying air temperature. Colored streaks formed around the kernel, indicating its solid-fluid interaction with the moving drying air.

The heat transfer mechanism in Fluent is dependent on the thermophysical properties given to the solid (kernel) cell zone and the fluid (drying air) cell zone. These separate cell zones interact at the air-kernel interface, which has been treated as a coupled boundary between the solid and fluid cell zones.

Moisture and temperature profiles within the kernel via CFD modeling offer essential insights regarding its drying behavior. Moisture variation within the kernel allows the management of potential hygroscopically induced fissuring or cracking. Thus, the decision to incorporate tempering in the drying process could be made if necessary. Also, analyzing the moisture movement and variation within the kernel would help food technologists understand the diffusion mechanism of moisture from the endosperm to the husk to complete the moisture removal process at the surface. However, in the case of Adlai, this would entail further investigations of the properties of its endosperm, bran layer, and husk. When it comes to the temperature profile of grain, understanding the temperature variation within the kernel helps manage grain drying while minimizing the effects of thermal stress that may be caused by rapid drying. All of these are important to the food technologist since the drying rate of grain greatly affects the final quality of the kernels (Bonazzi et al. 1997).

Validation of the CFD Models

As shown in Table 7, the simulation for 60°C drying air temperature was the lowest in terms of R^2 value since it is the only one lower than 0.98. However, both models for 30°C and 45°C drying air temperature have higher P% values, which is indicative of higher deviation from the experimental data. In general, all the predicted models from the CFD simulations were acceptable due to their high R^2 values, low S values, and P% values of less than 10%. This means that CFD modeling is an acceptable technique for predicting the drying performance of Adlai grain under several convective drying temperatures. This method could be used apart from full-scale experimentation, which is deemed laborious, expensive, and time-consuming. CFD could be used to explore the behavior of Adlai under several other drying conditions.

FUNDING

This study would not have been possible without the support of the Department of Science and Technology – Engineering Research and Development for Technology (DOST-ERDT).

ETHICAL CONSIDERATIONS

No human or animals were involved nor harmed in the conduct of this study.

DECLARATION OF COMPETING INTEREST

The authors of this study declare that there are no competing interests of any kind with other authors.

ACKNOWLEDGMENTS

The authors would like to thank DOST-ERDT for being the primary funding agency of this research endeavor. Immense gratitude is extended by the corresponding author to those who contributed to the success of this study, as well as to his family, his friends, and the faculty members and staff of the University of the Philippines Los Baños – College of Engineering and Agro-Industrial Technology (UPLB-CEAT). The comments and suggestions of the two anonymous reviews helped improve the contents of this research work.

REFERENCES

Andoy CN, Enot IR, Mabaza AD and Quillo IC. 2019. Utilization of Job's tear (*Coix Lacryma-Joba L.*) flour as composite for all purpose flour in saltine crackers. American Journal of Biomedical and Life Sciences, 7(3): 52. https://doi.org/10.11648/j.ajbls.20190703.12

Aradilla, AR. 2018. Phenology, growth and yield performance of adlay (*Coix lacryma-jobi* L.) grown in adverse climatic conditions. International Journal of Research & Review, 5(3): 16-24.

Bonazzi C, Peuty MA and Themelin, A. 1997. Influence of drying conditions on the processing quality of rough rice. Drying Technology, 15(3-4): 1141-1157. https://doi.org/10.1080/07373939708917283

Carson JK, Wang J, North MF and Cleland DJ. 2016. Effective thermal conductivity prediction of foods using composition and temperature data. Journal of Food Engineering, 175: 65–73. https://doi.org/10.1016/j.jfoodeng.2015.12.006

Cengel YA and Cimbala JM. 2014. Property Tables and Charts. Fluid Mechanics: Fundamentals and Applications Third Edition. McGraw-Hill, New York, USA, 948 pp.

Chandramohan VP. 2016. Experimental analysis and simultaneous heat and moisture transfer with coupled CFD model for convective drying of moist object. International Journal for Computational Methods in Engineering Science and Mechanics, 17(1): 59–71. https://doi.org/10.1080/15502287.2016.1147506

Chen P, Chen N, Zhu W, Wang D, Jiang M, Qu C and Li Y. 2023. A heat and mass transfer model of peanut convective drying based on a two-component structure. Foods, 12: 1823. https://doi.org/10.3390/foods12091823

Chilka AG and Ranade VV. 2018. Drying of almonds I: single particle. Indian Chemical Engineer, 60(3): 232–254. https://doi.org/10.1080/00194506.2017.1333464

ElGamal R, Ronsse F, Radwan SM and Pieters JG. 2014. Coupling CFD and diffusion models for analyzing the convective drying behavior of a single rice kernel. Drying Technology, 32(3): 311–320. https://doi.org/10.1080/07373937.2013.829088

Ibarz A and Barbosa-Canovas GV. 2014. Thermal Properties of Foods. Introduction to Food Process Engineering First Edition. CRC Press, Taylor & Francis Group, Boca Raton, Florida, USA, pp. 198-207.

Jha A and Tripathy PP. 2021. Optimization of process parameters and numerical modeling of heat and mass transfer during simulated solar drying of paddy. Computers and Electronics in Agriculture, 187: 106215. https://doi.org/10.1016/j.compag.2021.106215

Keeratibunharn N and Krasaekoopt W. 2013. Development of Job's tears yogurt. Assumption University Journal of Technology, 16(3): 133–139.

Khongjeamsiri W, Wangcharoen W, Pimpilai S and Daengprok W. 2007. Preference direction study of Job's tears ice cream. Maejo International Journal of Science and Technology, 01(2): 137-144.

Kim HS, Kim OW, Kim H, Lee HJ and Han JW. 2016. Thin layer drying model of sorghum. Journal of Biosystems Engineering, 41(4): 357–364. https://doi.org/10.5307/jbe.2016.41.4.357

Kumar C, Karim A, Joardder MUH and Miller GJ. 2012. Modeling heat and mass transfer process during convection drying of fruit. In Gu, Y T & Saha, S (Eds.) Proceedings of the 4th International Conference on Computational Methods. Queensland University of Technology, Australia, pp. 1-8.

Mohapatra D and Rao PS. 2005. A thin layer drying model of parboiled wheat. Journal of Food Engineering, 66(4): 513–518. https://doi.org/10.1016/j.jfoodeng.2004.04.023

Nguyen MP, Ngo TT and Le TD. 2019. Experimental and numerical investigation of transport phenomena and kinetics for convective shrimp drying. Case Studies in Thermal Engineering. 14: 100465. https://doi.org/10.1016/j.csite.2019.100465

Peleg M, Normand MD and Corradini MG. 2012. The Arrhenius equation revisited. Critical Reviews in Food Science and Nutrition, 52(9): 830–851. https://doi.org/10.1080/10408398.2012.667460

Peñaflor LM, Elepaño AR and Peralta EK. 2014. Rice-like grains from broken rice *(Oryza sativa L.)* and adlai (Coix lacryma-jobi L.). Asian Journal of Agriculture and Food Science, 02(04): 2321–1571.

Prakash B and Pan Z. 2011. Modeling Moisture Movement in Rice. Advanced Topics in Mass Transfer. InTech, Rijeka, Croatia, pp. 283-304.

Sun DW. 2007. CFD Modeling of Simultaneous Heat and Mass Transfer in Beef Chilling. Computational Fluid Dynamics in Food Processing. CRC Press, Taylor & Francis Group, Boca Raton, Florida, USA, pp. 195-221.

Sun DW. 2019. Non-Conjugated Drying Models. Computational Fluid Dynamics in Food Processing Second Edition. CRC Press, Taylor & Francis Group, Boca Raton, Florida, USA, pp. 342-344.

The Engineering ToolBox. 2018. Air - Diffusion Coefficients of Gases in Excess of Air. https://www.engineeringtoolbox.com Accessed on 13 January 2021.

ROLE OF AUTHORS: *AMA – main author, concept, numerical modeling, data gathering, data analysis, manuscript writing; ARE – thesis adviser, concept, consultations, revising of manuscript; KFY – consultations, revising of manuscript; DCS – consultations, revising of manuscript.*

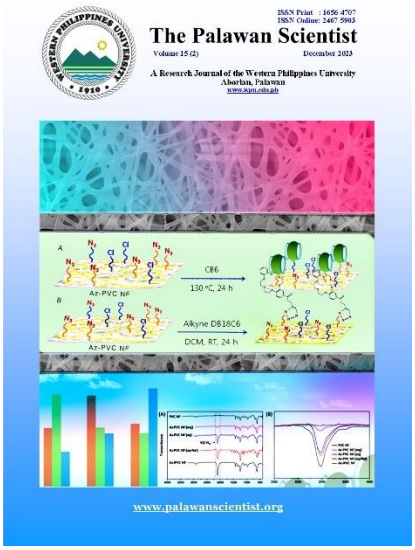

Seismic-induced landslide hazard analysis of the recreational area of the Makiling Botanic Gardens, Los Baños, Laguna, Philippines

Angelo Manuel A. Castillo*, Jedidiah Joel C. Aguirre, Carmina B. Borja and Andre C. Cruz

University of the Philippines Los Baños, Los Baños, Laguna, Philippines
**Correspondence: aacastillo3@up.edu.ph*

Received: 01 May 2023 || Revised: 16 Oct. 2023 || Accepted: 04 Dec. 2023

ISSN: 1656-4707
E-ISSN: 2467-5903
Homepage: www.palawanscientist.org

How to cite:
Castillo AMA, Aguirre JJC, Borja CB and Cruz AC. 2023. Seismic-induced landslide hazard analysis of the recreational area of the Makiling Botanic Gardens, Los Baños, Laguna, Philippines. The Palawan Scientist, 15(2): 69-84.

ABSTRACT

The Makiling Botanic Gardens (MBG) is an educational and eco-tourism site located within the vicinity of Mount Makiling, a dormant volcano susceptible to landslides, and located less than 20 km away from at least two tectonic faults. The study assessed the seismic-induced landslide hazards in the recreational area of MBG mainly based on three parameters: factor of safety (FS), yield acceleration (a_y), and slope displacement (D_n). Dynamic Cone Penetration Test (DCPT) served as the primary method for obtaining the shear strength of the soil within the area. Meanwhile, other relevant parameters, including material unit weight and internal angle of friction, were determined through laboratory testing, correlations, and available data and models. Moreover, the Peak Ground Acceleration (PGA) and Spectral Acceleration (SA) values were obtained through an interpretation of a probabilistic seismic hazard analysis (PSHA) study of the Philippines. Using the ArcGIS software, an FS map, yield acceleration map, and slope displacement map were generated. Results showed that the slopes within the area exhibit static stability. However, in the event of an earthquake, it is expected that the amplified PGA will exceed the expected yield acceleration values of the slopes in some parts of the recreational area, which could result in dynamic instability and slope displacements as high as 130 mm. Thus, the recreational area of MBG possesses some susceptibility towards a seismic-induced landslide.

Keywords: dynamic cone penetration test, factor of safety, Newmark displacement, peak ground acceleration, spectral acceleration

INTRODUCTION

Landslides are natural hazards generally defined as the downhill movement of soil, rock, and debris on sloping and relatively flat areas such as mountainous regions. They may occur without warning and may be triggered by earthquakes, heavy rainfall, and other activities that can disrupt and displace a mass of soil and rock which are everyday events in the Philippines, especially in its mountainous regions (Lapitan et al. 2006). Mount Makiling, a dormant but potentially active volcano in the Philippines with an elevation of 1,090 m above mean sea level, is a mountainous region housing several constituents of the Los Baños municipality (KBA 2006). Moreover, according to the ASEAN Centre for

Biodiversity (2013), within Mount Makiling lies the Mount Makiling Forest Reserve (MMFR), which houses the Makiling Botanic Gardens (MBG), established under Republic Act 3523 and Makiling Center for Mountain Ecosystems (MCME), to serve as an educational and eco-tourism site for the public. However, MBG also houses several sloping areas of soil and rock that may or may not be susceptible to seismic-induced landslides. According to the Philippine Institute of Volcanology and Seismology (PHIVOLCS), as of 2013, the MMFR is located approximately 17 km away from the nearest Valley Fault System (VFS), in which the fault system extends to the municipality of Calamba. Thus, to help establish proactive measures against a possible future destructive event, a seismic hazard analysis and mapping may be deemed necessary.

Seismic hazard is a classification of hazards that refer to the statistical probability of the occurrence of seismic activities, such as earthquakes, within a geographical area (Rojas 2016). In this regard, seismic-induced landslides may occur at any point in time, considering that there is still lack of technology and data for accurate predictions of earthquake occurrence. Concerning seismic activities, peak ground acceleration (PGA) is the maximum change in speed experienced by a particle in the ground. In contrast, spectral acceleration (SA) is the change in speed experienced by an infrastructure (Bradley 2011). Both PGA and SA may be expressed in *g* or the standard acceleration value due to gravity (9.81 $m \cdot s^{-2}$). Additionally, PGA may serve as a hazard index for short buildings with a maximum of seven stories, on average, in which PGA focuses more on peak ground motion. Meanwhile, SA may serve as a hazard index for tall buildings in which SA focuses more on building behavior. Furthermore, a probabilistic seismic hazard model of the Philippines was generated by the study of Peñarubia et al. (2020). In the study, the Philippine archipelago is defined as tectonically complex and seismically hazardous due to its geographical position and its formations. In the study, a PGA map was generated for the Philippines with a 10% probability of exceedance in a period of 50 years, as shown in Figure 1. For the municipality of Los Baños in the province of Laguna, the PGA for the area ranges from 0.3 *g* to 0.5 *g***.** In the case of MBG, a protected sanctuary, a non-intrusive seismic hazard analysis method was preferred to conform with related laws and official memorandums.

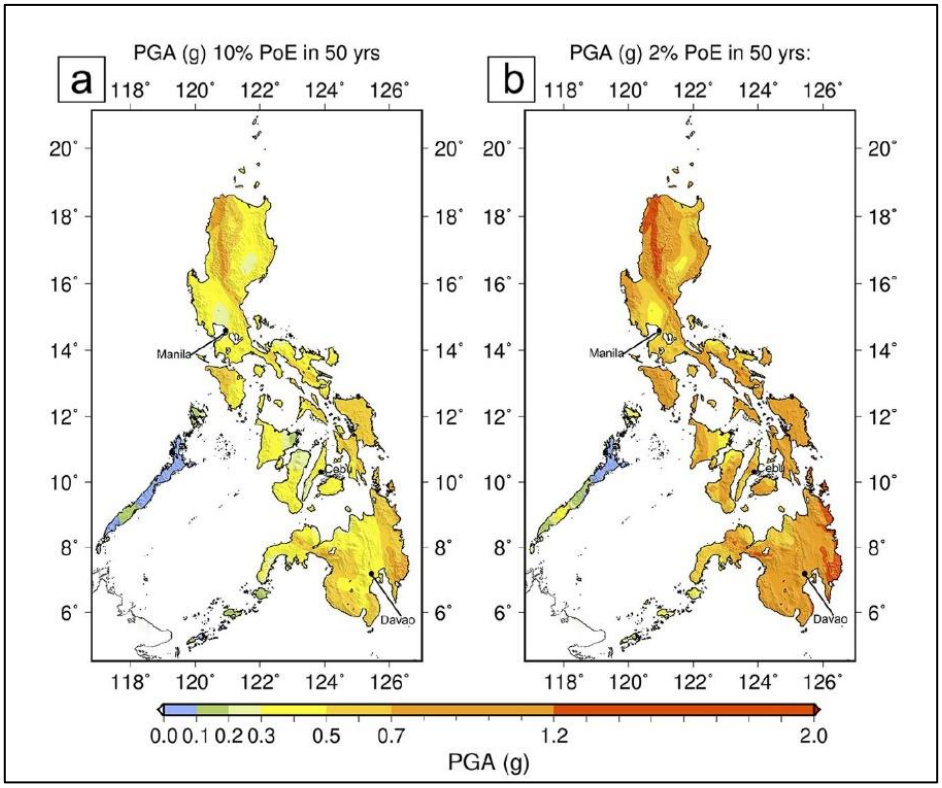

Figure 1. Mean peak ground acceleration (PGA)map for the Philippines with 10% and 2% probability of exceedance in 50 years.

The Dynamic Cone Penetration Test (DCPT) is a non-intrusive and non-destructive soil investigation procedure performed to determine the strength of the soil and soil layers present within the study area through the Dynamic Cone Penetration (DCP) – n values (VerTek 2021). In a seismic-induced landslide study in Indonesia by Kiyota (2020), DCPT provides an inexpensive and portable procedure for obtaining in-situ soil data regardless of slope stability conditions. The method is even more crucial in obtaining soil data after the events of a landslide in which slopes are unstable. The DCPT is performed following the standards provided by the ASTM D6951. According to Look (2007), the DCP is equivalent to a third of the energy of the Standard Penetration Test (SPT) in which the DCP – n values can be correlated with the soil strength in terms of cohesion, as shown in Table 1. The DCPT may be used for obtaining soil behavior data without procuring soil samples and disturbing the stratigraphy of a protected site such as MBG.

Since the Makiling Botanic Gardens (MBG), especially the recreational area, is a tourist destination and attracts several visitors annually, it would be beneficial for the area to have established safety measures against seismic-induced landslides, especially considering the unpredictable nature of earthquakes. The main objective of this study is to assess the seismic-induced landslide hazards in the 3.5 ha recreational area of the MBG based solely on projected seismic-induced slope displacements. Specifically, it aimed to identify the geology and soil composition within the recreational area of MBG based on available soil investigation reports and data; calculate the static Factor of Safety (FS) and yield acceleration at different points and areas within the recreational area of MBG using computed and pre-determined relevant soil parameters; and calculate the slope displacements due to seismic-induced landslides at different points and areas within the recreational area of MBG.

Table 1. Strength parameters from DCPT Data. Source: Look 2007.

Material	Description	DCP – n (Blows/100 mm)	Strength
Clays	Very Soft	0-1	C_u = 0-12 kPa
	Soft	1-2	C_u = 12-25 kPa
	Firm	2-3	C_u = 25-50 kPa
	Stiff	3-7	C_u = 50-100 kPa
	Very Stiff	7-12	C_u = 100-200 kPa
	Hard	>12	C_u > 200 kPa
Sands	Very Loose	0-1	$\Phi < 30°$
	Loose	1-3	Φ = 30-35°
	Medium Dense	3-8	Φ = 35-40°
	Dense	8-15	Φ = 40-45°
	Very Dense	>15	$\Phi > 45°$
Gravels, Cobbles, Boulders		>10	$\Phi = 35°$
		>20	$\Phi > 40°$
Rock		>10	C' = 25 kPa, $\Phi > 30°$
		>20	C' = 50 kPa, $\Phi > 30°$

METHODS

Descriptive Summary of the Study Area

The study focused only on the 3.5 ha recreational area of MBG, (Figure 2). The area was plotted using WGS84 coordinates and described using maps regarding the local geology and tectonic setting of the MMFR. The MBG has a WGS84 coordinates of 14.1566° North and 121.2342° East. For the procurement of existing pertinent data regarding the geomorphological characterization of MBG, the following documents were requested and obtained from the Makiling Center for Mountain Ecosystems (MCME): Land cover map of the MMFR ASEAN Heritage Park, Soil cover map of the MMFR ASEAN Heritage Park, and DEM of the MMFR ASEAN Heritage Park. Through ArcGIS, the elevation map at 5 m intervals, slope angle map at 5° intervals, land cover map, and soil cover map for the 3.5 ha study area were extracted.

Figure 2. Plot and location of study area.

Determination of Soil Properties

The Dynamic Cone Penetration Test (DCPT) served as the primary procedure for obtaining primary data to determine needed soil parameters. For the 3.5 ha recreational area, 43 test points were determined and plotted to represent the study area, as shown in Figure 3. For each test point, DCPT was performed once in which an 8 kg hammer was repeatedly raised and dropped at a certain height until it reached either a depth of one meter or refusal.

The penetration depth and number of blows were recorded for each test point. Afterwards, the Dynamic Cone Penetration (DCP) Index and DCP n-values for each test point were determined based on the penetration depth at each blow, resulting in generating a DCP profile for each test point. Using Table 1, the DCP – n values were correlated with cohesion (c') values. Due to the presence of clayey soil within the study area and as per Table 1, only cohesion values can be correlated with DCP-n values. For conservative measures, the lowest cohesion value obtained within a test point served as the governing shear strength for that test point. Then, the shear strength values were interpolated using the Kriging method of ArcGIS to generate a shear strength map for the study area. Meanwhile, slope angles (α) were determined based on the generated slope angle map for the same area.

Laboratory Determination of Other Soil Properties

For each of the 43 test points within the 3.5 ha recreational area of MBG, soil samples with respective masses of at least 100 g were obtained for laboratory testing at the Department of Civil Engineering (DCE) in the University of the Philippines Los Baños (UPLB). In the laboratory, the procured soil samples were oven-dried for at least 24 h, pulverized with a hammer, and sieved using Sieve No. 200 and mechanical shaker for 3 min.

After sieving, the mass retained in Sieve No. 200 was measured and recorded. Then, the percentage composition of the recorded mass to the overall mass of the sieved soil was computed and determined. The said parameter served as the coarse percentage of the soil sample, indicating the percentage of the sample with a particle diameter of more than 75 μm. If the

coarse percentage of a sample yielded a value of at least 30%, the internal angle of friction ($\emptyset'$) was determined through correlation with cohesion values using Table 2.

Meanwhile, for the determination of the material unit weight of the soil (γ), a small cylindrical container was prepared and filled with a compacted sample. The material unit weight was then computed and determined based on the contained mass of the container (in kilograms) and the inner volume of the container (in cubic meters) using Table 3.

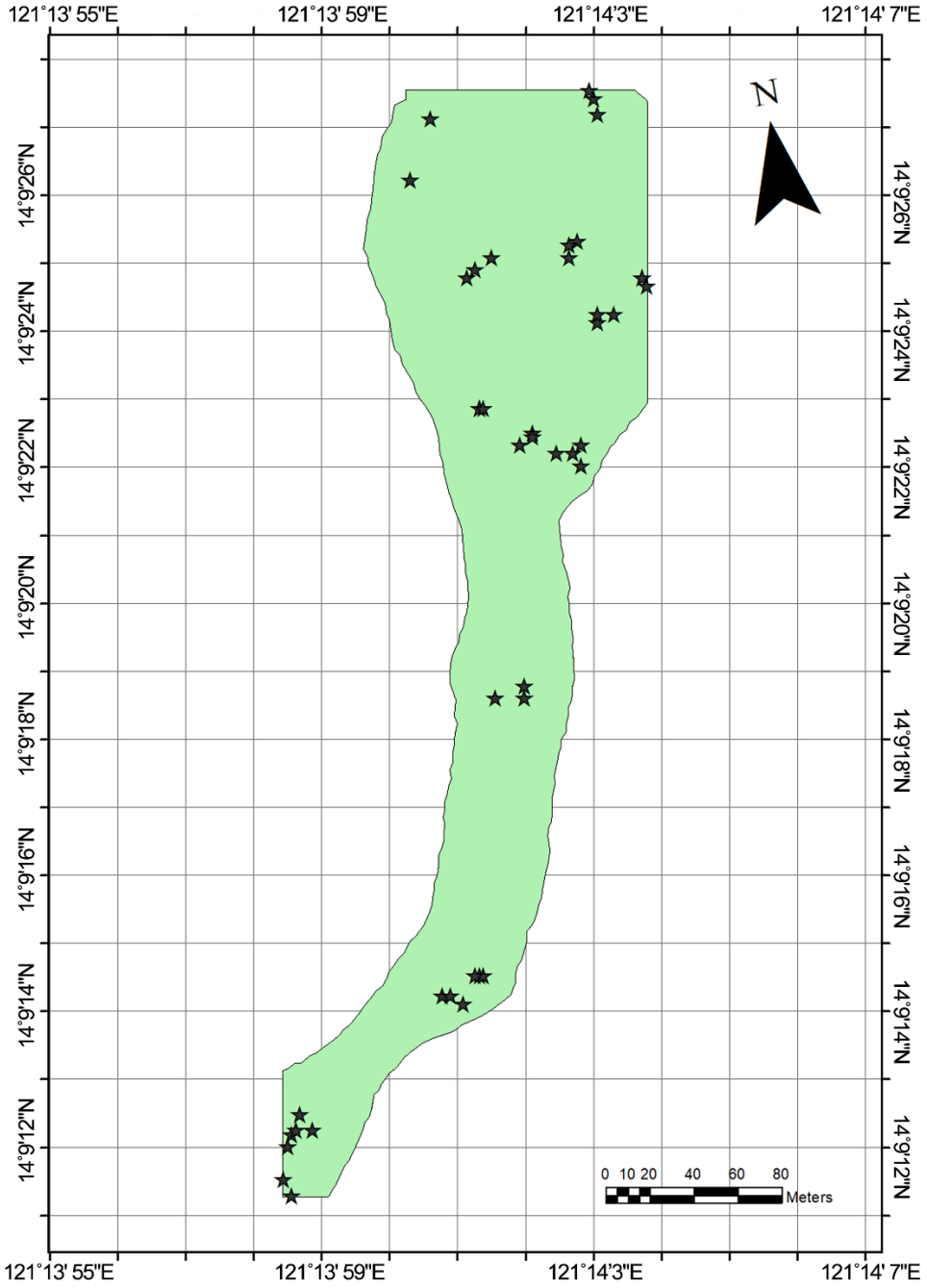

Figure 3. Map of the 3.5-hectare recreational area of Makiling Botanic Gardens showing the sampling sites (★).

Table 2. Strength values for cohesive soil. Source: Look 2007.

Type	Description	Effective Cohesion (kPa)	Friction angle (degrees)
Cohesive	Soft- Organic	5-10	10-20
	Soft- Non-organic	10-20	15-25
	Stiff	20-50	20-30
	Hard	50-100	25-30

Table 3. Corresponding material unit weight values for DCP – n values. Source: Herath 2005.

γ (kN m^{-3})	**DCP – n value (mm/blow)**
15.3	18.4
17.1	15.0
17.8	17.0
18.9	16.7
17.6	22.5
18.7	13.0
16.8	23.0
15.8	36.0
16.1	18.8
16.7	29.0
16.3	26.1
16.1	27.0
14.1	13.5
14.1	15.2
13.1	15.0
18.2	14.3
17.0	17.2
15.5	6.54
18.4	15.9
18.0	11.7
18.6	23.3
16.8	63.7
17.3	10.6
18.4	26.0

Determination of Factor of Safety

The Factor of Safety (FS) serves as a measure of slope stability within an area of interest. It is the ratio between the available shear strength of a slope and the shear forces acting on the slope that may cause landslides. Generally, an FS of greater than unity indicates a stable slope, while an FS of less than unity indicates an unstable slope prone to slope failure (Kramer 1996). The previously generated land cover map, soil cover map, slope angle map, elevation map, and shear strength map for the study area were intersected together with a set of 10 m by 10 m grids. Afterward, the newly generated map divided the recreational area of MBG into cells in which each cell had a corresponding set of attributes. Using the said attributes, the FS at each cell of the recreational area of MBG was determined using Equation 1, as shown below:

$$FS = \frac{c\prime}{\gamma t sin(\alpha)} + \frac{tan\emptyset\prime}{\tan(\alpha)} \quad (1)$$

where:

FS is the static factor of safety;
c' is the effective soil cohesion;
γ is the material unit weight of the soil;
t is the slope-normal thickness of the failure slab (3 m for shallow landslides;
α is the slope angle; and
$\emptyset'$ is the internal angle of friction of the slope.

The resulting values for the FS at each cell of the study area served as the basis for generating an FS map for the said area. The generated map provided a general overview of the static slope stability of the recreational area of MBG regarding the FS.

Yield Acceleration

In Newmark's sliding block analysis, both static and dynamic forces are incorporated to analyze slope stability, which is indicated by the yield acceleration (a_y). The yield acceleration is the minimum pseudo-static acceleration that can induce slope instability. Moreover, a mass that reaches its yield acceleration results in an FS of unity, implying that areas with yield acceleration values less than the peak ground acceleration (PGA) are susceptible to seismic-induced landslides. Regarding the FS map of the study area, the yield acceleration values, expressed in $\boldsymbol{g}$, at each cell were determined using Equation 2, as shown below:

$$a_y = (FS - 1)\, sin(\alpha) \quad (2)$$

where:

a_y is the yield acceleration of the slope;
FS is the factor of safety of the slope;
α is the slope angle.

After determining the corresponding yield acceleration values for each cell of the study area, a yield acceleration map for the recreational area of MBG was generated, thus providing an overview of the susceptibility of MBG towards landslides in terms of induced accelerations.

Determination of Slope Displacement

As mentioned previously, yield acceleration is the minimum value of acceleration to cause slope

instability. Slope failures, such as landslides, result in permanent displacements. The Newmark method for measuring displacement considers the effects of dynamic forces due to seismic activities. For this study, the pseudo-empirical predictive formula for Newmark displacements derived by Veylon et al. (2017) was used, as shown in Equation 3. For the values of PGA and spectral acceleration (SA) of the study area, the study adopted the maximum average PGA, with a 475 yr return period, for the study area which was from the study of Peñarubia et al. (2020). Furthermore, the adopted PGA value was amplified based on the specifications of the American Society of Civil Engineers (ASCE) Section 7-05 and based on the site classification of the study area. Meanwhile, the recreational area of MBG was generated based also on ASCE Section 7-05, a spectral acceleration design response spectrum, with a 475 yr return period. Lastly, the corresponding SA values at each cell of the study area was based from the Spectral Acceleration Maps provided by DOST-PHIVOLCS (Figures 4 and 5).

$$\ln(D_n) = -0.56 - 2.23\frac{a_y}{PGA} + 2.8\ln(\frac{SA(1.5T_1)}{PGA}) \quad (3)$$

where:

D_n is the Newmark displacement;
a_y is the yield acceleration;
g is the acceleration under the effects of gravitational force;
PGA is the peak ground acceleration;
SA is the spectral acceleration; and
T_1 is the initial fundamental period of the structure.

T_1 measures the vibratory characteristics of the slopes, which can be associated with the height of the slope and its stiffness. Thus, T_1 was determined using the formula from Veylon et al. (2017), shown in Equation 4 below:

$$T_1 = \frac{2\pi}{2.4}\frac{H}{\sqrt{G_{max}/\rho}} \quad (4)$$

where:

H is the height of the slope;
G_{max} is the maximum shear modulus of the material; and
ρ is the density of the material of the slope.

After determining the projected slope displacements at each cell of the recreational area of MBG, a slope displacement map was generated using ArcGIS. The map provided estimates of permanent displacements at different points and areas of the 3.5 ha recreational area of MBG in the event of a seismic-induced landslide occurrence.

RESULTS

Geology and Soil Composition of the Recreational Area of the Makiling Botanic Gardens

Makiling Botanic Gardens (MBG) is an eco-tourism site within the Mount Makiling Forest Reserve (MMFR) ASEAN Heritage Park. Figure 6 shows the local geology of the MMFR ASEAN Heritage Park, which defines the lithology and structures present within the area. To further support the implications of the local geology of the MMFR ASEAN Heritage Park, the presence of a particular type of soil suitable for plant growth and development was considered since the recreational area of MBG contains a diverse range of flora and fauna. For general visualization of the soil composition of the study area, Figure 7 shows the soil cover map for the recreational area of MBG, which was extracted from MMFR ASEAN Heritage Park soil cover map provided by the Makiling Center for Mountain Ecosystems (MCME). Concerning the soil cover map of the study area, Figure 8 shows the land cover map for the same area extracted from the provided MMFR ASEAN Heritage Park land cover map by MCME.

A Digital Elevation Model (DEM) from the National Mapping and Resource Information Authority (NAMRIA 2015) for the MMFR ASEAN Heritage Park was provided by MCME, which served as the basis for mapping the elevations and slope angles of the study area in which Figures 9 and 10 show the varying elevations and slope angles present within the area, respectively. At each of the 43 test points, a Dynamic Cone Penetration Test (DCPT) was performed, in which each test point generated a Dynamic Cone Penetration (DCP) n-value profile

(Figure 3). Then, the obtained DCP n-value profile was correlated to shear strength values (Table 1). The shear strength values at each point were then correlated to generate a shear strength map for the study area (Figure 11).

Static Factor of Safety and Yield Acceleration

Through ArcGIS, all the previously generated maps were combined and intersected. Fishnets were established using 10 m by 10 m grids, resulting in a generated map with 1,388 individual cells with their own unique sets of attributes. The static FS of each of the 1,388 cells was determined using Equation 1 and added as an attribute, resulting in an FS map shown in Figure 12. After determining the FS values at each cell and using Equation 2, the yield acceleration values for each of the 1,388 cells of the plotted recreational area of MBG were determined and added as an attribute, resulting in a yield acceleration map (see Figure 13).

Seismic-induced Slope Displacements

For the determination of projected slope displacements due to seismic-induced landslides, the peak ground acceleration (PGA) and spectral acceleration (SA), with a 475-year return period, for the recreational area of MBG were determined and considered. Considering the amplified PGA for the recreational area, a conservative value of 0.85***g*** was considered for the PGA of the said area. Meanwhile, using the generated site-specific spectral acceleration design response spectrum for the same area, each of the 1,388 cells of the study area was assigned a spectral acceleration value based on the fundamental period computed for each cell using Equation 4. Finally, using Equation 3, the slope displacement for each cell was determined and assigned as an attribute, resulting in the slope displacement map (see Figure 14).

DISCUSSION

Geology and Soil Composition of the Recreational Area of the Makiling Botanic Gardens

The local geology of the MMFR ASEAN Heritage Park is composed mainly of volcanic materials and residues based on Figure 6. The subsurface material present within the area is part of the Macolod Volcanic Complex, which is composed of volcanoes and volcanic features originating from the Pliocene era (5.3 mya) to the Pleistocene era (11 mya) in which Mount Makiling is part of the said complex (Peña 2008). Moreover, due to the active volcanic processes circulating within the area, tectonic features are influenced by these processes, resulting in a volcanotectonic fault located around 10 km east of the campus of the University of the Philippines Los Baños (UPLB). Additionally, the soil composition for the recreational area of MBG is mainly Macolod clay, a loam-clay soil (Figure 7) which is a common variety of soil in the Philippines that is suitable for agricultural purposes due to its high nutrient value and water retaining capacity (Montecillo 1983). However, Macolod clay is a relatively soft soil, which may indicate an increased risk for seismic-induced landslides. Additionally, the majority of the recreational area of MBG is built-up, implying the presence of structures such as roads, pavements, and buildings (Figure 8). The presence of these structures may further indicate that slope stabilization measures within the vicinity of the structures have been established and implemented. According to the California State of Water Resources Control Board (2001), slope stabilization measures are established in sloping areas prone to surface runoff and erosion, such as Mount Makiling. The presence of several infrastructures in such an environment may imply that stabilization measures were established to increase the slope's factor of safety and to stabilize the soil. However, based on existing records and observations, some portions of the built-up areas have exhibited signs of degradation due to age and environmental factors. Such a case may further result in outdated structures with unstable frameworks, which may serve as a factor for increased disaster risk in the event of seismic-induced landslides.

Regarding elevations in the study area, the recreational area of MBG exhibits increasing elevation from the entrance (northeast portion of the area) to the *Dipterocarp* area (southern portion of the area) (see Figure 9). The area yielded a maximum elevation of 140 m above mean sea level and a minimum elevation of 85 m above mean sea level, resulting in a maximum slope height of approximately 55 m. Moreover, the immediate changes in elevation in the *Dipterocarp* area and Molawin Creek area (northwest portion of the area) indicate the presence of relatively steep slopes within the said areas. Furthermore, the slope angles within the recreational area range from a minimum angle of 0° to a maximum angle of 20° (Figure 10). This indicates that the highest slope angles of the recreational area are present within the Molawin Creek area (Figure 9). The slope angles were one of the main parameters of interest to determine the static Factor of Safety (FS) values within the recreational area. Lastly, the shear strength of the Macolod clay within the recreational area of MBG ranges from a minimum shear strength of 12 kPa to a maximum shear strength of 26 kPa (Figure 11).

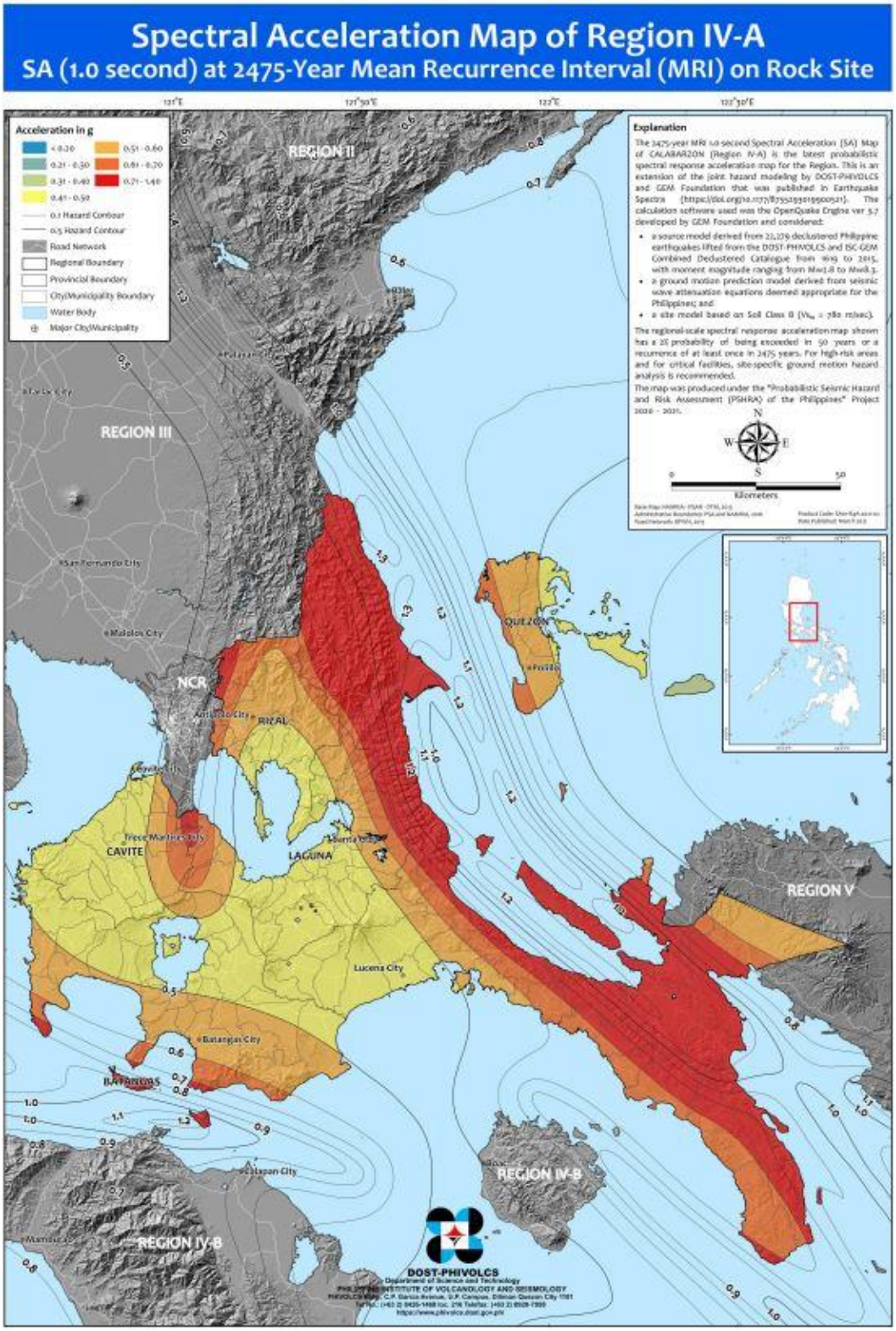

Figure 4. Spectral acceleration map of Region IV-A at 1.0 second.

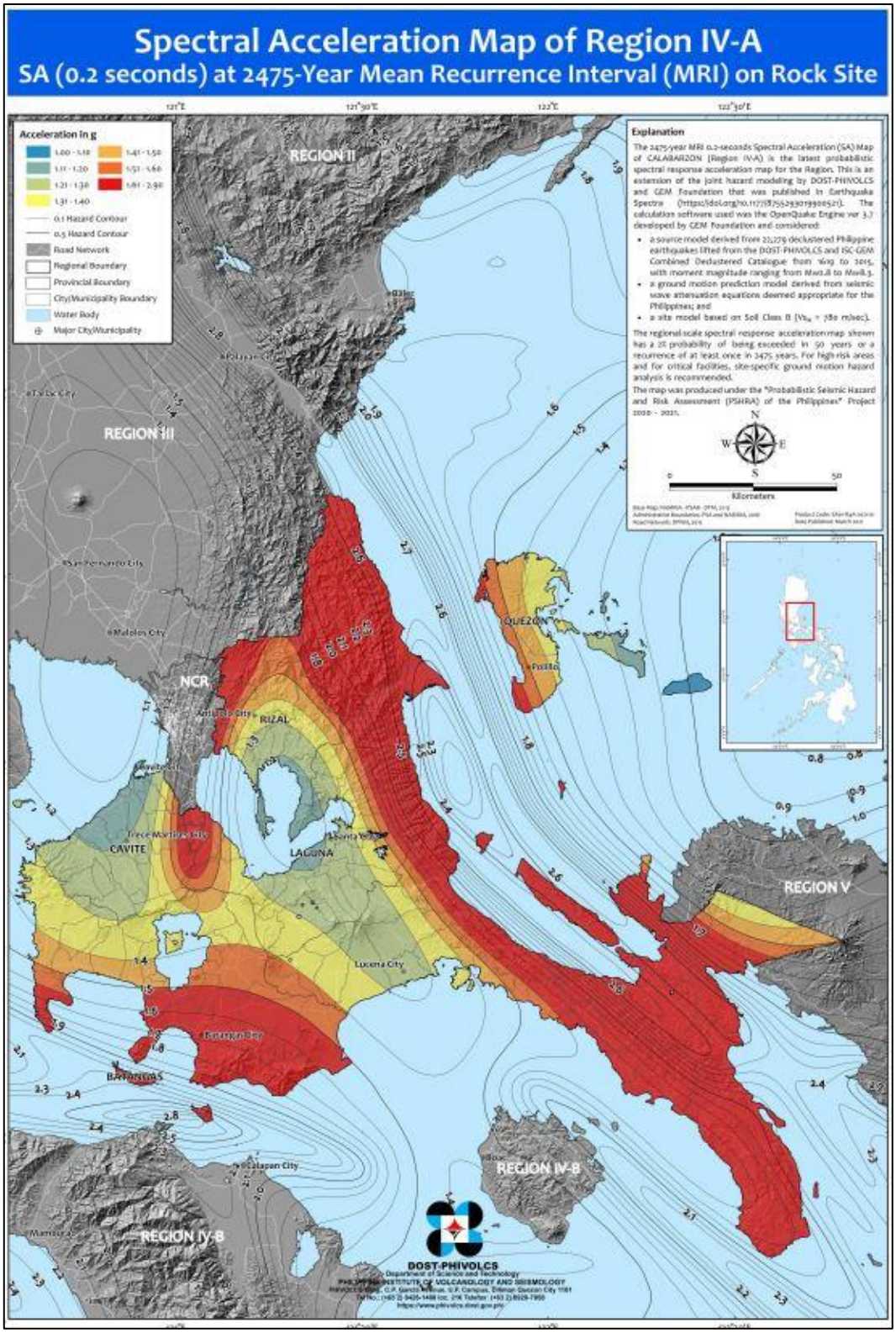

Figure 5. Spectral acceleration map of Region IV-A at 0.2 second.

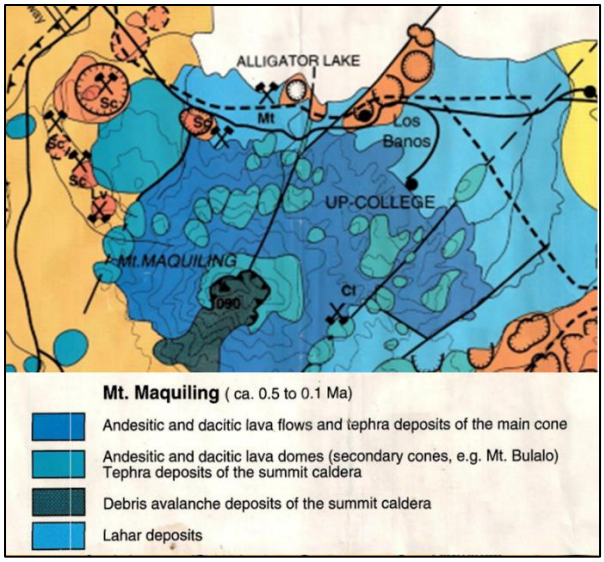

Figure 6. Local geology of Mount Makiling Forest Reserve ASEAN Heritage Park.

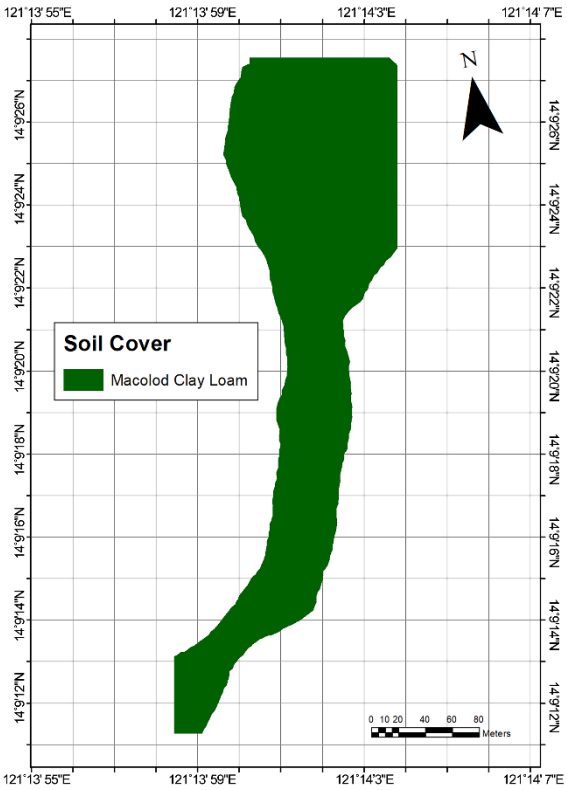

Figure 7. Soil cover map of the recreational area of Makiling Botanic Gardens.

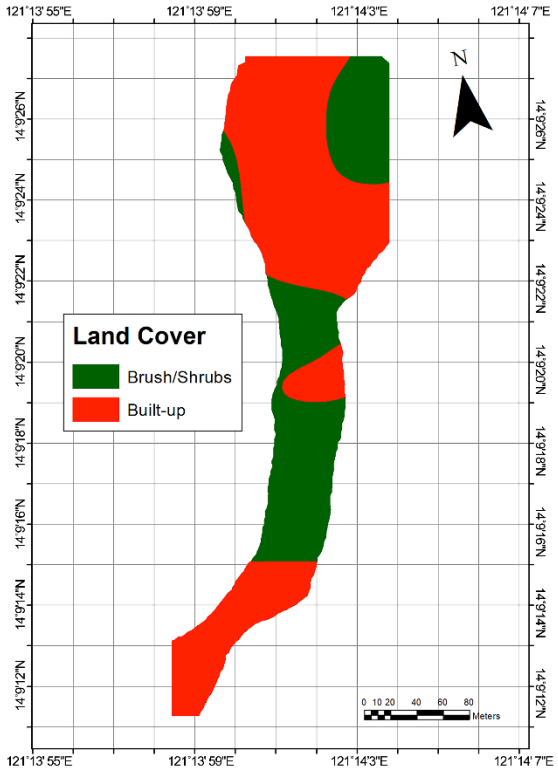

Figure 8. Land cover map of the recreational area of Makiling Botanic Gardens.

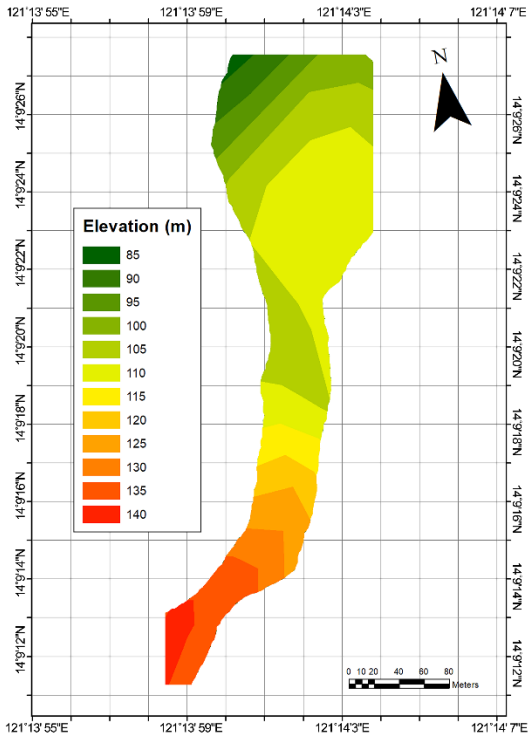

Figure 9. Elevation map of the recreational area of Makiling Botanic Gardens.

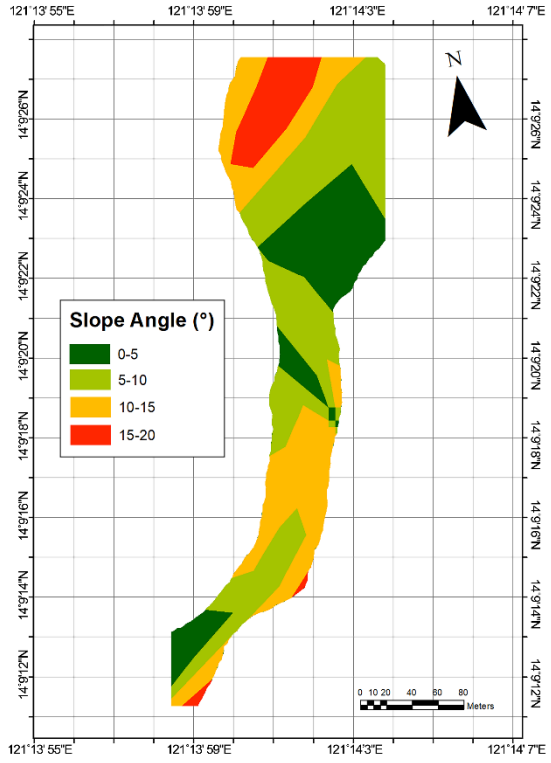

Figure 10. Slope angle map of the recreational area of Makiling Botanic Gardens.

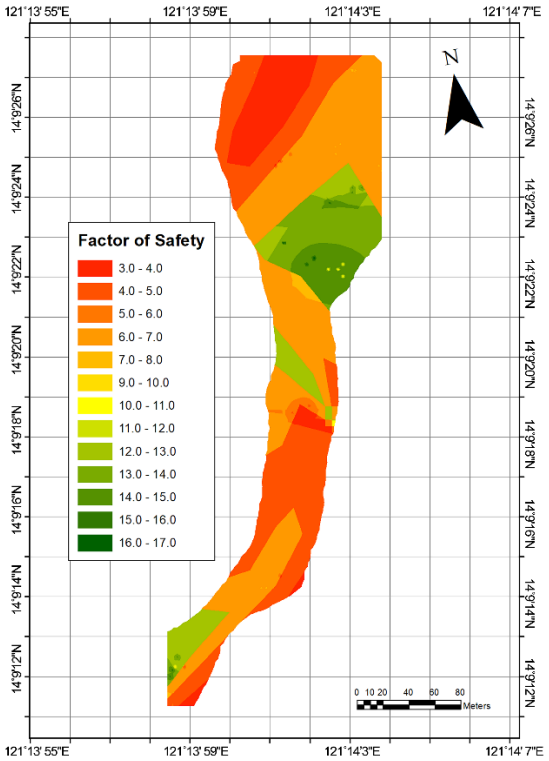

Figure 12. Factor of safety map for the recreational area of Makiling Botanic Gardens.

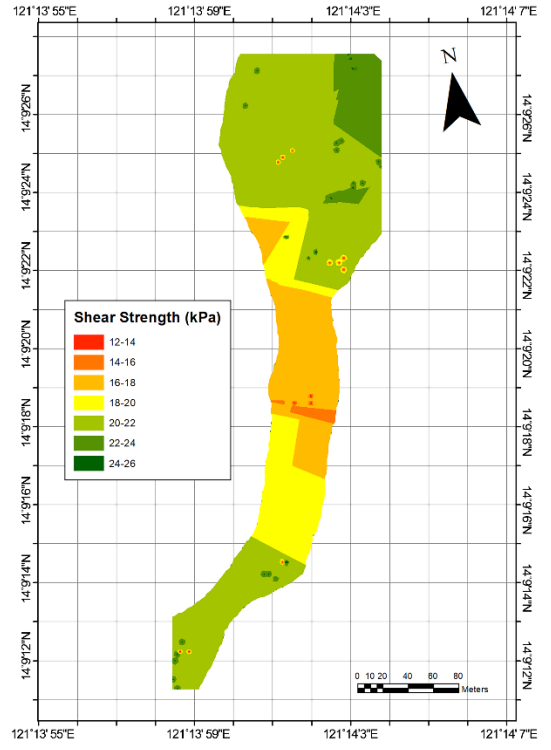

Figure 11. Shear strength map of the recreational area of Makiling Botanic Gardens.

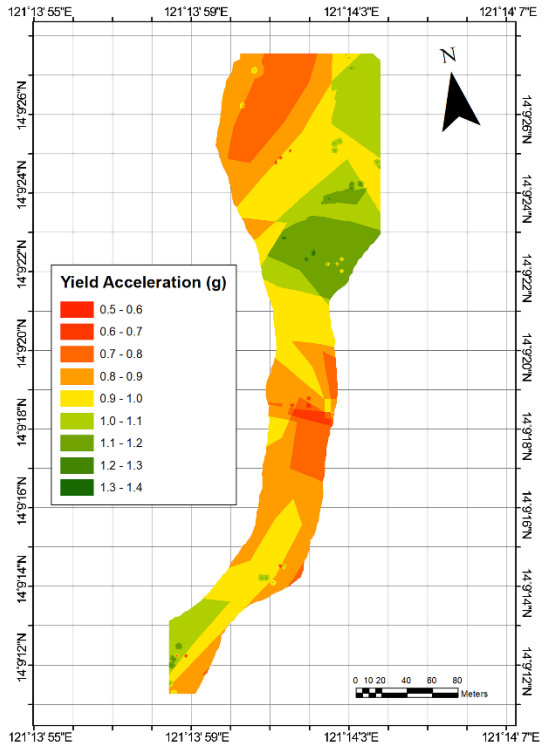

Figure 13. Yield acceleration map of recreational area of Makiling Botanic Gardens.

Relatively, low shear strength is observed in the central portion of the area, while relatively high shear strength is observed in the northern and southern portions of the area. Like the slope angles, the shear strength values served as one of the main parameters of interest to determine the static FS values within the recreational area. Additionally, due to the lack of Standard Penetration Test (SPT) data within the recreational area of MBG, the shear strength map served as the basis for the site classification of the study area. According to Atkinson (2008), shear strength values of less than 20 kPa and between 20 kPa and 40 kPa indicate the presence of very soft soil and soft soil, respectively. Based on Table 4, site classification E corresponds to an area with a soft soil profile. Thus, the 3.5 ha recreational area of MBG has a site classification of E due to soft soil (Figure 11). The site classification served as a basis for adjusting seismic parameters in the seismic-induced landslide hazard analysis of the said area.

Table 4. Soil profile types. Source: National Structural Code of the Philippines 2015.

Soil Profile Type	Generic Description	Average Soil Properties for Top 30 m of Soil Profile		
		Shear Wave Velocity, Vs ($m \cdot s^{-1}$)	SPT, N (blows/ 300 mm)	Undrained Shear Strength, S_u (kPa)
S_A	Hard Rock	> 1500		
S_B	Rock	760 to 1500		
S_C	Very Dense Soil and Soft Rock	360 to 760	> 50	> 100
S_D	Stiff Soil Profile	180 to 360	15 to 50	50 to 100
S_E[1]	Soft Soil Profile	< 180	< 15	< 50
S_F	Soil Requiring Site-specific Evaluation			

Static Factor of Safety and Yield Acceleration

The entirety of the recreational area of MBG has a static FS of more than 1.5, implying that the area has safe and stable slopes on average since all FS values are higher than unity based on Figure 12. These values further indicate that the resisting forces in the soil and slopes are sufficient to resist the shear forces acting within the soil. Additionally, a conservative value of 1.5 for the FS is generally acceptable as the basis for the design of a stable slope (Das 2010). An FS of less than 1.5 or close to unity may imply that the slope is close to failure with additional loads. Moreover, an FS of precisely unity indicates slope failure when the applied load reaches the design load. At the same time, an FS of less than unity indicates slope failure even without the application of loads. Since the FS of the recreational area of MBG yielded a value of more than 1.5, the area is suitable for some infrastructure developments since loading and environmental conditions are not severe (Maria 2016). Specifically, the minimum FS value yielded by the recreational area is around 3.02, in the Molawin Creek area and some portions of the *Dipterocarp* area. The relatively low FS value yields are consistent with the previously observed trends within the same areas. This implies that these areas have relatively very steep slopes (Figure 9) with large slope angles, which are both factors that affect slope stability. A steeper slope or a higher slope angle would result in a decrease in slope stability, which further increases its susceptibility to landslide occurrence due to the increasing effects of gravity as the plane becomes more inclined with respect to the horizontal plane. The remaining areas of the recreational area of MBG have relatively flat slopes with small slope angles, resulting in relatively very high FS values compared to the Molawin Creek area and the *Dipterocarp* area. Nevertheless, due to a high FS of 3.02, the Molawin Creek and *Dipterocap* areas have safe and stable static slopes.

Meanwhile, the entirety of the recreational area has a yield acceleration value ranging from 0.5 *g* to 1.4 *g* (Figure 13). The obtained value indicates that a minimum pseudo-static acceleration equal to the acceleration due to gravity multiplied by a factor of 0.5 must be induced to cause slope instability and landslide occurrence in some portions of the recreational area. Furthermore, the Molawin Creek and *Dipterocarp* areas yielded relatively low yield acceleration values, ranging only from 0.5 *g* to 0.8 *g* (Figure 12). These areas also yielded the lowest FS values, which served as the main factor for the differences in yield acceleration values at different areas of the recreational area of MBG. Based on the peak ground acceleration (PGA) maps of Peñarubia et al. (2020), the PGA for the area of Los Baños, Laguna, ranges from 0.3 *g* to 0.5 *g* considering a return period of 475 years. Following the American Society of Civil Engineers (ASCE) Section 7-05 and consideration of the site classification (E) of the recreational area, an amplification factor was applied to the PGA values, resulting in an amplified PGA for the recreational area of MBG, ranging from 0.70 *g* to 0.85 *g*. As a result, in the event of an earthquake, slope instabilities and

movements are highly likely to occur in the Molawin Creek area and *Dipterocarp* area since their respective yield acceleration values are less than or within the range of the amplified PGA for the recreational area of MBG.

Seismic-Induced Slope Displacements

Some portions of the recreational area have minimal projected slope displacements in the event of a seismic-induced landslide ranging only from 0 mm to 10 mm (Figure 14). However, some portions of the recreational area have large and significant slope displacements in the event of a seismic-induced landslide (Figures 12 and 13). Specifically, the Molawin Creek area and *Dipterocarp* area yielded the relatively highest projected slope displacements in the event of a seismic-induced landslide ranging from 80 mm to 130 mm. While the said areas have stable slopes in terms of static factors (Figure 12), the same areas have unstable slopes in terms of dynamic factors (Figure 13) resulting to significant seismic-induced slope displacement values. These dynamic factors generally consider the stability of the slopes against dynamic forces such as seismic-induced forces. Unfortunately, the Molawin Creek and *Dipterocarp* areas yielded relatively low resistance against these forces. As a result, in the event of an earthquake, the slopes within the Molawin Creek and *Dipterocarp* areas are high and likely to be significantly and progressively displaced which could lead to slope failures and seismic-induced landslides.

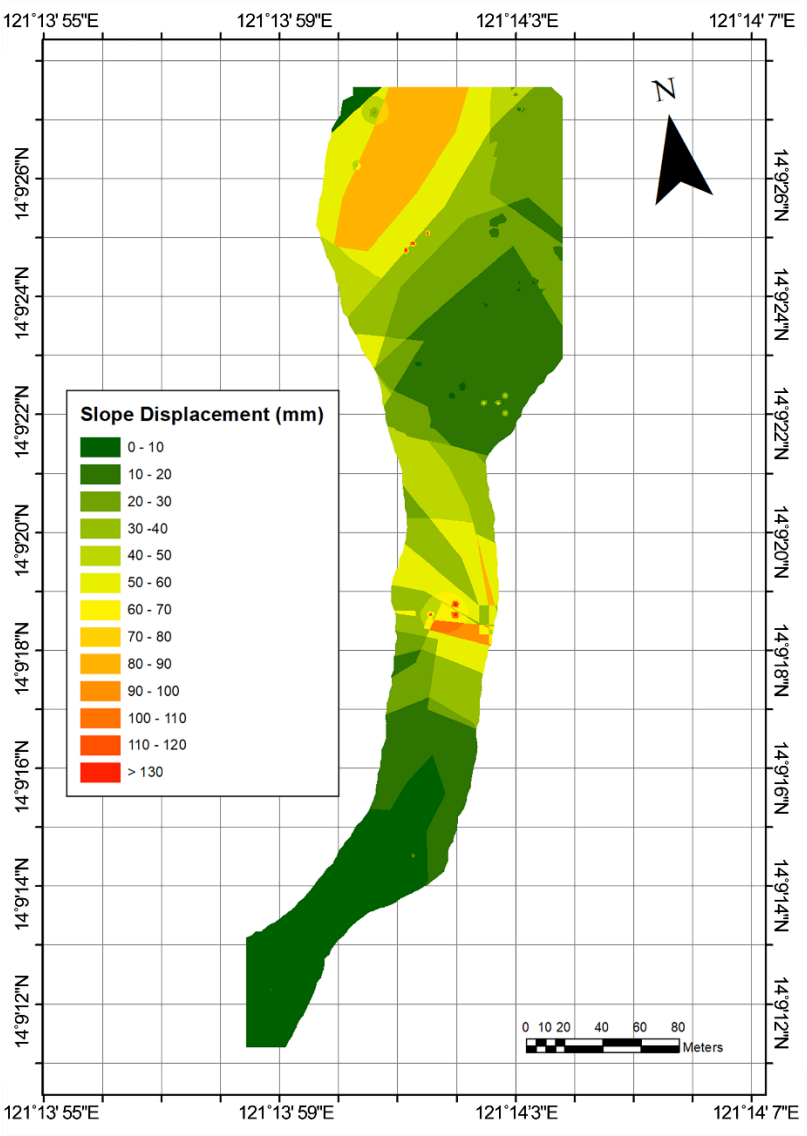

Figure 14. Slope displacement map of the recreational area of Makiling Botanic Gardens.

FUNDING

The study was primarily funded through the thesis grant provided by the Department of Science and Technology – Science Education Institute (DOST-SEI) Merit Scholarship.

ETHICAL CONSIDERATIONS

Test points used for landslide hazard analysis was safe and practical for researchers to avoid accidents and injuries. Studies conducted in a protected area employed non-intrusive and non-destructive methods to preserve the environment and ecosystem of the said area. Studies conducted during the COVID-19 pandemic observeed proper protocol and guidelines imposed by the agencies and institutions involved in the study.

DECLARATION OF COMPETING INTEREST

The authors declare that there are no competing interests to any authors.

ACKNOWLEDGMENTS

The authors would like to acknowledge For. Angela A. Limpiada for providing instructions and workshops in using ArcGIS and understanding its fundamentals. The authors would also like to acknowledge the Makiling Botanic Gardens (MBG), Makiling Center for Mountain Ecosystems (MCME), and their employees for approving the conduct of study in their areas and for providing support in the said study. The authors would also like to acknowledge the Department of Science and Technology – Science Education Institute (DOST-SEI) for providing financial support to the study. Additionally, the authors would like to acknowledge the Department of Civil Engineering and College of Engineering and Agro-Industrial Technology of the University of the Philippines Los Baños for their continuous support and guidance to the writing and finalization of the manuscript. Lastly, the authors would like to acknowledge the assigned reviewers of the manuscript for their patience and efforts towards improving the content and write-up of this paper and for making its publication possible.

REFERENCES

ASEAN Centre for Biodiversity. 2013. Mt Makiling Forest Reserve. https://asean.chm-cbd.net/mt-makiling-forest-reserve. Accessed on 26 September 2021.

Atkinson J. 2008. Rules of Thumb in Geotechnical Engineering. New Zealand Geotechnical Society: CY Chin, Auckland. 13pp.

Bradley BA. 2011. Empirical correlation of PGA, spectral accelerations and spectrum intensities from active shallow crustal earthquakes. Earthquake Engineering and Structural Dynamics, 40(15): 1707-1721. https://doi.org/10.1002/eqe.1110

California State of Water Resources Control Board. 2001. Slope Stabilization Techniques. California Waterboards. https://www.waterboards.ca.gov/lahontan/water_issues/programs/storm_water/docs/Chapter06.pdf. Accessed on 19 March 2022.

Das BM. 2010. Principles of Geotechnical Engineering (7th ed.). Cengage Learning. 666pp.

Herath A, Mohammad L, Gaspard K, Gudishala R and Abu-farsakh M. 2005. The Use of Dynamic Cone Penetrometer to Predict Resilient Modulus of Subgrade Soils. Geo-Frontiers Congress 2005. Austin: Amer Society of Civil Engineers. http://dx.doi.org/10.1061/40776(155)2

KBA (Key Biodiversity Areas). 2006. Mount Makiling, Philippines. https://www.keybiodiversityareas.org/site/factsheet/9722. Accessed on 19 September 2021.

Kiyota T, Furuichi H, Hidayat RF, Tada N and Nawir H. 2020. Overview of long-distance flow-slide caused by the 2018 Sulawesi earthquake, Indonesia. Soils and Foundations, 60(3): 722-735. https://doi.org/10.1016/j.sandf.2020.03.015

Kramer SL. 1996. Geotechnical Earthquake Engineering. New Jersey: Prentice Hall Inc, New Jersey. 653pp.

Lapitan PG, Sargento JO and Gaddi RT. 2006. Condition of the Mt. Makiling [Los Baños, Laguna, Philippines] after typhoon Milenyo and its restoration/rehabilitation plan. 2006 FORESPI Symposium: Forest Landscape Restoration an Rehabilitation [Symposium]. Food and Agriculture Organization of the United Nations, College, Laguna.

Look B. 2007. Handbook of Geotechnical Investigation and Design Tables. London: Taylor & Francis Group. 418pp. https://doi.org/10.1201/b16520

Maria R. 2016. Summary of Safety Criteria in Design. Universiti Malaysia Pahang, Malaysia: Automotive Engineering Research Group. http://dx.doi.org/10.13140/RG.2.1.1501.5285

Montecillo LC. 1983. Total Clay and Organic Matter in Relation to Soil Cation Exchange Capacity. Philippine Journal of Crop Science, 8: 41-44.

NAMRIA (National Mapping and Resource Information Authority). 2015. Department of Environment and Natural Resources. https://www.namria.gov.ph/download.php. Accessed on 10 January 2022.

National Structural Code of the Philippines. 2015. Static Force Procedure Section 208.5.4 (7th Edition). Quezon City: Association of Structural Engineers of the Philippines. 21pp.

Peña R. 2008. Lexicon of Philippine Stratigraphy. Geological Society of the Philippines, Mandaluyong City, Philippines. 364pp.

Peñarubia HC, Johnson KL, Styron RH, Bacolcol TC, Sevilla WG, Perez JS, Bonita JD, Narag IC, Solidum RU, Pagani MM and Allen T. 2020. Probabilistic seismic hazard analysis model for the Philippines. GEM's 2018 global hazard and risk models, 36(1_suppl): 44-68. https://doi.org/10.1177/8755293019900521

Rojas PM. 2016. Central ad South America: significant but constrained potential for geothermal power generation. Geothermal Power Generation, 667-715. https://doi.org/10.1016/B978-0-08-100337-4.00023-1

Vertek Team. 2021. What is DCP testing and how does it compare to CPT? https://www.vertekcpt.com/what-is-dcp-testing-and-how-does-it-compare-to-cpt/. Accessed on 19 September 2021.

Veylon G, Merckle S, Luu LH, Bard PY, Carvajal C and Frigo B. 2017. A simplified method for estimating Newmark. Soil Dynamics and Earthquake Engineering, 100: 518-528. https://doi.org/10.1016/j.soildyn.2017.07.003

ROLE OF AUTHORS: *AMAC – concept, overall method design, data gathering and analysis; writing, revising, and finalizing the manuscript JJCA – advising, method designs, data gathering and analysis, revising the manuscript; ACC – method designs (geotechnical), data gathering and analysis, revising the manuscript; CBB – method designs (seismic), data gathering and analysis, revising the manuscript.*

GUIDE FOR AUTHORS

The Palawan Scientist is an externally peer-reviewed multi-disciplinary and open-access journal that **does NOT charge any processing/publication fees**. It releases one volume with two issues per year (June and December).

Moreover, published articles in this journal are indexed in the master journal list of Clarivate Analytics, ASEAN Citation Index, Andrew Gonzalez Philippine Citation Index, Philippine E-Journals, and both Google and Google Scholar. Articles are also stored on AquaDocs, and The Internet Archive.

OBJECTIVE AND SCOPE

As a multi-disciplinary journal, The Palawan Scientist aims to publish high-quality and original researches in agriculture, fisheries and aquatic sciences, environment, education, engineering, mathematics, sociology, and related disciplines.

CALL FOR PAPERS

The Palawan Scientist is accepting original research articles, notes, and review papers for its coming issue. Please submit an e-copy of your manuscript through the "Submit Manuscript" panel of the website. For more information and regular updates, please refer to our Guide for Authors and visit or like our Facebook Page: The Palawan Scientist

FOR INQUIRIES OR FEEDBACK

For inquiries, suggestions or complaints authors may email the Editor-in-Chief at palawanscientist@gmail.com

TYPES OF PAPER

The Palawan Scientist categorizes manuscripts based on their contents and scientific contributions. The TPS classifies submitted manuscripts into 3 types:

1. **Research article:** Regular papers should report the results of original research which have not been previously published elsewhere, except in preliminary form. It should have a total of not more than 6,000 words and must be organized with the following main headings: **ABSTRACT, Keywords, INTRODUCTION, METHODS, RESULTS, DISCUSSION, ACKNOWLEDGMENTS, REFERENCES**.
2. **Notes** should be brief descriptions of experimental procedures, technical operations or applied activities within the laboratories or in the field. It should have a total of not more than 3,000 words and consist of **ABSTRACT**, **Keywords**, followed by the **NOTES**, **ACKNOWLEDGMENTS** and **REFERENCES**.
3. **Review Paper** should cover specific topics which are of active current interest. It may contain an **ABSTRACT**, **Keywords**, **INTRODUCTION**, the **different headings of the sub-topic**, **ACKNOWLEDGMENTS** and **REFERENCES** with a total of not more than 8,000 words.

MANUSCRIPT SUBMISSION PROCESS

1. Before submission, the authors are advised to carefully read and follow strictly the journal policies and the guide for authors to avoid delay in the publication process.
2. Authors must submit an e-copy of the manuscript through the "Submit Manuscript" panel of the website. The file name of the manuscript should be **Type of Paper_Family Name** of the Corresponding Author_Version 1 (e.g. **Research Article_Cruz_Version 1**).
3. The corresponding author must submit the following files:
   a. Full manuscript in **WORD FILE** using this TEMPLATE.
   b. Cover letter
   c. Copyright Transfer Agreement
   d. Open Access Agreement
   e. Checklist for Authors

MANUSCRIPT PREPARATION

1. General Guidelines

a. The manuscript should be typewritten using Times New Roman, font 10; double-spaced, single column, justified on A4 (8.3"x11.7") size paper, with 2.54 cm margins on all sides. All pages should be numbered consecutively at the bottom center of the page. Line numbers should be continuous (do not restart at each page).
b. The manuscript should be free from plagiarism; well written in American English; spelling and grammar are checked; and have been proofread by English Critic or a language editing software is used.
c. The author should refrain and/or are discouraged in citing publications from suspected predatory journals.

2. Title Page

a. The title page should contain the following: title of the article, running title, author(s), affiliation(s), name and complete contact details (mailing address and e-mail address) of the person to whom correspondence should be sent.
b. A superscript in Arabic numbers should be placed after the author's name as reference to their affiliations. The title of the paper should be above-centered, **bold** and written in a sentence form.
c. Capitalize only the first word of the title and proper nouns if there are. Scientific name(s) when included in the title should be accompanied by taxonomic authority.

3. Abstract

a. Abstract page should not be more than 250 words. The abstract should contain facts and conclusions, rather than citation of the areas and subjects that have been treated or discussed.
b. It may start with the hypothesis or a statement of the problem to be solved, followed by a description of the method or technique utilized to solve the problem.
c. It should end with a summary of the results and their implications.
d. **Keywords** – maximum of six alphabetically arranged words not mentioned in the title, lower-cased, except for proper nouns.

4. Introduction

a. Provide sufficient information of the introduction/background of the study and critique of pertinent literature or current level of knowledge without subheadings, figures, and tables to give the readers clear understanding of the purpose and significance of the study.

5. Methods

a. Provide all information of the population/samples of the study, study sites, research design, sampling procedure, data collection technique and data analysis which includes subheadings to distinguish the different methods (for each objective and other relevant subtopics).
b. Authors should clearly state all statistical tests, parameters and replications.
c. Equation should be inserted using the Equation Editor in the journal's suggested font type.
d. Authors should provide only the brand/model and country of all chemical/equipment used.

6. Results

a. Authors should present the result section by stating the findings of the research without bias and interpretation arranged in accordance with and to the order of objectives which are indicated by subheadings. Texts should not excessively repeat the contents of the tables and figures.

7. Discussion

a. Provide comprehensive interpretation and significance in accordance with the results in light of what is already known about the problem investigated, explained new knowledge or insights (conclusion and recommendation) that emerged in the results section.
b. Tables and figures may be used to compare the results of the study with those of authors/studies.

8. Acknowledgments

a. Indicate the source of financial support, individuals who assisted in the conduct of research and anonymous reviewers.

9. References

a. References to the literature citations in the text should be by author and year; if there are two authors, both should be mentioned; with three or more authors, only the first author's family name plus "et al." need to be given.
   References in the text should be cited as:
   - Single author: (Frietag 2005) or Frietag (2005)
   - Two authors: (De Guzman and Creencia 2014) or De Guzman and Creencia (2014)
   - More than two authors: (Sebido et al. 2004) or Sebido et al. (2004).
b. Use a semicolon followed by a single space when citing more than two authors. Arrange by date of publication with the latest being the last in the list (example: Sebido et al. 2004; Frietag 2005; De Guzman and Creencia 2014).
c. Use a comma followed by a single space to separate citations of different references authored by the same author (example: Jontila 2005, 2010). If the same author and year are cited, use a "letter" to distinguish one paper over the other (example: Creencia 2010a, b).
d. Alphabetize authors with the same year of publications. Use semicolons to separate each publication (example: Balisco and Babaran 2014; Gonzales 2014; Smith 2014).
e. Write journal's name in full (examples: The Palawan Scientist, not Palawan Sci; Reviews in Fisheries Science, not Rev. Fish. Sci.).
f. For articles with more than 10 authors, list only the first 10 authors followed by et. al.
g. The list of citations at the References section of the paper should include only the works mentioned in the text and should be arranged in alphabetical and chronological manner. If a referencing software was used, the following fields should be removed before submitting the manuscript.

h. Citing journal articles– name(s) and initial(s) of author(s), year, full title of research article (in sentence form), name of the journal (not abbreviated), volume number, issue number (if given), range of page numbers, DOI number (if available) and/or web link:

Dolorosa RG, Grant A and Gill JA. 2013. Translocation of wild *Trochus niloticus*: prospects for enhancing depleted Philippine reefs. Reviews in Fisheries Science, 21(3-4): 403-413. https://doi.org/10.1080/10641262.2013.800773

Ardines RB, Mecha NJMF and Dolorosa RG. 2020. Commonly gleaned macro-benthic invertebrates in a small offshore island of Cawili, Cagayancillo, Palawan, Philippines, The Palawan Scientist, 12: 102-125.

i. Citing of books – name(s) of author(s), year of publication, full title of the book (capitalize each main word), publisher, place of publication and total number of pages.

Gonzales BJ. 2013. Field Guide to Coastal Fishes of Palawan. Coral Triangle Initiative on Corals, Fisheries and Food Security, Quezon City, Philippines. 208pp.

j. Citing a chapter in a book – name(s) of author(s), year, full title of the chapter in a book (capitalize each main word), last name of editor and title of book, edition, publisher, place of publication and page range of that chapter:

Poutiers JM. 1998. Gastropods. In: Carpenter KE and Niem VH (eds). FAO Species Identification Guide for Fishery Purposes. The Living Marine Resources of the Western Central Pacific Seaweeds, Corals, Bivalves and Gastropods. Food and Agriculture Organization, Rome, Italy, pp. 364-686.

k. Citing a Webpage – names of the author (s), year, title of the article, webpage address and date accessed.

Froese R and Pauly D (eds). 2022. FishBase. www.fishbase.org. Accessed on 07 March 2022.

CITES (Convention on International Trade of Endangered Species). 2014. The CITES Appendices. Convention on International Trade in Endangered Species of Wild Flora and Fauna. www.cites.org. Accessed on 07 March 2022.

l. Citing a thesis or dissertation – author's family name, initial names of the author, year, title of the thesis, degree, name of institution, address of the institution, total number of pages (pp).

Guion SL. 2006. Captive breeding performance of *Crocodylus porosus* (Schneider 1901) breeders at the Palawan Wildlife Rescue and Conservation Center. BS in Fisheries. Western Philippines University-Puerto Princesa Campus, Palawan, Philippines. 28pp. (include weblink, if there's any, followed by accessed date).

Lerom RR. 2008. Biosystematics study of Palawan landraces of rice (*Oryza sativa* L.). Doctor of Philosophy, Institute of Biological Sciences, University of the Philippines-Los Baños College, Laguna, Philippines. 197pp. (include weblink, if there's any, followed by accessed date).

m. Citing a Report

Picardal RM and Dolorosa RG. 2014. Gastropods and bivalves of Tubbataha Reefs Natural Park, Cagayancillo, Palawan, Philippines. Tubbataha Management Office and Western Philippines University. 25pp. (include weblink, if there's any, followed by accessed date).

n. In Press articles when cited must include the name of the journal that has accepted the paper.

Alcantara LB and Noro T. In press. Growth of the abalone *Haliotis diversicolor* (Reeve) fed with macroalgae in floating net cage and plastic tank. Aquaculture Research.

o. Citing an article from an online newspaper.

Fabro KA. 2021. Surge in seizures of giant clam shells has Philippine conservationists wary. Mongabay. https://news.mongabay.com/2021/03/surge-in-seizures-of-giant-clam-shells-has-philippine-conservationists-wary/. Accessed on 07 March 2022.

10. Figures and Tables

a. Figures and tables should be numbered (Arabic numerals) chronologically. Stand-alone captions for figures and tables should be sentence-cased, double spaced, and have justified margins; the first line is not indented and placed immediately after the paragraph where it is first mentioned. The use of text boxes for figure and table captions are not allowed.

b. References to the tables and figures in the text should be cited as: Table 1; Figure 1; Tables 1 and 2; Figures 1 and 2; Table 1A; Figure 1B; (not Table 1a or Figure 1b) consistent to the label in the Tables and Figures.

c. Photos, maps, drawings, charts, and graphs should be treated as Figures and have at least 300 dpi, are included in the manuscript using the "Inset Pictures" tool of the MS Word. Note: A separate file of each photo should be available upon request.

d. Graphs must have white background free from major grid lines (of y-axis); the x and y axes are labeled and legend is provided.

e. Illustration should be original line drawings of good quality and should not exceed A4 size paper. Inscriptions should be readable even if the drawing is reduced by 75%. Drawings should be scanned and saved in TIF or PDF format before embedding on the manuscript. Separate files of the photos/illustrations may be requested upon the acceptance of the manuscript.

f. All photos used in the paper must have been taken by the author(s), if possible. Photos taken from other researchers/individuals/organizations must be duly acknowledged in the paper. The use of photos downloaded from the web/internet is strictly forbidden unless a written permission from the copyright holder (of that photo) is presented.

g. All rows, columns and edges of the table should be bordered by lines.

11. Scientific, English and Local Names

a. All organisms must be identified by their English, scientific names and local names if possible.

b. Scientific names and taxonomy authority must be cited for all organisms at first mention (e.g., *Stiphodon palawanensis* Maeda & Palla, 2015). Subsequently, only the initial of the genus should be written except when starting a sentence with a scientific name. All scientific names should be italicized. Example: *Epinephelus fuscoguttatus*; *Anadara* sp. *Musa* spp. Do not italicize the higher levels of taxonomic classification (example: family Echinometridae).
c. Local names should be in double quotes (example: locally called "saging" not 'saging'; "palay" not 'palay').
d. Research articles dealing on species list should provide the authorities for each species (example: *Conus magus* Linnaeus, 1758; *Enosteoides philippinensis* Dolorosa & Werding, 2014).

12. Punctuations, Equations, Symbols and Unit of measures

a. Unfamiliar terms, abbreviations, and symbols must be defined/spelled out at first mention even in the abstract. Acronym should only be spelled-out as it is introduced in the text, it should be written in acronym in succeeding parts of the paper.
b. Mathematical equations should be clearly presented so that they can be interpreted properly. Equations must be numbered sequentially in Arabic numerals in parentheses on the right-hand side of the equations.
c. In International System of Units of measurements must be used but separated from the value and the unit of measure (e.g. 5 mm, 25 g, 30 m^3, 100 μm, 9 ind ha^{-1}, 10 sacks ha^{-1}, 2 kg h^{-1}, 2 kg h^{-1} day^{-1}) and probability (*P*) is in upper cased and italicized (e.g. $P > 0.05$; $P < 0.05$; $P = 0.01$). To fix a single space between the value and its unit of measure, use the MS word command "CTR+SHIFT+SPACE BAR" to provide a space between the value and its unit of measure.
d. There is a single space between numbers and the following mathematical signs: ±, =, ×, -, +, ÷, (e.g. 92 ± 0.092; 5 × 6).
e. Numbers less than 10 should be spelled out (for example: eight trees, 10 fish) except when followed by a unit of measure (for example: 9 cm, not nine cm). Number mentioned at the start of the statement should be spelled-out (e.g. Nine fishermen not 9 fishermen or Six degrees Celsius not 6˚C).
f. The symbol for Degree (˚) should be inserted using the insert symbol option and not zero (0) or alphabet (o) superscript.
g. Do not separate a percent sign and degree of temperature with the number (example: 5% and 8˚C).
h. Write dates in this manner: day-month-year (example: 20 October 2012 or 20 Oct 2012).
i. Use a 24-h system for time (example: 1300 instead of 1:00 pm). To express a measured length of time, abbreviations for hour (h), minutes (min) and seconds (sec) should be used (example: 2 h and 30 min; or 2.5 h).
j. Include apostrophes in years (example: 2014's).
k. No periods in acronyms (example: UNESCO not U.N.E.S.C.O.; CITES not (C.I.T.E.S.)
l. Use a single capital letter when writing latitude and longitude (example: 9°44'27.80"N and 118°41'2.01"E). Compass points (north, south, east, west) and their derivations (northern, southern, eastern, western) are lowercase (example: north of Palawan) except when they form part of the place name (example: South Cotabato; Eastern Samar).

POLICIES

Plagiarism

Plagiarism is copying the author's (self-plagiarism) or someone else's ideas, works, and words without proper acknowledgement, credit or permission of the original author and source. The Palawan Scientist uses a plagiarism checker to identify the originality of the submitted manuscript. Authors should strictly refrain from plagiarism and follow the ethical standard of the research community.

All manuscripts submitted to The Palawan Scientist shall undergo plagiarism check, if plagiarism is detected, authors will be advised to rewrite/rephrase the plagiarized portion before the publication process begins.

Data fabrication and falsification

Fabrication concerns on making up research findings, while falsification is manipulating reports of scientific research results or data with an intention of giving false information about the status of submitted articles. Authors caught reporting any scientific research misconduct will no longer be allowed to submit their manuscript in the journal, and published articles which were later discovered to have such concern may be retracted upon the recommendation of the Technical Advisers.

Ethical consideration

Studies involving human subjects must have followed the institutional and national guidelines set by the ethics board. A consent statement form is secured for studies involving minors or children below 18 years old. Moreover, names and other information of the subjects must be kept confidential and will be excluded from the manuscript. Other relevant documents should be ready upon the request of The Palawan Scientist. Additionally, research studies involving the use of animals must have also followed all institutional and national ethical guidelines for the care and use of test/experimental animals.

Disclaimer

The Editorial Board of The Palawan Scientist does not provide warranties as to the completeness and veracity of the content. Moreover, the opinion and ideas expressed in this publication are by the authors and not necessarily of the publisher. The Western Philippines University cannot accept any legal responsibility or liability arising from plagiarism and other errors.

Retractions

In some cases, the paper published in The Palawan Scientist may be retracted due to scientific fraud, such as unethical authorship, repeated submissions, false claims of authorship, unethical use of data, or plagiarism. Before a paper may be

retracted, the complainant or the author must send a signed communication to the Editor-In-Chief (EIC). The editor reserves the right to retract the article as maybe suggested by the Technical Advisers.

Corrections/Errata
Authors are obliged to report errors in their articles that are relevant to the accuracy of published data. The journal shall carry out an investigation, and if, after the investigation, the concern is valid, the author shall be contacted through their email and given the opportunity to address the issue. Corrections and addendum will be included in the "Errata" section of the journal's succeeding issue.

Removal
The manuscript may remove from the journal's website when The Palawan Scientist has been informed that the content brings defamatory or infringes other's legal rights or is otherwise unlawful, if acted upon, the content would pose immediate and serious health risk. In this case, the whole text will be placed with a statement explaining that it's been removed due to legal reasons.

Withdrawal
It is strongly discouraged to withdraw a manuscript after submission to The Palawan Scientist especially when it has undergone peer-review process. However, a valid reason for withdrawal may be acknowledged by the EIC if all authors signed a letter request clearly stating the purpose of manuscript withdrawal.

Data and Reproducibility
To fully assess the process of a research article, all data related to the submitted articles in The Palawan Scientist should be available for future use. Authors are encouraged to deposit detailed descriptions of their method used in the study to any repositories. However, the authors may provide supporting information to display all necessary data when uploading data to repositories is not possible.

Complaints, Appeals, and Allegations
Any complaints, appeals, and allegations of scientific research misconduct shall be sent to the EIC to explain their concern. The identity of the complainants shall not be disclosed. Parties involved shall be contacted for further inquisition.

Authorship and Contributorship
For articles with two or more authors, it is required to indicate the contributions of each author which may include but not limited to the following: conceptualization, fund sourcing, conduct of experiment, data collection, data analysis, manuscript writing. Any change (deletion or addition) to authorship should be made before the publication of the article. To request such change, the corresponding author must have received permission from all co-authors before emailing the editor citing the reasons for changes. A confirmation from the added or deleted authors must be also received by the editor.

Conflicting Interest
Authors must declare any conflicting interest. If any conflicting interest is present, it must be briefly stated. If there's none, the statement "The authors declare that there is no conflicts of interests to any authors".

Copyright Transfer Agreement
All authors are required to provide consent to the terms mentioned in The Palawan Scientist Copyright Transfer Agreement. The agreement shall be accomplished electronically and must be submitted together with the manuscript. The Copyright Transfer Agreement can be downloaded here.

Open Access Agreement
All authors are required to provide consent to the terms mentioned in The Palawan Scientist Open Access Agreement. The agreement shall be accomplished electronically and must be submitted together with the manuscript. The Copyright Transfer Agreement can be downloaded here.

Repository Policy
The Palawan Scientist allows authors to deposit different versions of their articles in an institutional or other repository of their choice, including submitted, accepted, and published versions without any embargo.

CODE OF ETHICS

The Palawan Scientist Journal adheres to the highest ethical standard of publication.

Code of Ethics for Authors
1. The manuscript shall contain the author's original and unpublished work, and which is explicitly not simultaneously considered for publication in other journals.
2. The Guide for Authors should be strictly followed and complied with.

3. The manuscript shall be free from plagiarism and falsification, well-written in American English, spelled and grammar checked using language editing software and/or underwent proofreading by an English critic. The works of other authors have been properly and fully cited.
4. The author shall nominate or suggest at least three competent reviewers who are experts in the field and who have not actually participated in the research work submitted for consideration. However, the editor reserves the right to invite reviewers not among those suggested in the interest of the most critical and fair assessment of the submitted manuscript.
5. Each author must have a substantial contribution in the conduct of the study and/or writing of the manuscript and such contributions must be stated and enumerated unequivocally. All others may be listed in the Acknowledgment section of the manuscript.
6. The journal editors shall establish communications only with the corresponding author in the case of multiple-authored submissions, who shall keep all co-authors updated about the progress of the review process and its outcome.
7. The corresponding author shall comply with deadlines set for revising their manuscripts and other tasks.
8. It is the responsibility of the authors to comply with all applicable ethical standards in the conduct of the study and to reflect such compliance in the submitted work.
9. The corresponding author should contact the editor promptly to retract/correct the published paper when serious errors and/or grave ethical violations are detected by a third party.

Code of Ethics for Reviewers

1. Reviewers should agree to review manuscripts only for those they have the subject expertise.
2. Reviewers immediately identify any conflicts of interest (resulting in financial, personal, intellectual, professional, political, or religious), if any, and subsequently decline the review request.
3. Reviewers should ensure performing a requested review within the time-frame set by the editors and decline the invitation if such time-frame cannot be complied with.
4. The journal employs a double-blind review system so that any untoward biases may be avoided.
5. Reviewers are expected to be totally objective, impartial and constructive with their review to ensure the best possible outcome in showcasing the research as a worthy contribution to the scientific literature.
6. All information should be treated by reviewers with utmost respect and strictest confidentiality and should never be used for purposes other than for critical evaluation for scientific merit and technical impact.
7. Reviewers should follow the TPS guidelines on peer review and other established ethical and reviewing protocols.

Code of Ethics for Editors

1. Editors should be responsible for anything distributed in their journals.
2. Editors should make choices to acknowledge or dismiss articles based on their academic or journalistic merit, counting their significance, creativity, clarity, and pertinence to the journal's mission and area.
3. Editors should accept original articles from all authors and should at all times keep up objectivity and maintain balance in reviewing all articles, acting without predisposition of bias or favoritism based on the origin of a paper; an author's sexuality, race, nationality, ethnicity, affiliation or political convictions, age; or commercial rumination.
4. Editors should give direction to reviewers on everything expected of them, including the confidentiality in handling submitted material, disclosing conflict of interest before the review, and ensuring that the reviewers' identities are protected.
5. Editors should take steps to guarantee the timely evaluation of all articles and answer promptly the author's queries regarding the status of their papers.
6. Editors should explain to authors the decision made on their articles through a letter with the reviewer's comments and suggestions.
7. Editors should adhere and conform to the editorial policies, regulatory guidelines, and higher ethical standards of publication.
8. Editors should not expose the identity of authors, reviewers and keep the privacy of unpublished articles.
9. Editors should protect the decency of the journal from suspected and alleged misconduct in the research and publication process. They should instigate proper and reasonable investigation to fairly resolve any issues.

PUBLICATION PROCESS

Received papers will be properly acknowledged and will undergo screening process using the Guide for Author's Checklist and anti-plagiarism tool. It will be immediately sent off for review if it satisfies the preliminary evaluation. If it does not, it will be sent back to the corresponding author for revision.

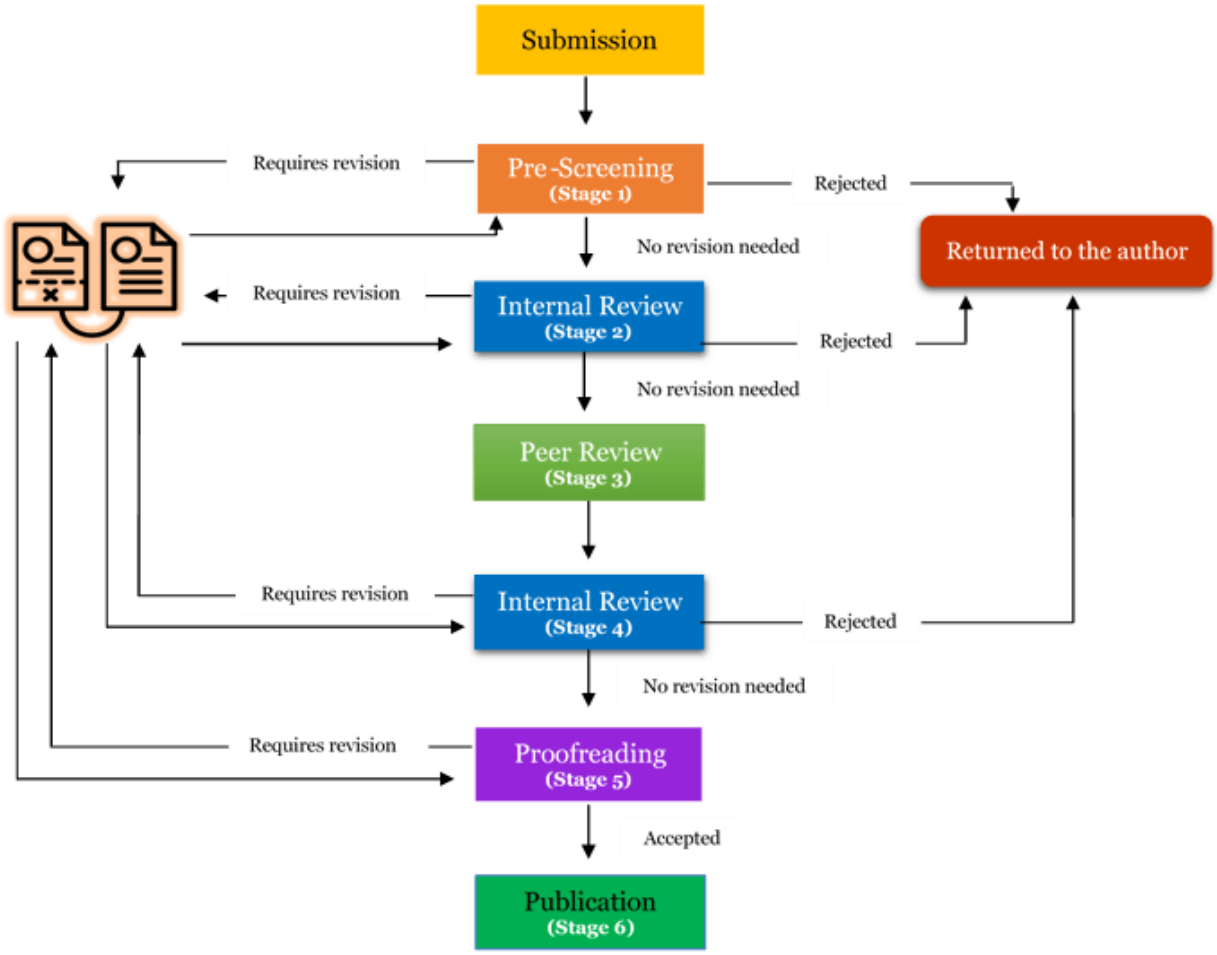

Peer-review Process

All submitted manuscripts shall undergo a double-blind review process before publication. The double-blind review process ensures that information about the authors and reviewers shall remain anonymous to provide objective judgment of the paper. The manuscript sent for external review should not contain the authors' name, affiliation, and acknowledgment section. At least two reviewers shall evaluate the manuscript and suggest whether it shall be accepted, revised, or rejected. Manuscripts returned to authors for revision or correction must be resubmitted within the given deadline. The resubmission could be extended upon request to the editor.

WPU MISSION

WPU commits to undertake quality instruction, research and extension programs towards a progressive Western Philippines

VISION

The leading university for holistic human development in Western Philippines and beyond

CORE VALUES (3CT)

Culture of Excellence

We encourage every Personnel to excel in every performance of their duties leading to quality results

Commitment

We commit our talents and abilities and will work for the general welfare of the University

Creativity

We continue to quest for new ideas for the development of the University and its stakeholders

Teamwork

We promote at all times team approach to achieve common goals

The Palawan Scientist

www.palawanscientist.org

Volume 15(2), December 2023

Western Philippines University
San Juan, 5302 Aborlan, Palawan, Philippines
www.wpu.edu.ph